4. Results and discussion

The work carried out towards achieving the proposed plan of work has been discussed under the following heads.

4.1 Determining structural requirements for the peripherally acting 1,5-diaryl pyrazole containing CB1 receptor antagonists as anti-obesity agents by 3D-QSAR (CoMFA/CoMSIA) studies. Designing of some newer compounds having better activity and properties.

4.2 Development of pharmacophore and 3D-QSAR (atom-based) models using different scaffolds for the identification of essential features responsible for CB1 receptor antagonistic activity.

4.3 Performing of virtual screening for the identification of novel scaffolds by using different filters like pharmacophore model, 3D-QSAR (atom-based), molecular docking, Lipinski's rule of five, CNS score and receptor-ligand interactions.

4.4 Hit optimization through molecular modeling techniques and synthesis of the designed compounds.

4.5 Pharmacological evaluation/screening of the synthesized compounds as peripherally acting CB1 receptor antagonists as potential anti-obesity agents.

4.6 Molecular modeling and SAR studies of the synthesized compounds.

4.1 Determining structural requirements for the peripherally acting 1,5-diaryl pyrazole containing CB1 receptor antagonists as anti-obesity agents by 3D-QSAR (CoMFA/CoMSIA) studies. Designing of some newer compounds having better activity and properties

To design peripherally acting CB1 receptor antagonists, one needs to know the structural requirements responsible for such an activity. In the present study, it was planned to explore the structural requirements in peripherally acting 1,5-diaryl pyrazole containing CB1 receptor antagonists using 3D-QSAR studies. CoMFA/CoMSIA are the most widely used techniques in molecular modeling. The 1,5-dirayl pyrazole series was selected because rimonabant contained the same scaffold. 1,5-Diaryl pyrazole containing compounds having peripheral activity only were selected so that the

essential structural requirements for the peripherally acting CB1 receptor antagonists could be explored.

The best developed model was used for the designing of newer peripherally acting CB1 receptor antagonists having increased PSA, lowered lipophilicity and enhanced potency.

4.1.1 Dataset

A dataset of peripherally acting selective CB1 receptor antagonists were chosen for the present 3D-QSAR (CoMFA/CoMSIA) studies. A total of 72 compounds containing the 1,5-diaryl pyrazole scaffold were chosen having CB1 receptor antagonistic activity.[145,146] Compounds with the same range of biological activity and those having structural similarity were omitted from the dataset. The compounds which did not have biological activity in the exact quantitative terms were also removed from the dataset. CB1 receptor antagonistic activity was available in terms of IC_{50} values in the nanomolar (nM) range in the literature. These IC_{50} values (in molar concentration) were converted into their corresponding pIC_{50} ($-\log IC_{50}$) which were utilized as dependent variables for the development of both CoMFA and CoMSIA models. The structures and biological activity of the compounds used are shown in Table 4.1.1.

4.1.2 Distribution of training and test set

The compounds of the dataset were distributed into the training set (54 compounds) and test set (18 compounds) in 3:1 ratio as shown in Table 4.1.1. The compounds in the training and test sets were divided randomly by applying the following logic: i) Biological activity and structural variations present in a wide range in the training set were also maintained in the test set. ii) The template molecule (the most potent compound among the dataset) was made a part of training set. The activities of the training set and test set ranged from 0.1 nM (pIC_{50} = 10.000) to 980 nM (pIC_{50} = 6.009) and 0.8 nM (pIC_{50} = 9.097) to 455 nM (pIC_{50} = 6.342), respectively. The test set was used for the purpose of evaluating the predictive power of the developed models.

4.1.3 Alignment rules

The derivation of active conformation of the most active compound and alignment of all the compounds on the active conformation is one of the essential steps in CoMFA. Development of a good CoMFA model depends on the relative positioning

of the ligands in the fixed lattice.[248] In the present study, the most potent compound (**20**) in the series was used as the template molecule for alignment purposes. 3D-QSAR models were also obtained using two equipotent compounds (**3** and **24**) as templates by using different types of alignments. Unfortunately, poorer statistical results were obtained for these models when compared to the model developed using compound (**20**) as the template. The range of r^2_{cv} values was 0.294 – 0.412 having an optimum number of component (ONC) value of 2, which were not in the acceptable range for the models developed using compounds (**3** and **24**) as the templates. The results obtained for the model developed using compound (**20**) as template were encouraging, i.e. (r^2_{cv} = 0.552 with ONC = 6). Thus, compound (**20**) was selected as the template molecule for further studies. The molecular alignments of the compounds were carried out using different methods, such as atom-based, data-based, centroid-based and centroid/atom-based as shown in the Fig. 4.1.1.

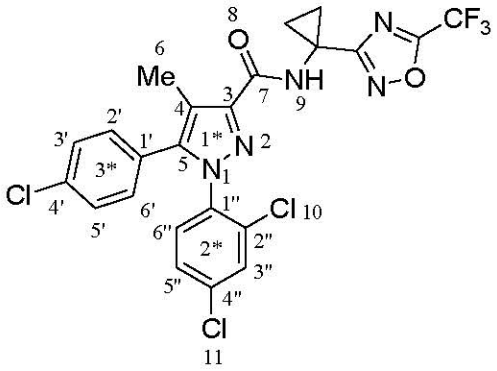

Alignments	Atom/Centroid
I	1, 3-5
II	1-5
III	1*-3*
IV	1*,6,7
V	1*, 3*, 7
VI	1-5
VII	1-5, 1'-6'
VIII	1-5, 1"-6"
IX	1-5, 1'-6', 1"-6"
X	1-5, 1'-6', 1"-6", 6-11

Fig. 4.1.1 Template molecule (**20**) and the alignment rules.

4.1.3.1 Atom-based alignment

In this alignment, selected atoms of the template molecule (**20**) were used for RMS fitting over the corresponding atoms of all the compounds in the dataset. Two types of alignments (I & II) were performed using different atoms as shown in Fig. 4.1.1.

4.1.3.2 Centroid-based alignment

In this alignment, the pyrazole ring and the two phenyl rings were defined as centroids (Fig. 4.1.1). Pairwise superimposition of centroids of the template molecule

(**20**) was carried out with the corresponding centroids of all the compounds (alignment III).

4.1.3.3 Centroid and atom-based alignment

In this alignment, both centroids and atoms were considered for the purpose of alignment. Two types of alignments (IV & V) were defined (Fig. 4.1.1). Pairwise superimposition of centroids and atoms was done in this alignment.

4.1.3.4 Data-based alignment

Data-based alignment was carried out by using the 'Align Database' function in SYBYL. Different types of combinations used for data-based alignments (VI-X) are shown in Fig. 4.1.1. All the compounds were aligned using these common fragments. The aligned compounds using data-based alignment (VI) are shown in Fig. 4.1.2.

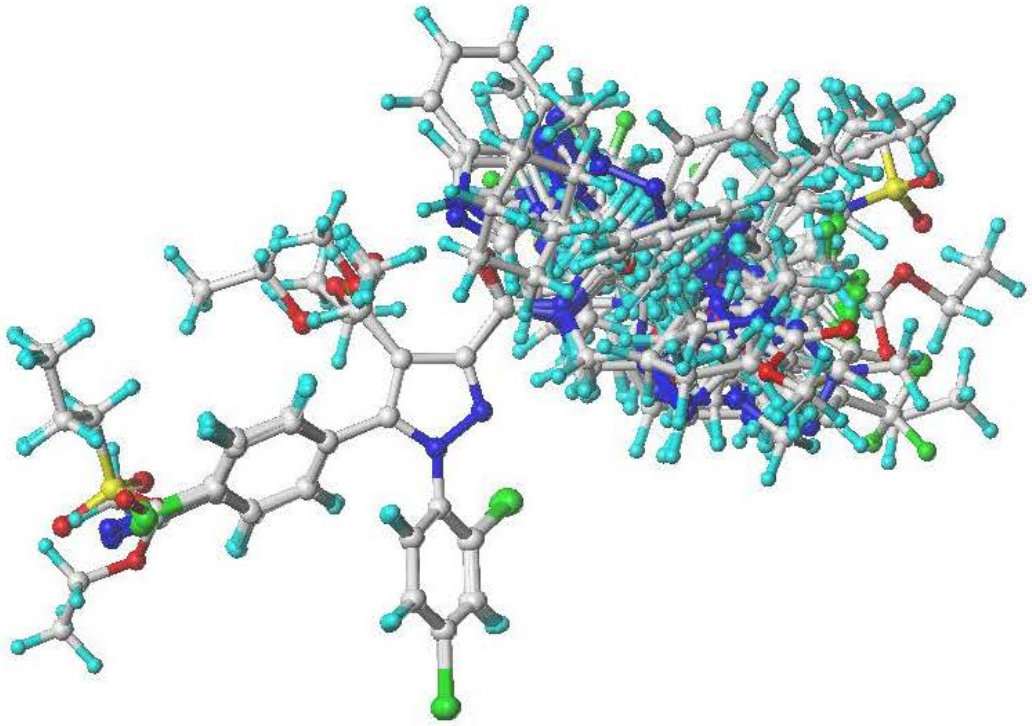

Fig. 4.1.2 Alignment of the compounds using data-based alignment (VI).

Table 4.1.1 Chemical structures of compounds (**1-72**) and their biological activities.

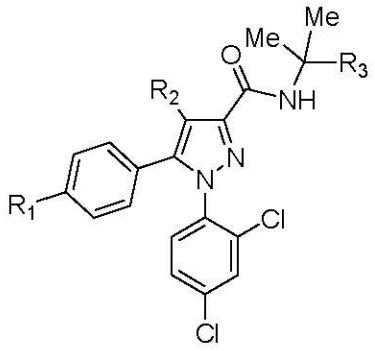

(1-18)

Compd	R_1	R_2	R_3	Experimental		Predicted pIC_{50}	
				IC_{50} (nM)	pIC_{50}	CoMFA	CoMSIA
1*	Cl	Me	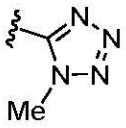	145	6.839	7.826	7.729
2	Cl	Et	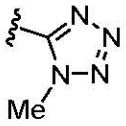	0.5	9.301	9.788	9.724
3	Br	Et	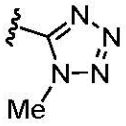	0.1	10.000	9.777	9.828
4	$OSO_2{}^nPr$	Me	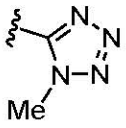	1.1	8.959	8.850	9.021
5*	CN	Et	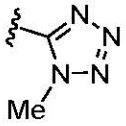	22	7.658	7.556	8.016
6	OMe	Et	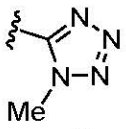	5	8.301	8.325	8.460
7	CO_2Et	Et	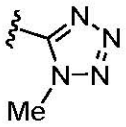	17	7.770	7.634	7.797
8	Cl	Me	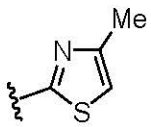	15	7.824	7.764	7.763
9*	Cl	Me	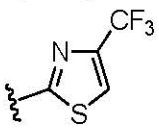	2	8.699	7.925	8.361

10	Cl	Me	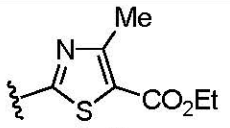	22	7.658	7.717	7.383
11	Cl	Me	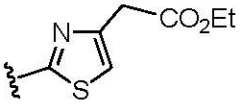	10	8.000	8.046	7.833
12*	Cl	Me	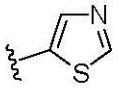	12	7.921	7.891	8.021
13	Cl	Me	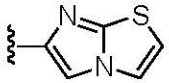	11	7.959	7.896	7.698
14	Cl	Me	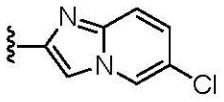	88	7.056	7.131	6.988
15	Cl	Me	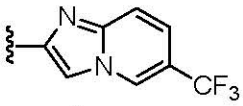	63	7.201	7.280	7.359
16	Cl	Me	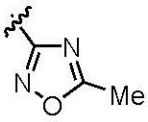	33	7.481	7.415	7.480
17	Cl	Me	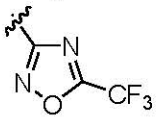	3	8.523	8.803	8.316
18	Cl	Me	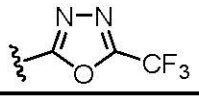	6	8.222	8.317	8.324

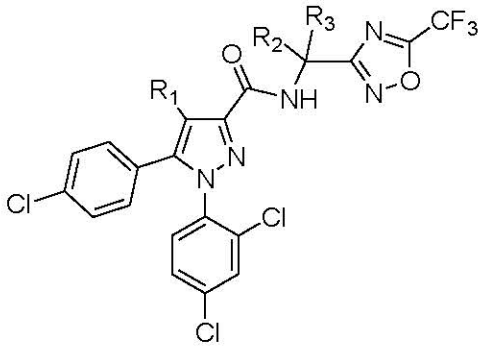

(19-25)

Compd	R_1	R_2	R_3	Experimental		Predicted	pIC_{50}
				IC_{50}(nM)	pIC_{50}	CoMFA	CoMSIA
19*	Me	Et	Me	6	8.222	8.304	8.118
20	Me	-CH_2CH_2-		0.1	10.000	9.774	9.751
21*	Me	-$CH_2CH_2CH_2$-		0.8	9.097	9.229	9.516
22	CH_2OH	Me	Me	0.4	9.398	9.097	9.336
23*	CH_2OMe	Me	Me	4	8.398	8.750	8.895
24	CH_2OH	-CH_2CH_2-		0.1	10.000	10.246	10.157
25	CO_2Et	-CH_2CH_2-		1	9.000	9.002	8.809

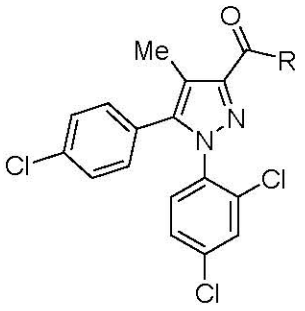

(26-31)

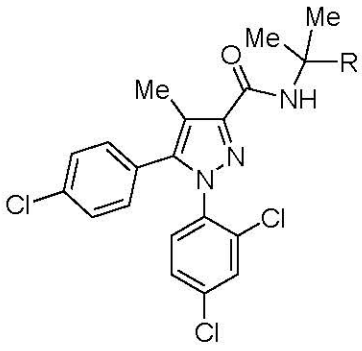

(32-56)

Compd	R	Experimental		Predicted	pIC_{50}
		IC_{50} (nM)	pIC_{50}	CoMFA	CoMSIA
26	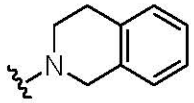	18	7.745	7.722	7.828
27	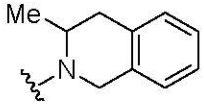	20	7.699	7.743	7.636
28	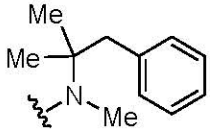	96	7.018	7.159	7.077
29	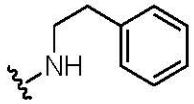	10	8.000	8.167	7.696
30	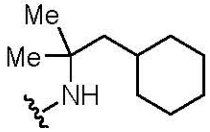	26	7.585	7.611	7.529
31	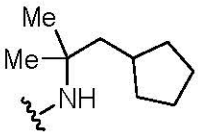	21	7.678	7.714	7.556
32	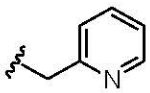	2	8.699	8.671	8.799
33	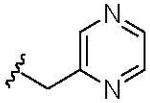	57	7.244	7.330	7.454
34	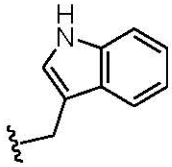	20	7.699	7.570	7.748
35	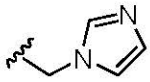	71	7.149	7.178	7.247
36	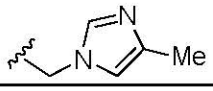	20	7.699	7.526	7.587

37*	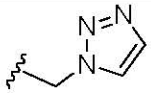	15	7.822	7.608	7.788
38*	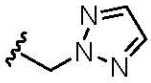	16	7.796	7.434	7.685
39*	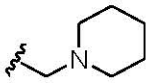	455	6.342	6.714	6.635
40	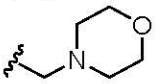	47	7.328	7.129	7.385
41	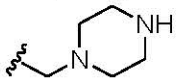	900	6.046	6.212	6.019
42*	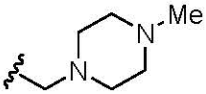	310	6.509	6.554	6.328
43	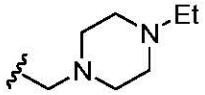	855	6.068	6.222	6.176
44	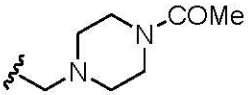	633	6.199	6.253	6.205
45	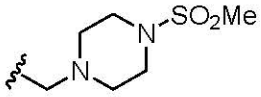	980	6.009	5.829	5.892
46	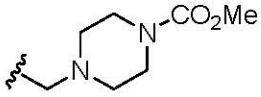	29	7.538	7.416	7.463
47	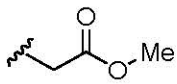	17	7.770	7.705	7.647
48	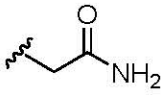	25	7.602	7.612	7.721
49*	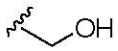	60	7.222	7.825	7.831
50*	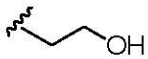	33	7.481	8.014	7.684
51	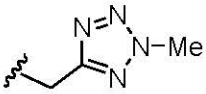	71	7.149	7.237	7.416
52	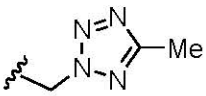	18	7.745	7.874	7.805
53	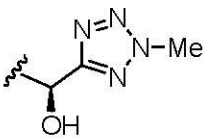	74	7.131	7.044	7.168
54*	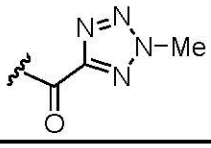	6	8.222	8.303	7.520

55	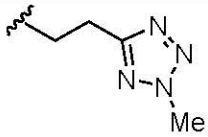	11	7.959	7.901	8.094
56	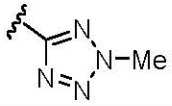	88	7.056	7.276	7.299

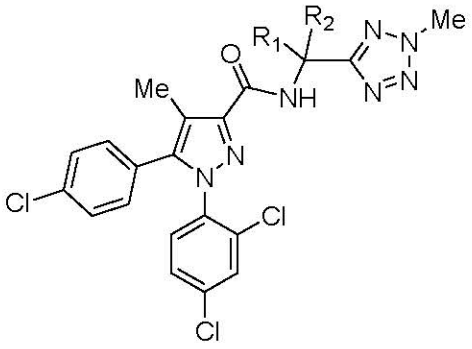

(57-64)

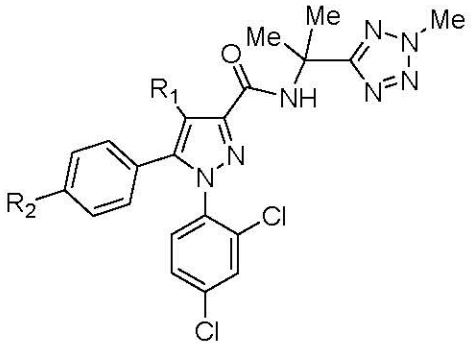

(65-72)

Compd	R_1	R_2	Experimental		Predicted	pIC_{50}
			IC_{50} (nM)	pIC_{50}	CoMFA	CoMSIA
57	H	H	100	7.000	7.104	7.286
58*	-CH_2CH_2-		61	7.215	8.517	7.846
59	Et	Et	35	7.456	7.250	7.569
60	-$CH_2CH_2CH_2$-		10	8.000	7.944	7.966
61*	Me	Et	18	7.745	7.900	7.303
62*	Me	-CH_2OH	77	7.114	7.177	7.288
63	-$(CH_2CH_2)_2$-		16	7.799	7.796	7.896
64	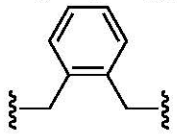		14	7.854	7.758	7.960
65*	Et	Br	4	8.398	8.871	8.255
66	Me	$OSO_2{}^nPr$	7	8.155	8.239	8.415
67	Me	CN	31	7.509	7.494	7.382
68	Et	CN	34	7.469	7.627	7.463
69	CH_2OH	Cl	8	8.097	8.104	8.343
70	CH_2F	Cl	3	8.523	8.164	7.850
71	CO_2Et	Cl	1	9.000	8.937	8.879
72	CH_2OH	$OSO_2{}^nPr$	0.5	9.301	9.245	9.118

* Test set compounds

4.1.4 CoMFA analysis

Peripherally acting 1,5-diaryl pyrazole containing CB1 receptor antagonists were utilized for the development of 3D-QSAR models using different fields in CoMFA and CoMSIA methods. A number of models were developed by applying

various alignments rules (Fig. 4.1.1 and 4.1.2). The importance of each field was studied individually and after that the analysis was carried out using steric and electrostatic fields calculated at each grid point simultaneously. This method was based on partial least square analysis using varying column filtering values. The column filtering value was set to 2.0 kcal/mol in the present study. CoMFA analysis used Coulombic and Lennard-Jones potentials to assess the contribution from different fields. The CoMFA results of these alignments (I-X) are summarized in Table 4.1.2. A QSAR model can be judged for its creditable prediction of biopotency of the unknown molecules on the basis of statistical parameters. All the necessary statistical parameters, such as r^2_{ncv}, r^2_{cv}, standard error of estimation (SEE), standard error of prediction (SEP), Fischer statistics (*F*-test), ONC and predictive correlation coefficient were analyzed for the evaluation of the predictive accuracy of the developed 3D-QSAR models.

To obtain the best model, various alignments, such as two types of atom-based (I and II), one type of centroid-based (III), two types of centroid and atom-based (IV and V) and five types of data-based alignments (VI-X) were tried. Out of these alignments, the data-based (VI) alignment offered the best model. Alignment (VI) afforded r^2_{cv} = 0.552 with six components, r^2_{ncv} = 0.973, *F*-value = 281.239 and r^2_{pred} = 0.528. The remaining CoMFA results of different alignments are shown in Table 4.1.2. It was observed that data-based alignment (VI) offered the best statistical parameters showing high r^2_{cv}, r^2_{ncv}, *F*-value, low SEE value and good r^2_{pred}. Thus, data-based alignment (VI) was considered to be the best model on the basis of its predictive accuracy. Contributions of steric and electrostatic fields for the best developed model were 43.4 and 56.6 %, respectively.

Table 4.1.2 Summary of CoMFA results

Statistical Parameters	**Type of Alignment**									
	I	II	III	IV	V	**VI**	VII	VIII	IX	X
r^2_{cv}	0.381	0.421	0.424	0.423	0.461	**0.552**	0.542	0.546	0.522	0.561
ONC	3	2	5	6	6	**6**	5	6	5	6
SEP	0.757	0.744	0.738	0.747	0.722	**0.658**	0.658	0.662	0.672	0.651
r^2_{ncv}	0.848	0.743	0.940	0.972	0.955	**0.973**	0.945	0.964	0.943	0.974
SEE	0.376	0.486	0.238	0.164	0.209	**0.162**	0.228	0.187	0.233	0.158
F-value	92.792	73.842	150.156	271.783	164.924	**281.239**	164.613	207.441	157.391	296.518
$P\ r^2 = 0$	0	0	0	0	0	**0**	0	0	0	0
r^2_{pred}	0.492	0.467	0.330	0.438	0.402	**0.528**	0.501	0.464	0.454	0.416

4.1.5 CoMSIA analysis

The CoMSIA method is used for overcoming the limitations of steric and electrostatic fields of the CoMFA method. CoMSIA analysis used a Gaussian function to assess the contributions from different fields. The CoMSIA method is a combination of five different fields, including steric (S), electrostatic (E), hydrophobic (H), hydrogen bond donor (D) and hydrogen bond acceptor (A). By using different combinations of fields, various CoMSIA models were developed that showed moderate to high internal and external predictivity as shown in Table 4.1.3. The CoMSIA model obtained with a combination of all the five fields yielded r^2_{cv} = 0.529 with six components, r^2_{ncv} = 0.966, *F*-value = 223.662 and r^2_{pred} = 0.367. The contributions of SEHDA fields for this model were 11.2, 37.1, 20.9, 8.9 and 21.9 %, respectively. The best CoMSIA model developed using a combination of SHA fields yielded the r^2_{cv} = 0.571 with six components, r^2_{ncv} = 0.960, *F*-value = 188.701 and r^2_{pred} = 0.679. The contributions of SHA fields were 19.9, 39.9 and 40.3 %, respectively. Figures 4.1.3 and 4.1.4 represent graphs plotted between the experimental and predicted activities for the respective training set and test set compounds for the best developed CoMSIA model (SHA). The best developed CoMFA model considered only the steric and electrostatic interactions showing an acceptable r^2_{cv} value of 0.552 and r^2_{pred} = 0.528. Whereas the best developed CoMSIA (SHA) model yielded higher r^2_{cv} value of 0.571 and r^2_{pred} = 0.679, indicating that CoMSIA (SHA) model is a better predictive model.

Table 4.1.3 Summary of CoMSIA results

Statistical Parameters	Combination of fields used							
	SHE	SED	SEA	SHA	HAD	SEHA	SEHD	SEHDA
r^2_{cv}	0.683	0.518	0.467	**0.571**	0.476	0.537	0.645	0.529
ONC	6	6	5	**6**	6	6	6	6
SEP	0.553	0.518	0.695	**0.644**	0.712	0.669	0.586	0.674
r^2_{ncv}	0.954	0.952	0.919	**0.960**	0.945	0.963	0.956	0.966
SEE	0.210	0.215	0.277	**0.196**	0.231	0.189	0.206	0.181
F-value	163.620	156.235	108.747	**188.701**	134.174	203.463	173.098	223.662
P $r^2 = 0$	0	0	0	**0**	0	0	0	0
$r^2_{predictive}$	0.437	0.354	0.470	**0.679**	0.510	0.429	0.386	0.367

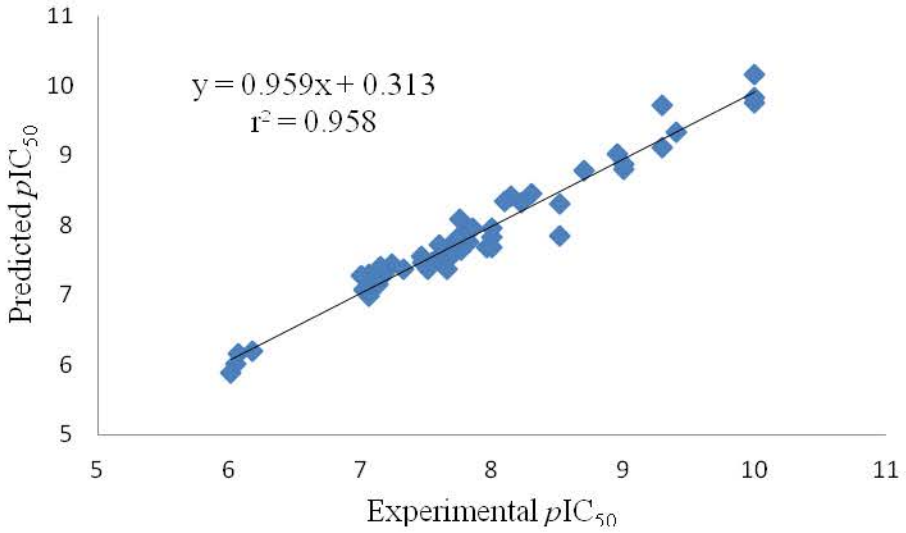

Fig. 4.1.3 Graph of experimental versus predicted activities of training set compounds for the best CoMSIA model (SHA).

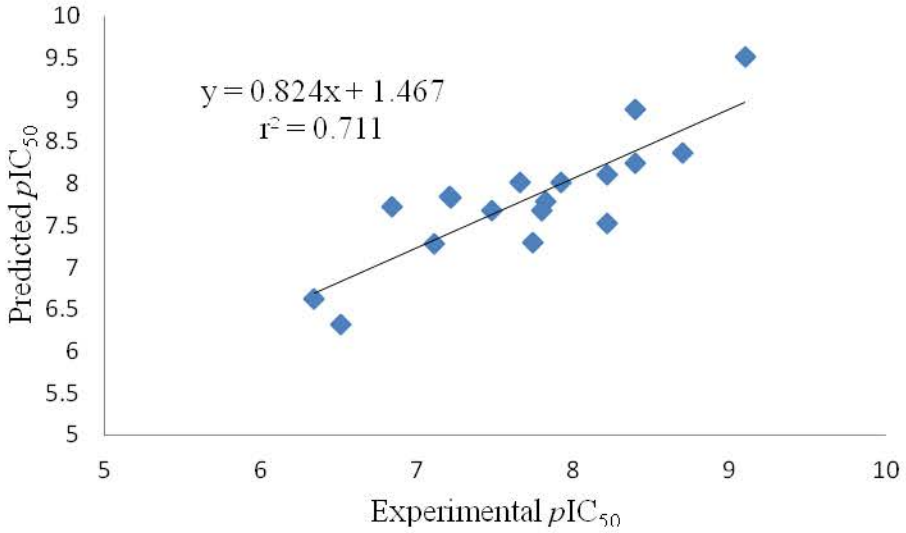

Fig. 4.1.4 Graph of experimental versus predicted activities of the test set compounds for the best CoMSIA model (SHA).

4.1.6 Validation of the best CoMSIA model

Validation of a developed model is an important criterion if the developed model is to be used for prediction purposes. Different validation parameters, such as internal validation, *F*-test, *Y*-randomization test, bootstrapping, external validation and modified r^2 (r^2_m) were utilized to validate the best developed CoMSIA model.

4.1.6.1 Internal validation

To ascertain the predictive accuracy of the model i.e. its ability to compute correctly the biological activity of the compounds for the training set, an internal validation test was performed.[249] The best CoMSIA model (SHA) showed a good cross-validated correlation (r^2_{cv} = 0.571, r^2_{ncv} = 0.960) which indicated that the developed model had a high internal predictive accuracy.

4.1.6.2 Fischer statistics (F-test)

Fischer value (*F*) is defined as the ratio between the explained and unexplained variance for a given number of degree of freedom. A higher *F*-value for the developed model than the threshold tabulated value indicates that there is a high probability of the developed model to be statistically significant.[250] The *F*-value for the best CoMSIA model (SHA) was 188.701 [F_{05} (6,71) = 3.06 (Tab)] at 99 % confidence level, indicating that the model is statistically significant.

4.1.6.3 *Y*-Randomization test

The *Y*-randomization test is the most commonly used test to eliminate the possibility of chance correlation and ensure the robustness of the developed model.[251,252] This test is performed by randomly shuffling the dependent variable vector (pIC_{50}) and using the previously selected matrix of independent variables (descriptors) of the training set compounds followed by rebuilding the models using the original alignment rule and evaluating the models by predicting the biological activity of the training and test set compounds. It is expected that the derived models would show significantly lowered r^2_{cv} and r^2_{ncv} values than the original one after several repetitive trials.[251] Ten random trials were performed for the best developed CoMSIA (SHA) model and the obtained poor r^2_{cv} and r^2_{ncv} values ensured the robustness of the original model. The non-cross-validated and cross-validated r^2 for the CoMSIA (SHA) models were obtained in the range of 0.301 to 0.580 and -0.693 to 0.021, respectively, as shown in Table 4.1.4. Thus, the random trials were not matching with the original model. Hence, the *Y*-randomization test validates that the original model is not a case of chance correlation.

Table 4.1.4 Summary of *Y*-randomization test for the best CoMSIA (SHA) model

Parameters	Value
No. of random trials	10
No. of trials with r^2_{cv} and r^2_{ncv} greater than non-random trials	0
No. of trials with r^2_{cv} and r^2_{ncv} lesser than non-random trials	10
Range of r^2_{ncv} from randomized data	0.301 to 0.580
Range of r^2_{cv} from randomized data	-0.693 to 0.021

4.1.6.4 Bootstrapping

Validation with bootstrapping was carried out for 100 runs to further assess the robustness and statistical confidence of the developed model. In the bootstrapping method, many new datasets were generated from the original dataset by randomly selecting samples from the original dataset and the model is generated by using the same (i.e. 6) optimal number of components. Each of these bootstrapping samples is used for performing statistical calculations. The measurement of bias of the original calculations is based on the difference between the calculated parameters from the original dataset and the average of the parameters calculated from the many bootstrapping samplings.[253] For the best CoMSIA model (SHA), the bootstrapped variance value (r^2_{bs} = 0.977) and bootstrapped standard deviation (SD_{bs} = 0.008) suggest a good internal consistency within the dataset. This confirms that a reliable and stable 3D-QSAR model has been successfully developed.

4.1.6.5 External validation

The predictive performance of a model is evaluated via validation of test set compounds. A set of 18 compounds were used for the external validation of the developed CoMFA/CoMSIA models to verify the stability and prediction accuracy of the developed models. The predictive correlation coefficient, r^2_{pred} values were 0.528 and 0.679 for CoMFA and CoMSIA (SHA) models, respectively.

4.1.6.6 Modified r^2 (r^2_m)

Modified r^2_m is another validation criterion to validate the external predictability of the developed QSAR models. The r^2_m value is used to penalize a model exhibiting a large difference between the actual and the predicted activities of the test set. The predicted activity of the test set compounds should be near to the corresponding actual activity of the compounds; hence, the r^2_0 value will be close to the r^2 value in the case of a good prediction. Here, r^2 is the squared correlation coefficient between the

observed and predicted values of the test set compounds and r^2_0 is squared correlation coefficient between the observed and predicted values of the test set compounds with intercept set to zero value. For the best external prediction, the r^2_m value will be similar to the r^2 value ($r^2_m = r^2$) while in the worst condition the value of r^2_m will be zero ($r^2_m = 0$). The external prediction accuracy of a model is considered to be good when the r^2_m value is greater than 0.5. The best developed CoMSIA (SHA) model exhibited r^2_m values of 0.575 for test set (Fig. 4.1.5), indicating that the developed model was highly predictive and reliable.

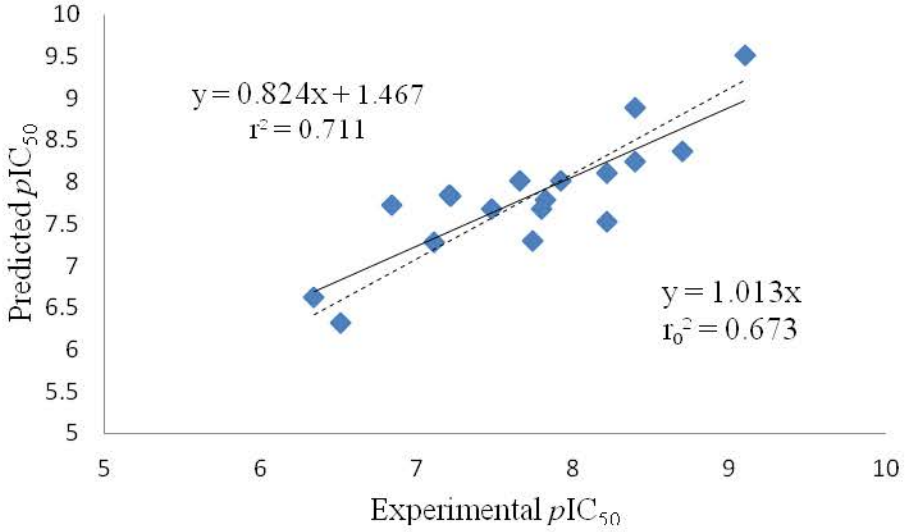

Fig. 4.1.5 Graph of experimental versus predicted activities of the test set compounds for the best CoMSIA model (SHA).

4.1.6.7 Tropsha's validation tests

A good model should pass the Tropsha's validation criteria: $r^2_{cv} > 0.5$, $r^2_{pred} > 0.6$, $[(r^2 - r^2_0)/r^2] < 0.1$ or $[(r^2 - r'^2_0)/r^2] < 0.1$ and $0.85 \leq k \leq 1.15$ or $0.85 \leq k' \leq 1.15$. Here, r^2 is squared correlation coefficient between observed and predicted values, r^2_0 is squared correlation coefficient between the observed and predicted values of the test set compounds with intercept set to zero and r'^2_0 is squared correlation coefficient between the predicted and observed values of the test set compounds with intercept set to zero. The k is the slope of line obtained through the observed and predicted values of the test set compounds whereas k' is the slope of line obtained through the predicted and observed values of the test set compounds. The best CoMSIA model (SHA) showed higher r^2_{cv} value of 0.571 which is generally considered as a reliable parameter for a good predictive QSAR model. The r^2_{pred} value of the best CoMSIA model (SHA) was

0.679. The next parameter $[(r^2 - r^2_0)/r^2] < 0.1$ or $[(r^2 - r'^2_0)/r^2] < 0.1$ indicates that at least one of the correlation coefficient for regression line passing through the origin r^2_0 or r'^2_0 should be close to r^2. $[(r^2 - r^2_0)/r^2]$ and $[(r^2 - r'^2_0)/r^2]$ values are observed as 0.0534 and 0.0197 respectively which are lower than 0.1 signifying a good QSAR model. The forth parameter ($0.85 \leq k \leq 1.15$ or $0.85 \leq k' \leq 1.15$) indicates that at least one slope of the regression lines passing through the origin should be close to one. The regression plots of experimental versus predicted activities and predicted versus experimental activities were constructed as shown in Fig. 4.1.5 and 4.1.6. The k and k' are observed to be 1.103 and 0.984 respectively, which are in the given range. Thus, all the validation parameters satisfy the mentioned criteria suggesting that the developed model is a reliable one.

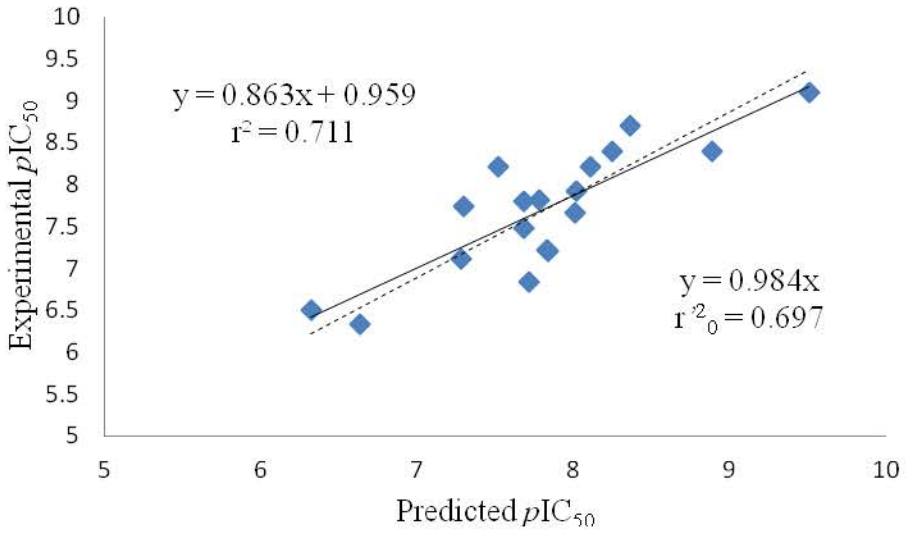

Fig. 4.1.6 Graph of predicted versus experimental activities of the test set compounds for the best CoMSIA model.

4.1.6.8 Applicability domain (APD)

It is not possible for any QSAR model, even if it is robust and validated, to predict the exact activity of all the compounds. The applicability domain defines the predictions for only those compounds to be reliable that fall into the domain.

Applicability domain was performed by using *Enalos KNIME nodes*,[254] designed and developed by Novamechanics Ltd (http://www.novamechanics.com/knime.php). Applicability domain is determined by two methods i.e. similarity measurement and leverage. Both the methods are based on distance-based approach in which distance of the query compound is calculated from a defined point within the descriptor space of the training set compounds. The equations

used for determining the similarity measurement and leverage are explained in experimental part. In similarity measurement method, APD was calculated 0.79 and all the test set compounds fell within the domain of applicability as shown in Table 4.1.5. Thus, all the predictions for the test set compounds using the model can be considered reliable. In the leverage method, the warning upper leverage limit was fixed at 0.17 and all the test set compounds showed the leverage value below this leverage limit as shown in Table 4.1.5 which indicated that the predictions for all the test set compounds were considered reliable. Thus, the results of both the tests (similarity measurement and leverage) offered the conclusion that the test set compounds fell into the domain of applicability.

Table 4.1.5 Applicability domain of test set compounds as determined by similarity measurement and leverage method.

Compd	Similarity measurements distance (Threshold APD = 0.79)	Leverage value (upper limit = 0.17)	Inference
1	0.18	0.03	reliable
5	0.12	0.04	reliable
9	0.22	0.05	reliable
12	0.19	0.02	reliable
19	0.25	0.04	reliable
21	0.18	0.04	reliable
23	0.15	0.05	reliable
37	0.21	0.05	reliable
38	0.13	0.04	reliable
39	0.22	0.05	reliable
42	0.16	0.05	reliable
49	0.27	0.04	reliable
50	0.14	0.02	reliable
54	0.29	0.13	reliable
58	0.22	0.08	reliable
61	0.16	0.05	reliable
62	0.09	0.05	reliable
65	0.29	0.08	reliable

4.1.6.9 Validation of the best model using external compounds reported in the literature

Nine external compounds (**a**-**i**), which were not part of the model development process, were used for external validation of the developed model. These compounds were selected from the literature covering rimonabant (**a**),[255] TM38837 (**b**),[97] AM6545

(**c**),[255] cyano group containing compounds (**d-g**)[141] and amide group bearing pyrazole derivatives (**h** and **i**)[142] having the reported activity in IC_{50} values. The predictive accuracy of the best developed 3D-QSAR model (SHA) was checked by matching the predicted biological activities with the experimentally determined ones. The predicted activities of all the compounds (**a-i**) were found to be matching quite closely to the actual values. The residual values were ranging from 0.24 to -0.28 as shown in Table 4.1.6 indicating that the developed model predicted the activity quite correctly and this also proved that the correlation shown by the best developed model (SHA) was not an accidental one. Applicability domain was also performed for these compounds indicating that all the compounds were within the range and the predicted activities were reliable ones as shown in Table 4.1.6. The graph of the experimental and predicted activities of the external set of compounds is shown in Fig. 4.1.7. Thus, the best developed 3D-QSAR model (SHA) could be universally utilised for further modification of the existing compounds or designing of novel compounds for CB1 receptor antagonist activity.

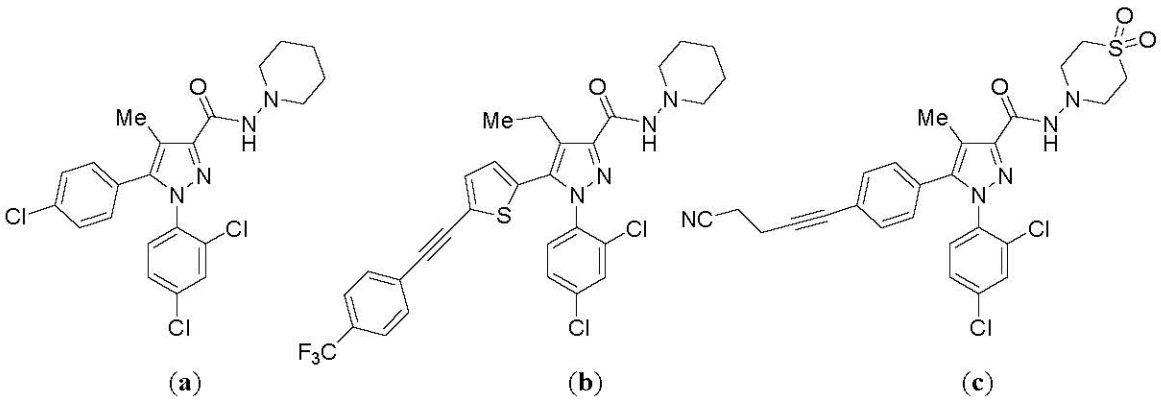

Comp	R
d	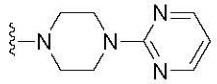
e	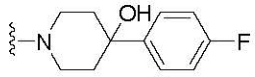
f	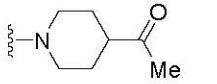
g	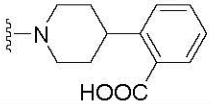

Comp	R
h	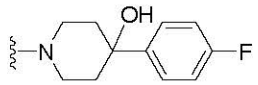
i	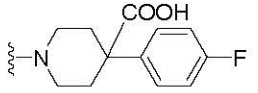

Table 4.1.6 Prediction of activity of external set of compounds (**a-i**) by using the best developed 3D-QSAR CoMSIA model (SHA).

Compd	Experimental activity (pIC_{50})	Predicted activity (pIC_{50})	Residual value	APD (0.79)	Leverage (0.17)	Inference
a	7.95	7.76	0.19	0.64	0.02	reliable
b	8.07	7.99	0.08	0.57	0.11	reliable
c	8.38	8.18	0.20	0.15	0.06	reliable
d	8.42	8.35	0.07	0.62	0.09	reliable
e	8.52	8.28	0.24	0.10	0.04	reliable
f	6.70	6.91	-0.21	0.39	0.04	reliable
g	5.55	5.83	-0.28	0.26	0.06	reliable
h	9.72	9.53	0.19	0.17	0.10	reliable
i	7.52	7.67	-0.15	0.27	0.07	reliable

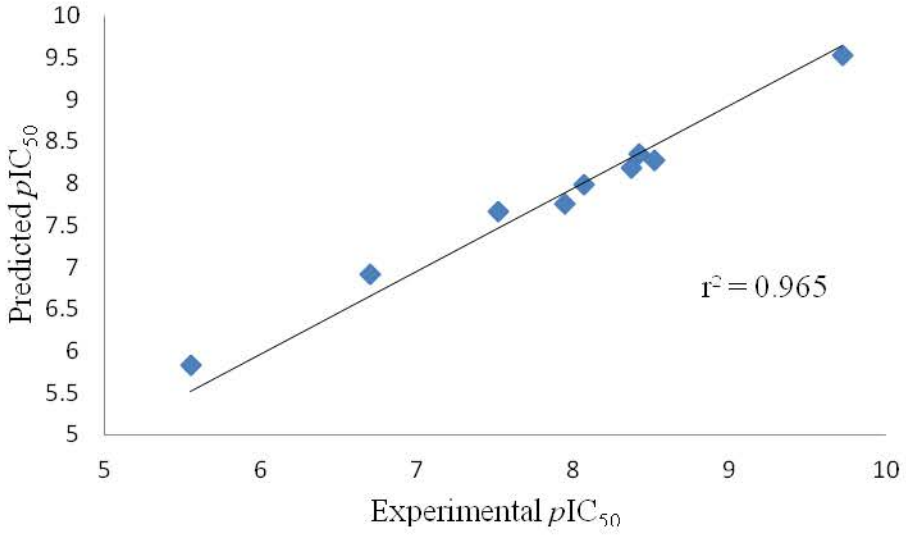

Fig. 4.1.7 Graph of experimental verses predicted activities of external compounds reported in the literature.

4.1.7 Graphical interpretation of the contour maps

In comparison to the best CoMFA model, the best CoMSIA (SHA) model exhibited better predictive accuracy. The contour maps of the best developed CoMSIA model have been discussed. The CoMSIA model contour maps are signifying the area in the space where the aligned compounds would interact favourably or unfavourably with the receptor. Visualisation of contour maps is useful to gain insight into the structural requirements for CB1 receptor antagonistic activity.

In the CoMSIA steric contour maps, green coloured contour maps (80 % contribution) represent the regions favourable for high steric tolerance while yellow coloured contour maps (20 % contribution) represent unfavourable regions. The template molecule (**20**) is shown in the contour map as shown in Fig. 4.1.8 in which the methyl group and phenyl ring at 4th and 5th positions of the pyrazole ring were oriented towards the green region as well as the oxadiazole ring and cyclopropane ring attached to the side chain at 3rd position of the pyrazole were also surrounded by the green region which could be the reason for good activity of the compound (**20**, IC_{50} = 0.1 nM). In compound (**4**), the *n*-propyl chain attached to the phenyl ring at 5th position and tetrazole ring attached to the side chain at 3rd position of pyrazole ring were embedded in the green region contributing positively towards the good activity (IC_{50} = 1.1 nM). Bulkier groups such as tetrazole in compound (**2**, IC_{50} = 0.5 nM), compound (**3**, IC_{50} = 0.1 nM) and compound (**65**, IC_{50} = 4 nM), oxadiazole in compound (**21**, IC_{50} = 0.8 nM), compound (**24**, IC_{50} = 0.1 nM) and compound (**25**, IC_{50} = 1 nM) were covered in the green region indicating that the bulkier group in this area were favourable for enhancement of biological activity. Pyridine ring attached to the 3rd position of the pyrazole ring of compound (**32**, IC_{50} = 2 nM) is also oriented near the green region resulting in good activity of the compound. Tetrazole ring in compound (**5**, IC_{50} = 22 nM), phenyl ring attached to the cyclopentane in compound (**64**, IC_{50} = 14 nM) and phenylethylamine group in compound (**29**, IC_{50} = 10 nM) were oriented between the green and yellow regions indicating moderate activity for these compounds. Bulky groups such as piperidine ring in compound (**39**, IC_{50} = 455 nM), piperazine ring in compound (**41**, IC_{50} = 900 nM), compound (**42**, IC_{50} = 310 nM), compound (**43**, IC_{50} = 855 nM), compound (**44**, IC_{50} = 633 nM) and compound (**45**, IC_{50} = 980 nM) were embedded in yellow region indicating that bulkier substituents in this area were unfavourable resulting in poor activity for these compounds. Tetrazole ring in compound (**53**, IC_{50} = 74 nM) and *H*-imidazolo[1,2-*a*]pyridine in compounds (**14**, IC_{50} = 88 nM) were also aligned towards yellow region which could be the reason for their poor activity.

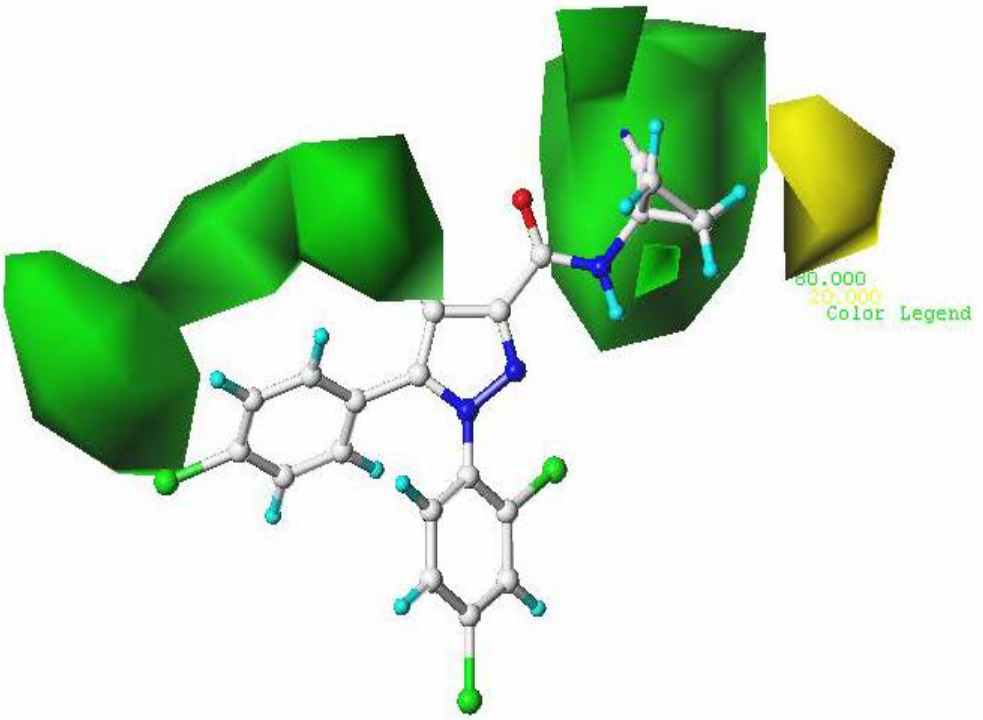

Fig. 4.1.8 CoMSIA steric contour map with the template molecule (**20**).

The CoMSIA hydrophobic contour maps with the template molecule (**20**) are shown in the Fig. 4.1.9. The cyan coloured contour maps depicted the favourable regions while the white contour maps depicted the unfavourable regions for hydrophobic substituents. The contributions of favourable and unfavourable regions are truncated to 80 and 20 % respectively. Trifluoromethyl group of the template molecule is oriented towards the cyan region which makes the compound more active. Part of the tetrazole ring of compound (**2**, IC_{50} = 0.5 nM) is present in the cyan region; trifluoromethyl group of compound (**17**, IC_{50} = 3 nM), compound (**21**, IC_{50} = 0.8 nM) and compound (**22**, IC_{50} = 0.4 nM) is present near the cyan region indicating that substituents with hydrophobic character in this region are favourable and show good activity. Methyl group at position 3 of tetrazole in compound (**72**, IC_{50} = 0.5 nM) is oriented near the cyan region resulting into good activity. Imidazothiazole ring of compound (**13**, IC_{50} = 11 nM) is present in between cyan and white regions indicating moderate activity for this compound. Pyrazine ring of compound (**33**, IC_{50} = 57 nM) is present near the white region whereas the tetrazole ring of compound (**1**, IC_{50} = 145 nM) is covered by the white region which are unfavourable for activity justifying their poor activities. The tetrazole [compound (**5**, IC_{50} = 22 nM)] and imidazole [compound

(**36**, IC_{50} = 20 nM)] rings are oriented near the white region contributing towards poor activity of these compounds.

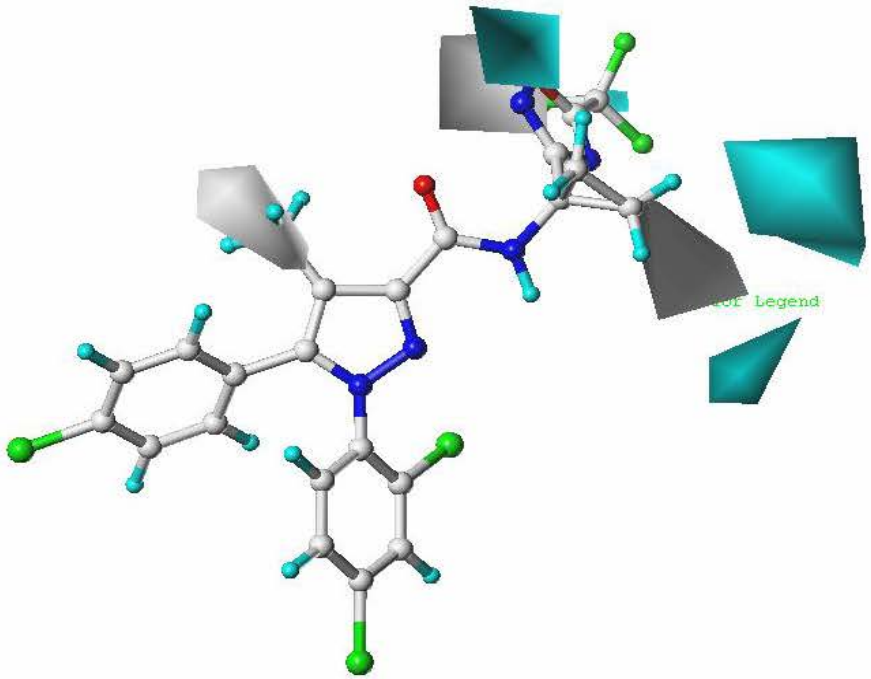

Fig. 4.1.9 CoMSIA hydrophobic contour map with the template molecule (**20**).

In hydrogen bond acceptor CoMSIA contour maps, the magenta colour (90 % contribution) represents the region favourable for hydrogen bond acceptor substituents whereas the orange coloured contour maps (10% contribution) represent the regions unfavourable for hydrogen bond acceptor groups. The template molecule (**20**) with CoMSIA hydrogen bond acceptor contour maps is showed in Fig. 4.1.10. Hydrogen bond acceptor groups like oxygen of oxadiazole ring of the template molecule embedded in the magenta region could be contributing for high antagonistic activity. Oxygen of the oxadiazole of compound (**21**, IC_{50} = 0.8 nM) and compound (**25**, IC_{50} = 1 nM) is embedded in the magenta region justifying high activity of both the compounds. Nitrogen of tetrazole of compound (**69**, IC_{50} = 8 nM) and compound (**70**, IC_{50} = 3 nM) present in between the magenta and orange regions offers moderate activity for these compounds. Nitrogen of tetrazole of compounds (**57**, IC_{50} = 100 nM), compound (**58**, IC_{50} = 61 nM), compound (**62**, IC_{50} = 77 nM) and compound (**67**, IC_{50} = 31 nM) is oriented towards the orange region causing poor activity for these compounds. Nitrogens of imidazole and pyrazine in compound (**35**, IC_{50} = 71 nM) and compound (**33**, IC_{50} = 57 nM) respectively, are oriented towards the orange region and

the nitrogen of imidazopyridine of compound (**15**, IC_{50} = 63 nM) is present near the orange region showing poor activity. Sulphur of thiazole ring of compound (**8**, IC_{50} = 15 nM) covered by the orange region and oxygen of the amide chain attached to the thiazole ring present near the orange region offer poor activity for the compound.

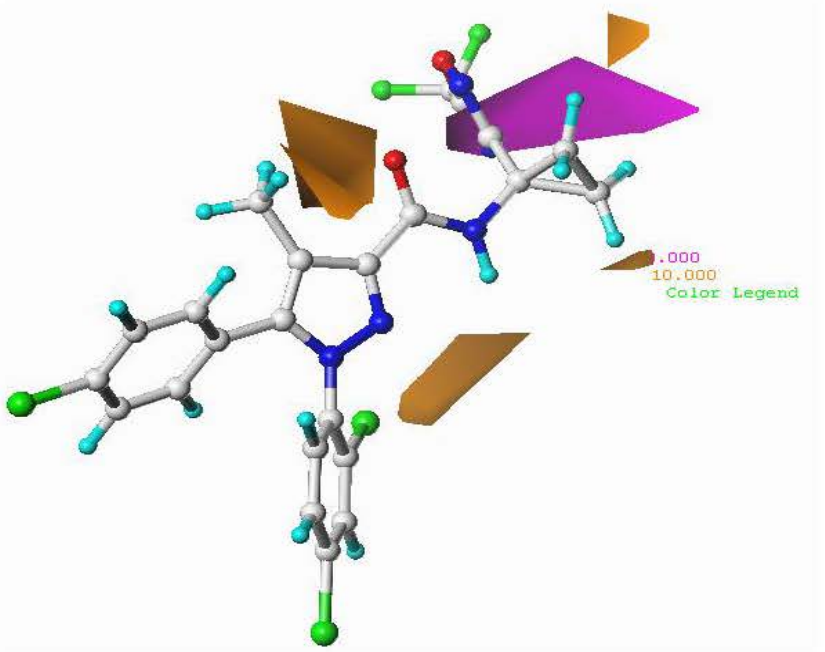

Fig. 4.1.10 CoMSIA hydrogen bond acceptor contour map with the template molecule (**20**).

4.1.8 Designing of novel CB1 receptor antagonists using the best developed CoMSIA model (SHA)

The best developed 3D-QSAR CoMSIA (SHA) model was having higher external predictive accuracy than the best CoMFA model. Hence, designing of novel lead compounds was performed using the contour maps generated by the best CoMSIA (SHA) model with the aim to have higher CB1 receptor antagonistic activity than the template molecule (**20**). One of the main strategies adopted was to design more polar and less lipophillic derivatives so that peripherally active compounds could be designed. Polarity and lipophilicity are governed by polar surface area (PSA) and logP, respectively. Both these properties for the compounds were calculated using Qikprop[256] software. Before calculating PSA and logP values of various compounds, the software was validated by calculating both of these properties for rimonabant, a known compound. The calculated values for rimonabant were found to be matching quite closely with the literature values [calculated PSA = 53.91 $Å^2$ (literature value = 50.2

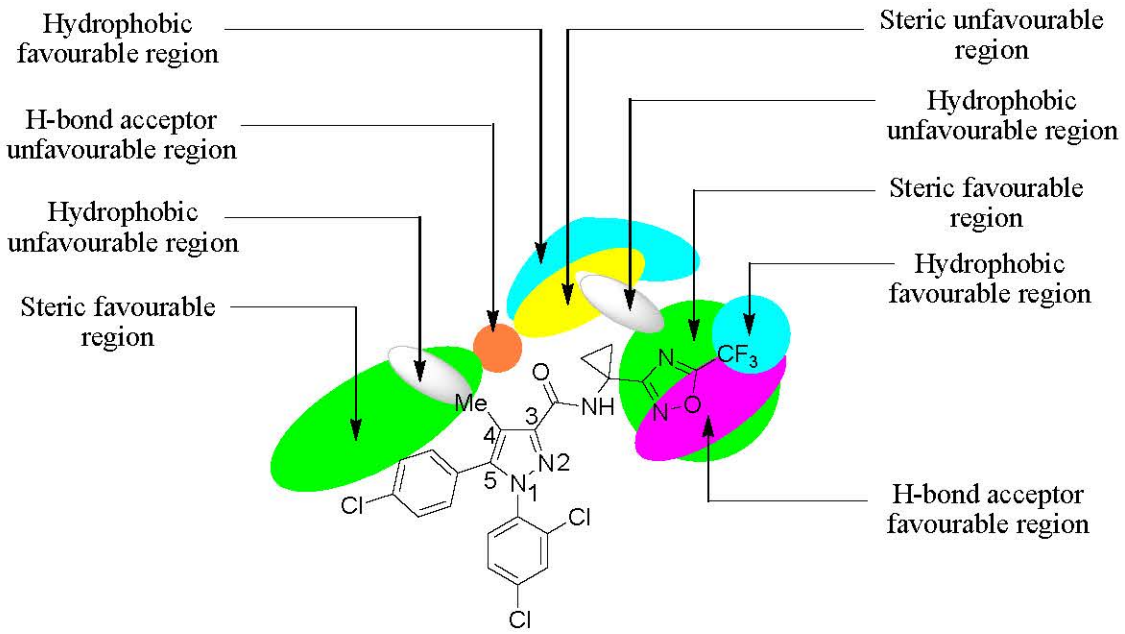

Fig. 4.1.11 Representation of contour maps of best CoMSIA model (SHA) with the template molecule (**20**).

Å^2); calculated logP = 6.30 (literature value = 6.47)].[141] The template molecule exhibited PSA value of 86.67 Å^2 and logP of 6.61. Thus, it was thought logical to modify the existing template molecule with the inputs obtained from the contour maps generated by the best CoMSIA model to design molecules with increased PSA and decreased logP values. A lot of modifications were tried by using different combinations of functional groups to enhance the biological activity of the template molecule with increased PSA and decreased logP values. Modifications which offered better results only have been discussed here. Since the steric contour maps are having green and yellow coloured contours for sterically favourable and unfavourable regions respectively, efforts were made to put bulky groups in the green region as shown in Fig. 4.1.11. Efforts were also made to put a polar and bulky triazole group in place of the methyl at 4th position of the pyrazole ring in green region offering PSA and logP values of 106.23 Å^2 and 5.92, respectively for the designed molecule. The predicted activity of this designed compound (**M1**) showed pIC$_{50}$ value of 9.94 which was quite close to the template molecule (pIC$_{50}$ = 10.00). The designed compound (**M1**) fell inside the applicability domain as determined by both similarity measurement and leverage method (Table 4.1.7). This indicated that replacement of the methyl group with triazole ring at 4th position is favourable for designing of CB1 receptor antagonists. Contour maps with reference to the designed compounds (**M1** and **M5**) are shown in Fig. 4.1.12.

Triazole ring was embedded in the green contours as shown in Fig. 4.1.12a. Further, the Cl was replaced with Br at 4th position of phenyl ring attached to the pyrazole ring at 5th position and it was observed that this modification caused an increase in the activity (pIC$_{50}$ = 10.04) with PSA value of 106.23 Å^2 and logP of 5.98 for compound (**M2**). Substitution with methoxy group was also favourable resulting into increased activity (pIC$_{50}$ = 10.16) with increased PSA value to 115.11 Å^2 and lowered logP, i.e. 5.50, for compound (**M3**). Green contour regions are also present on the right side covering the oxadiazole ring as shown in Fig. 4.1.11. Trifluoromethyl group was replaced with a more bulky group like phenyl which occupied the space in the green region. Biological activity of these compounds (**M4** and **M5**) also increased. Introduction of bulky phenyl ring in these compounds (**M4** and **M5**) led to increased logP. Contour maps of the designed compound (**M5**) clearly justify substitution of the triazole at 4th position because the triazole ring is embedded in green contour maps which are favourable for steric groups as shown in Fig. 4.1.12d. It is very much clear from the Fig. 4.1.12f that the triazole ring is not oriented towards orange contour map (H-bond acceptor unfavourable region). Similarly, phenyl substitution in the same region resulted into compound (**M6**) showing activity (pIC$_{50}$ = 10.06) with PSA 114.31 Å^2 and logP 6.15. Hydrophobic regions are indicated by cyan and white coloured contours as favourable and unfavourable regions respectively. Hydrophobic favourable region is present on trifluoromethyl group attached to the oxadiazole ring as shown in Fig 4.1.11. Substitution with hydrophobic groups like iodo in this region resulted into compounds (**M7**) with an increased activity (pIC$_{50}$ = 10.30), and a reasonable PSA value i.e. 109.00 Å^2 and a lowered logP value of 5.45. H-bond acceptor contour maps are depicted with magenta and orange colours for favourable and unfavourable regions respectively. Magenta region is covering the area of oxadiazole ring of the template molecule (**20**) as shown in Fig. 4.1.11. So, H-bond acceptor groups are embedded in this area. Replacement of trifluoromethyl with acetyl group resulted in compound (**M8**) showing good activity pIC$_{50}$ = 10.27 with increased PSA (136.13 Å^2) and lowered logP (4.46) values. Substitution with ethyl ketone in the same region resulted into compound (**M9**) having pIC$_{50}$ = 10.21, PSA = 134.00 Å^2 and logP = 4.76. Higher activity (pIC$_{50}$ = 10.61) is achieved by substituting acetyl group as H-bond acceptor in the favourable region in compound (**M10**) showing increased PSA and lowered logP. All the designed compounds are shown in Table 4.1.7.

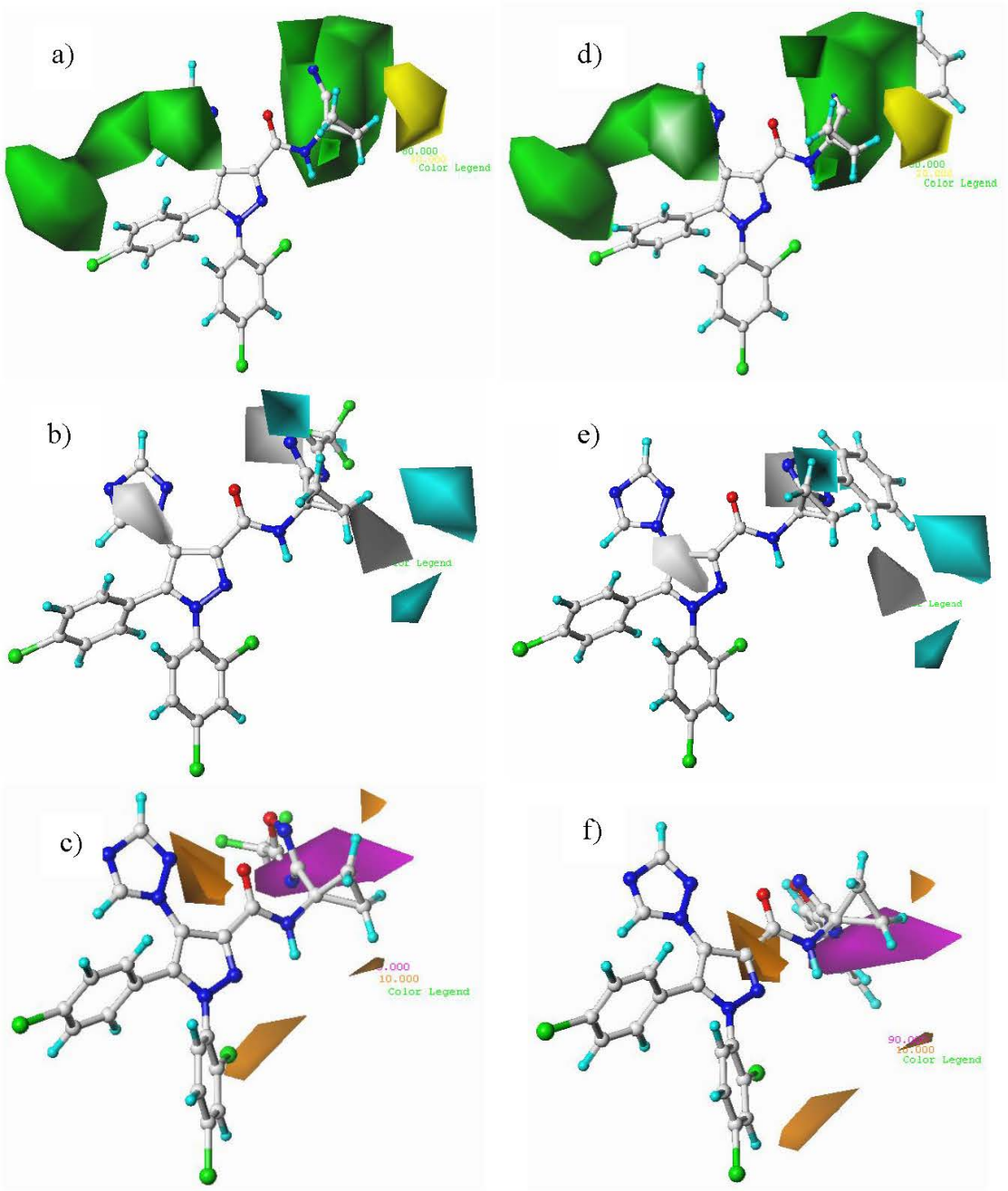

Fig. 4.1.12 Designed compound (**M1**) in a) CoMSIA steric contour map b) CoMSIA hydrophobic contour map c) CoMSIA hydrogen bond acceptor contour map and designed compound (**M5**) in d) CoMSIA steric contour map e) CoMSIA hydrophobic contour map f) CoMSIA hydrogen bond acceptor contour map.

Percentage oral absorption (human) and extent of central nervous system (CNS) activities were also predicted by Qikprop. Predicted CNS activity simply indicates whether a compound is CNS active or inactive. The scale is -2 (inactive) to +2 (active). All of the designed compounds (Table 4.1.7) showed oral absorption (human) in the range of 65.97 to 100.00 %. Rimonabant showed CNS activity score (+2) which

indicated the penetration of the drug in the CNS whereas the template molecule showed CNS activity score (+1) pointing out that the template molecule is less CNS active or more peripherally acting. The designed compounds (**M1-M7**) showed CNS activity score (-1) meaning that these compounds were more peripherally acting than the template molecule and rimonabant. The designed compounds (**M8-M10**) showed CNS activity score (-2) indicating the least penetration of these compounds in the CNS as shown in the Table 4.1.7. Hence, it can be inferred that steric, hydrophobic and hydrogen bond acceptor fields are the governing factors for the designing of peripherally active selective CB1 receptor antagonists. All the designed compounds have been checked for their novelty and were found to be so. The applicability domain was defined for the designed compounds (**M1-M10**) using similarity measurement and leverage method. All designed compounds fell inside the domain of applicability as shown in Table 4.1.7. The designed compound (**M10**) showed excellent *in silico* results which can be picked up as a lead molecule for further studies.

Table 4.1.7 Designed compounds (**M1-M10**).

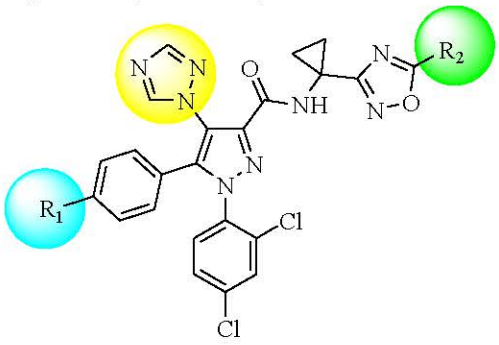

(M1-M10)

Compd	R_1	R_2	Predicted pIC_{50}	PSA	logP	% Oral absorption (human)	CNS Activity score	APD (0.79)	Leverage (0.17)
Rimonabant			7.76*	53.91	6.30	100.00	+2	-	-
20			9.75†	86.67	6.61	100.00	+1	-	-
M1	Cl	CF_3	9.94	106.23	5.92	87.90	-1	0.23	0.10
M2	Br	CF_3	10.04	106.23	5.98	88.23	-1	0.31	0.16
M3	OMe	CF_3	10.16	115.11	5.50	72.49	-1	0.50	0.02
M4	Cl	Ph	10.06	105.41	6.57	92.62	-1	0.09	0.06
M5	Br	Ph	10.66	105.41	6.63	92.94	-1	0.26	0.10
M6	OMe	Ph	10.06	114.31	6.15	77.19	-1	0.27	0.03
M7	I	I	10.30	109.00	5.45	83.43	-1	0.53	0.16
M8	Cl	COMe	10.27	136.13	4.46	65.97	-2	0.79	0.07
M9	Cl	COEt	10.21	134.00	4.76	73.46	-2	0.60	0.06
M10	**I**	**COMe**	**10.61**	**136.13**	**4.47**	**69.94**	**-2**	**0.54**	**0.13**

* Literature value = 7.95, † Literature value = 10.00

4.2 Development of pharmacophore and 3D-QSAR (atom-based) models using different scaffolds for the identification of essential features responsible for CB1 receptor antagonistic activity

Ligand-based drug designing approaches such as pharmacophore and 3D-QSAR[257,258] are based on the assumption that all the compounds interacting with a common target would share similar structural or physicochemical properties. Structural features such as aromatic ring, hydrophobic group, H-bond donor or H-bond acceptor groups etc. are important components of a pharmacophore model. These features are useful for characterization of structurally diverse compounds interacting with the same target.[259] In the discovery of novel lead compounds, pharmacophore modelling and 3D-QSAR techniques are powerful tools which may shed light on the essential structural features required for eliciting the desired biological activity. In the present work, a wide array of structures have been used involving six different scaffolds i.e. imidazoles, purines, pyrazines, piperazines, pyrazoles and pyrazolines to find out the common essential structural features for the peripherally acting CB1 receptor antagonists. The present study utilizes techniques like pharmacophore modeling and 3D-QSAR modeling.

4.2.1 Selection of dataset for pharmacophore and 3D-QSAR (atom-based) models

Various classes of selective CB1 receptor antagonists have been reported in the last few years. Initially, a set of 190 compounds from six different classes such as imidazole, purine, pyrazine, piperazine, pyrazole and pyrazolines were chosen from the literature.[111,118,136,148,167,181,192,199,200,218,223] The first criterion for the selection of the compounds was selectivity for peripheral receptors. Selectivity of CB1 receptor over CB2 receptor was also considered. Compounds having human CB1 receptor activity only were considered in the present study. Compounds whose stereochemistry and biological activity were not clearly defined were omitted from the study. Further, selections of the compounds were made on the basis of variations in the biological activity and chemical structures. The most active, moderately active and least active compounds of each scaffold were considered so that a robust data set could be prepared. For avoiding redundancy of information, compounds having similar biological activity and chemical structures were omitted from the final data set. Thirteen (13) compounds were removed due to ambiguous stereochemistry and

biological activities. Finally, a set of 25 compounds were selected for the present study. Rest of the compounds (**S1-S152**) were used as an additional external set for the purpose of validation. Biological activities of all these compounds were reported as K_i values (nanomolar) which were converted into their corresponding pK_i values by taking negative logarithm of K_i values in molar concentration (pK_i = - logK_i). The chemical structures of the model-building set are shown in Fig. 4.2.1. The pK_i values of all the selected compounds for developing a pharmacophore model were ranging from 5.074 to 10.046. The threshold pK_i values for actives and inactives were fixed to 7.5 and 6.6 respectively to get 8 active, 8 inactive and 9 moderately active compounds which were utilised for the development of pharmacophore model and the subsequent scoring function. For the 3D-QSAR modeling, the model-building set was divided into a training set and test set in the ratio of 4:1. There were 20 compounds in the training set and 5 compounds in the test set.

Pharmacophore hypothesis was developed using PHASE QSAR module of Schrodinger that employs a grid-based 3D-QSAR analysis.[260] Grid points nearest to the atoms in the molecule aligned to a selected reference compound were identified. Thus, the grid points so obtained were used to generate 3D descriptors for different types of interactions to correlate with the biological activities using PLS analysis.[251,252] Chemical structures of all the compounds were sketched and cleaned using 'building tools' option in Maestro molecular modeling software. All the sketched molecules were optimized using the LIGPREP version 2.3.[261] The optimized molecules were imported into PHASE for the development of common pharmacophore hypothesis (CPH) and the associated alignment. Conformers of all the compounds were generated using ConfGen search method with OPLS-2005 force field. A maximum of 1000 conformers per structure with 100 conformers per rotatable bond were generated by a preprocess minimization of 100 steps, and a distance-dependent dielectric solvation treatment was applied.

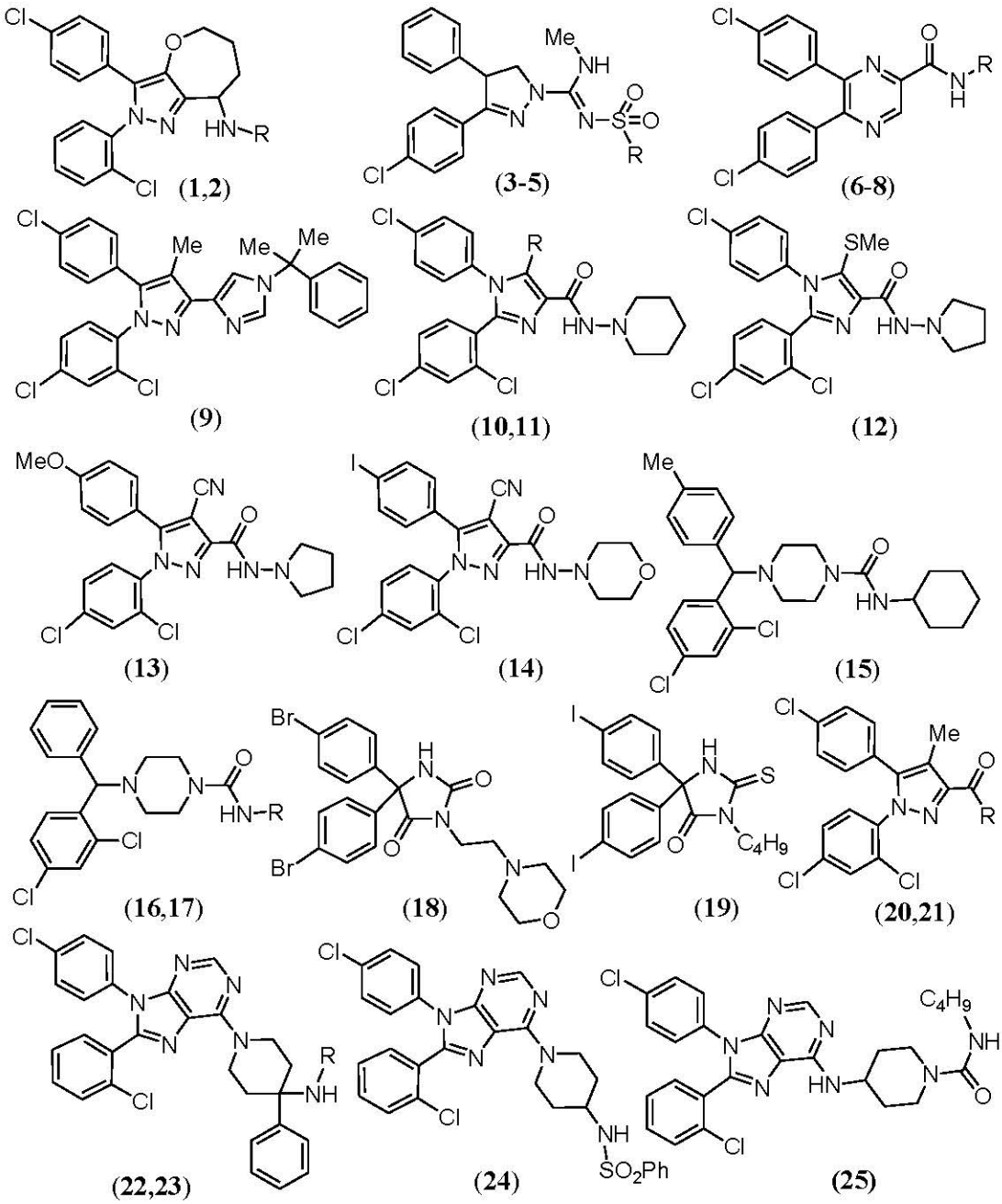

Compound	R	Compound	R	Compound	R
(1)	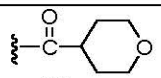	(7)	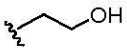	(20)	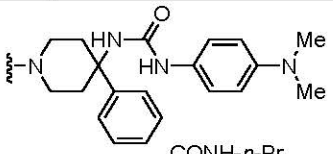
(2)	Me	(8)			
(3)	$N(C_2H_5)_2$	(10)	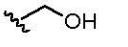	(21)	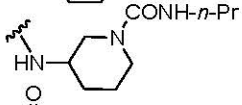
(4)	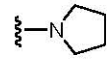	(11)	SC_2H_5		
(5)	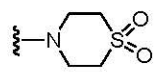	(16)	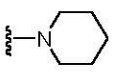	(22)	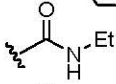
(6)	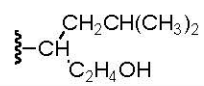	(17)	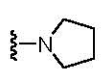	(23)	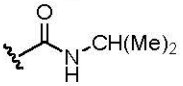

Fig. 4.2.1 Chemical structures of compounds (**1-25**) used for the development of pharmacophore model.

4.2.2 Pharmacophore modeling

This work was aimed to identify essential structural features for peripherally acting CB1 receptor antagonists. Active and inactive threshold pK_i values were fixed to 7.5 and 6.6 respectively resulting into 8 active, 8 inactive and 9 moderately active compounds. For developing a common pharmacophore hypothesis, all the 8 active compounds were utilised. Pharmacophore sites were created for all the compounds to get six different kinds of structural features such as H-bond acceptor, H-bond donor, hydrophobic, positive ionizable, negative ionisable and aromatic rings. The study resulted into three common structural features i.e. H-bond acceptors, hydrophobic groups and aromatic rings with frequencies of 1, 3 and 2 respectively. The software was restricted to find a minimum of 3 and maximum of 5 pharmacophoric sites wherein a condition was applied that 8 out of 8 active compounds must match all the sites. Several 3-point, 4-point and 5-point pharmacophore hypotheses were generated on the basis of the active compounds present in the dataset. In case of 5-point hypothesis, all the active compounds could not match with all the sites. AHHRR was the most probable 5-point hypothesis. AHH, AHR, ARR, HHH, HHR, HRR and AHHH, AHHR, AHRR, HHHR and HHRR were found to be the most probable hypotheses for 3-point and 4-point pharmacophore hypotheses in which all the active compounds matched all the sites. All the generated hypotheses were evaluated. The highest survival score was used to characterize the generated hypotheses. The survival scores ranged from 2.860 to 5.606. Top ranked survival score for 3-point hypothesis was obtained for AHR.72 i.e 3.060 whereas 4-point hypotheses AHHR.35 and AHRR.6 scored 2.860 and 5.606 respectively. Amongst all, the best hypothesis was obtained from the 4-point model (AHRR) having the highest survival score of 5.606 as shown in Table 4.2.1. The fitness scores of all the active compounds were observed for the best pharmacophore model AHRR.6. The active compound (**13**) was superimposed on the best model and it was observed that all the pharmacophoric features perfectly matched with a fitness score of 3.00 whereas the inactive compound (**19**) had a fitness score of 1.52 indicating that the developed pharmacophore model AHRR.6 has the capability to pick up the active compounds from the dataset. The best model (AHRR.6) containing one hydrogen bond acceptor, one hydrophobic group, and two aromatic rings is shown in Fig. 4.2.2. The A5 acceptor feature correctly mapped on the oxygen of carbonyl amide group attached to 3rd position of the pyrazole ring, H9 hydrophobic features mapped on the 4-Cl group of the phenyl ring at 5th position of the pyrazole ring and the two R12 and R13

aromatic rings perfectly mapped on the phenyl rings attached to 1st and 5th positions of the pyrazole ring. The distances and angles of AHRR.6 of the pharmacophore features are given in Table 4.2.2 and 4.2.3. The three top ranked pharmacophore models AHR, AHHR and AHRR were then used to align the molecules for the development of atom-based 3D-QSAR analysis. The best QSAR model was characterized by various statistical measures and regression contours. The accuracy of the developed models was verified by the statistical data such as r^2_{ncv} and r^2_{cv}.

Table 4.2.1 Data of the top ranked pharmacophore models

ID	Survival	Survival-inactive	Post hoc score	Site	Vector	Volum	Selectivity	Match
AHR.72	3.060	1.260	3.061	0.63	0.912	0.519	1.072	8
AHHR.35	2.860	1.179	2.864	0.53	0.893	0.441	1.411	8
AHRR.6	**5.606**	**3.527**	**3.192**	**0.72**	**0.900**	**0.572**	**1.463**	**8**

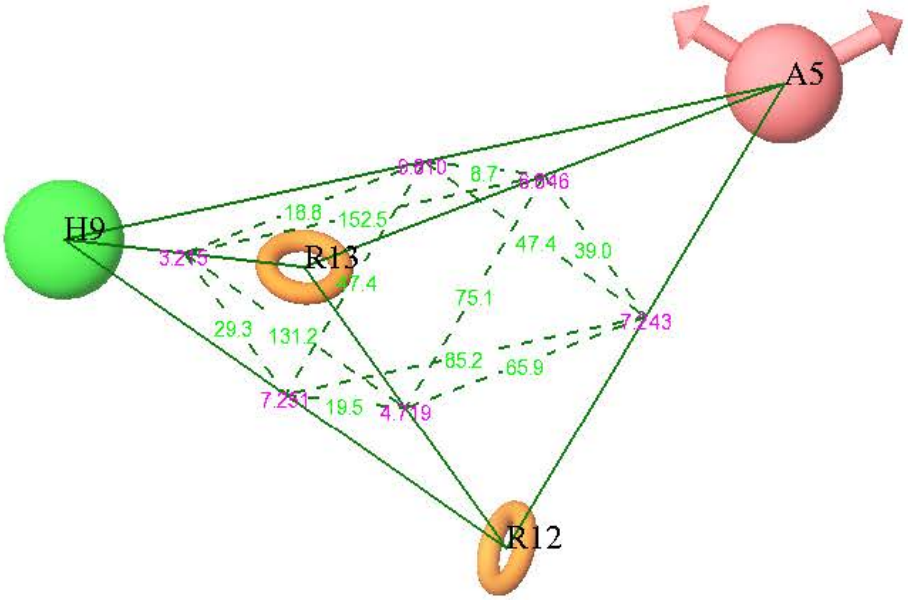

Fig. 4.2.2 Distances and angels of the best developed pharmacophore model AHRR.6. Orange coloured torus represents aromatic rings (R12 and R13), green coloured sphere represents hydrophobic group (H9), and light red coloured vector represents hydrogen bond acceptor (A5). Purple colour represents distances and green colour represents the angles between the pharmacophoric features.

Table 4.2.2 Distances between the two different pharmacophoric features of AHRR.6 model.

Site 1	Site 2	Distance (Å)
A5	H9	9.810
A5	R13	6.846
A5	R12	7.243
H9	R13	3.215
H9	R12	7.251
R13	R12	4.719

Table 4.2.3 Angles among the different pharmacophoric features of AHRR.6 model.

Site 1	Site 2	Site 3	Angle
H9	A5	R13	8.7
H9	A5	R12	47.4
R13	A5	R12	39.0
A5	H9	R13	18.8
A5	H9	R12	47.4
R13	H9	R12	29.3
A5	R13	H9	152.5
A5	R13	R12	75.1
H9	R13	R12	131.2
A5	R12	H9	85.2
A5	R12	R13	65.9
H9	R12	R13	19.5

4.2.3 Analysis of 3D-QSAR (atom-based) model

In the present study, atom-based 3D-QSAR models were developed because atom-based 3D-QSAR considers the entire molecular space while pharmacophore-based 3D-QSAR (like CoMFA and CoMSIA) does not consider the chemical space beyond the pharmacophoric groups. Thus, atom-based 3D-QSAR is more advantageous than pharmacophore-based 3D-QSAR for the development of a good QSAR model.[262] The molecular alignment obtained through pharmacophore generation was used to generate 3D-QSAR model by using partial least square (PLS) factors. A maximum of 4 PLS factors were allowed. Each atom in the atom-based model served as a sphere. The training set compounds were covered with a regular grid of cubes. Each cube represented upto six "bits", meaning six different classes of atoms including H-bond donor (D), hydrophobic or non polar (H), negative ionic (N), positive ionic (P), electron-withdrawing (W) and others (X). The alignment generated from the

pharmacophore model was utilised for the development of 3D-QSAR models. The developed models were evaluated by different parameters such as cross-validated coefficient, noncross-validated coefficient, F-value, predictive r^2, modified r^2, Pearson-R etc.

Several 3D-QSAR models were generated and each generated model was validated by the internal test set compounds. Although a number of models were generated but only the top ranked models have been discussed here. The 3D-QSAR model obtained by using the 3-point pharmacophore hypothesis (AHR.72) for the purpose of alignment showed r^2_{ncv} = 0.967, r^2_{cv} = 0.518, SD = 0.331, PLS factor = 4, F-value = 87.2, RMSE = 0.490, Pearson-R = 0.923 and stability = -0.507, while the 3D-QSAR model obtained by using the alignment on 4-point pharmacophore hypothesis (AHHR.35) showed r^2_{ncv} = 0.997, r^2_{cv} = 0.702, SD = 0.063, PLS factor = 4, F-value = 2435.9, RMSE = 0.523, Pearson-R = 0.852 and stability = -0.137 (Table 4.2.4). The best 3D-QSAR model got developed using the alignment based on 4-point pharmacophore hypothesis (AHRR.6) having r^2_{ncv} = 0.990, r^2_{cv} = 0.938, SD = 0.164, PLS factor = 4, F-value = 389, RMSE = 0.144, Pearson-R = 0.982 and stability = 0.016. The statistical parameters of the 3D-QSAR models are shown in Table 4.2.4. Predicted pK_i values (by the best developed AHRR.6 model) and residuals of the experimental (actual) and predicted pK_is are shown in Table 4.2.5.

Table 4.2.4 Statistical parameters obtained for the 3D-QSAR models obtained from various alignments.

Statistical parameters	AHR.72	AHHR.35	AHRR.6
r^2_{ncv}	0.967	0.997	**0.990**
r^2_{cv}	0.518	0.702	**0.938**
PLS factor	4	4	**4**
F-value	87.2	2435.9	**389**
Stability	-0.507	-0.137	**0.016**
RMSE	0.490	0.523	**0.144**
SD	0.331	0.063	**0.164**
Pearson-R	0.923	0.852	**0.982**

Table 4.2.5 Experimental and predicted pK_i values and the residuals of training and test set compounds by using the best developed 3D-QSAR model (AHRR.6) with fitness score.

Compd ID	Experimental pK_i	Predicted pK_i	Residual	Fitness score
1	10.04	9.95	0.09	1.82
2*	7.33	7.44	-0.11	2.07
3	7.52	7.61	-0.09	2.15
4*	6.63	6.62	0.01	2.18
5	6.08	6.15	-0.07	2.14
6	7.85	7.67	0.18	1.79
7	5.07	5.38	-0.31	1.78
8	6.75	6.47	0.28	1.78
9	10.00	10.10	-0.10	2.59
10*	7.46	7.63	-0.17	2.59
11	7.29	7.28	0.01	2.53
12*	8.05	7.98	0.07	2.54
13	8.69	8.67	0.02	3.00
14	6.88	6.84	0.04	2.20
15	9.82	9.88	-0.06	2.08
16	7.25	7.07	0.18	1.97
17	6.13	6.42	-0.29	1.93
18	7.15	7.25	-0.10	1.57
19	6.14	6.02	0.12	1.52
20	5.82	5.84	-0.02	1.90
21	6.56	6.56	0.00	2.55
22	6.71	6.71	0.00	2.39
23*	6.47	6.72	-0.25	2.47
24	8.92	9.00	-0.08	2.39
25	5.47	5.34	0.13	2.44

* Test set compounds

4.2.3.1 Validation of the best developed 3D-QSAR model (AHRR.6)

4.2.3.1.1 Validation by statistical parameters

A statistically validated 3D-QSAR model is a pre-requisite for reliable predictions. Several statistical parameters such as r^2_{ncv}, r^2_{cv}, SD, RMSE, F-value etc. can be used for the evaluation of a reliable and robust model. Higher r^2_{ncv} and r^2_{cv} values of 0.990 and 0.938 respectively revealed that the developed 3D-QSAR model possessed high internal predictive capability. $[(r^2 - r^2_0)/r^2]$ and $[(r^2 - r'^2_0)/r^2]$ values obtained were 0.016 and 0.007 respectively which were less than 0.1. The values of *k*

and *k*' were obtained as 1.011 and 0.988 respectively (Fig. 4.2.3 and 4.2.4). The F-value for the best 3D-QSAR model was 389 [F_{05} (4,19) = 4.5 (Tab)] at 99 % confidence level which indicated that the developed model was statistically highly significant. The SD and RMSE values of 0.164 and 0.144 respectively were quite near to each other. High Pearson-R value (0.982) indicated a good ranked correlation between the experimental and predicted activities for the test set compounds. Predictive r^2 (r^2_{pred}) for the test set compounds was found to be 0.925 and r^2_m = 0.843 indicated robustness of the model. On the basis of threshold value (active > 7.5, inactive < 7.5), sensitivity of the best model was observed as 88.89 % indicating that 88.89 % of compounds were correctly predicted "actives" out of the total "actives" whereas specificity was observed as 100 % which indicated that 100 % of compounds were correctly predicted "non-actives" out of the total "inactives". Accuracy of the best developed model was observed as 96 % which referred to the proportion of correctly predicted as "true active" or "true inactive". PPV was observed as 100 % indicting the probability of correct positive prediction whereas NPV was observed as 94.12 % indicating the probability of correct negative prediction. MCC was observed as 91.46 % which measured the quality of the binary classification, indicating very good prediction. Thus, it is revealed from the statistical parameters that a reliable model has been successfully developed.

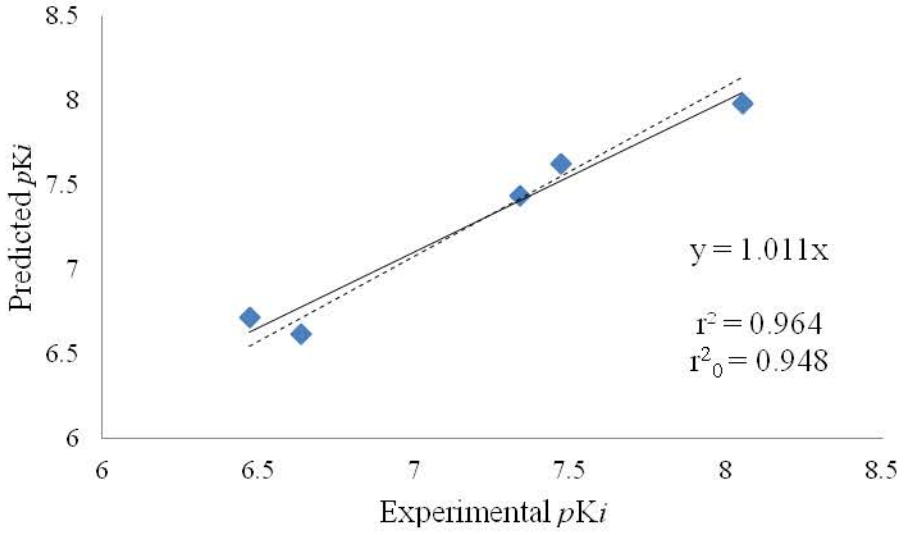

Fig. 4.2.3 Graph of experimental versus predicted activity of test set compounds.

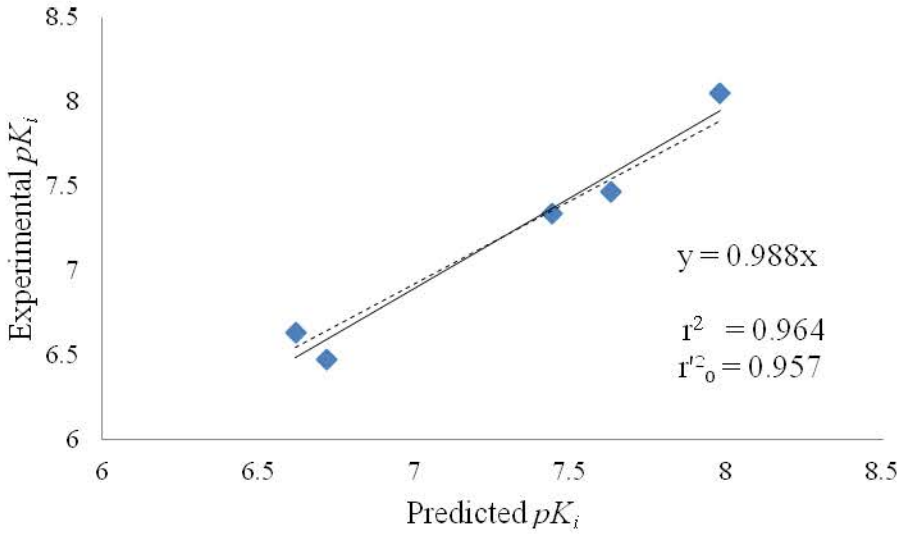

Fig. 4.2.4 Graph of predicted versus experimental activity of test set compounds.

4.2.3.1.2 Additional validation of the model using external data set

External data set containing 152 compounds (**S1-S152**), which were not included in the model development process, were used for the true validation of the best developed model. The predictive capability of the best developed model was further evaluated by comparing the predicted activities with the experimental ones. The predicted activities of the external set compounds (**S1-S152**) were quite close to the experimental activities. The experimental and predicted activities of the compounds (**S1-S152**) are shown in Table S1 (supplementary data). The graph plotted between the experimental and predicted activities of the external set compounds is shown in Fig. 4.2.5. The correlation coefficient r^2 was observed as 0.705 indicating that the developed model has good accuracy for predicting the biological activity of the non-evaluated compounds.

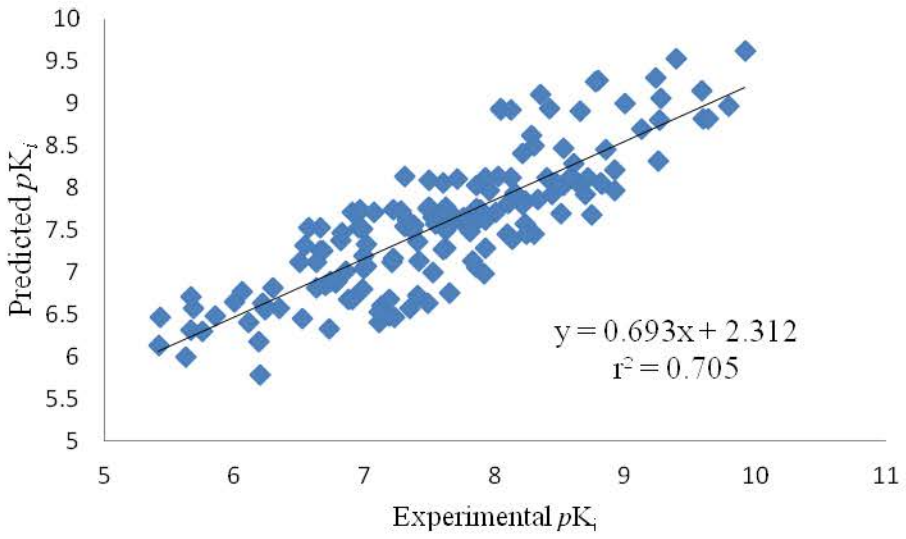

Fig. 4.2.5 Graph of experimental versus predicted activities of external set compounds (**S1- S152**).

4.2.3.1.3 Applicability domain (APD)

It is not always possible to predict the correct activity of all the compounds for any QSAR model even if it is validated with several parameters. APD is defined as "the response and the chemical structure space in which the QSAR model makes predictions with a given reliability".[263] It is used to find the compounds that are outside the APD and identifying the outliers from the training set compounds. APD was calculated for training, test, external test set compounds and the virtual screening hits by using the programme "APD using standardization approach".[263] The obtained results indicated that there were no outliers present in the training set and it was also observed that the test set, external test set and hits obtained from virtual screening were all inside the APD affirming the reliability of the developed 3D-QSAR model.

4.2.3.2 Graphical interpretation of the developed 3D-QSAR (atom-based) model

The contour maps obtained from the best 3D-QSAR model can provide insights into the structural features required for CB1 receptor antagonistic activity. The effects associated with the positive and negative regression coefficients of H-bond donor, hydrophobic, negative ionic, positive ionic, electron-withdrawing and other features could be visualized by PHASE. Visualization of the 3D-QSAR model can be done by using "regression coefficient visualization" or "effects" from atom-based or pharmacophore-based types in the grid-based 3D-QSAR methods. In the present study, effects of each pharmacophoric feature were observed with their positive and negative

regression coefficients around the pharmacophore hypothesis to identify the favourable and unfavourable regions for the activity. The positive and negative coefficients are depicted in blue-coloured and red-coloured cubes respectively in all the maps (Fig. 4.2.6-4.2.9).

4.2.3.2.1 Effect of substitution of bulky groups

With the inputs obtained from the generated contour maps due to the bulk of the groups, it was observed that bulky substituents in the blue coloured cubes favoured the activity whereas such substituents in the red coloured cubes disfavoured the activity (Fig. 4.2.6). The steric effects are visualized at positive and negative regression coefficient threshold of 0.006 and -0.006 respectively. Bulky substituents such as tetrahydropyran ring attached to amide in the most potent compound (**1**) in the dataset is oriented towards blue region which is favourable for the high activity (Fig. 4.2.6a) whereas the side chain attached to the pyrazine ring in compound (**7**) oriented towards red region might be a reason of its poor activity (Fig. 4.2.6b). Substituent like dimethyl at 3rd position of the imidazole ring in compound (**9**) orientated towards the blue coloured cubes (present towards right hand side of the Fig. 4.2.6c favourable region for bulky substituents) may be responsible for good activity of compound (**9**) whereas in compound (**21**), the bulky substituent like propane attached to the 3rd position of the piperidine ring is oriented towards the red coloured cubes (present at top of the Fig. 4.2.6d; this red coloured region is not favourable for the bulky substituents) so this could be one of the reasons for poor activity of compound (**21**). Bulky substituent like cyclohexane attached to carboxamide at 4th position of the piperazine ring in compound (**15**) was observed near to the blue coloured cubes (present towards right hand side of Fig. 4.2.6e, which favoured the bulky substituents) thus, this could be the reason of compound (**15**) having good activity. Pyrrolidine ring attached to the carboxamide at 4th position of the piperazine ring in compound (**17**) is oriented towards the red coloured cubes (present at the top of the Fig. 4.2.6f). This red coloured area is unfavourable for the bulky substituents, hence leading to poor activity for compound (**17**).

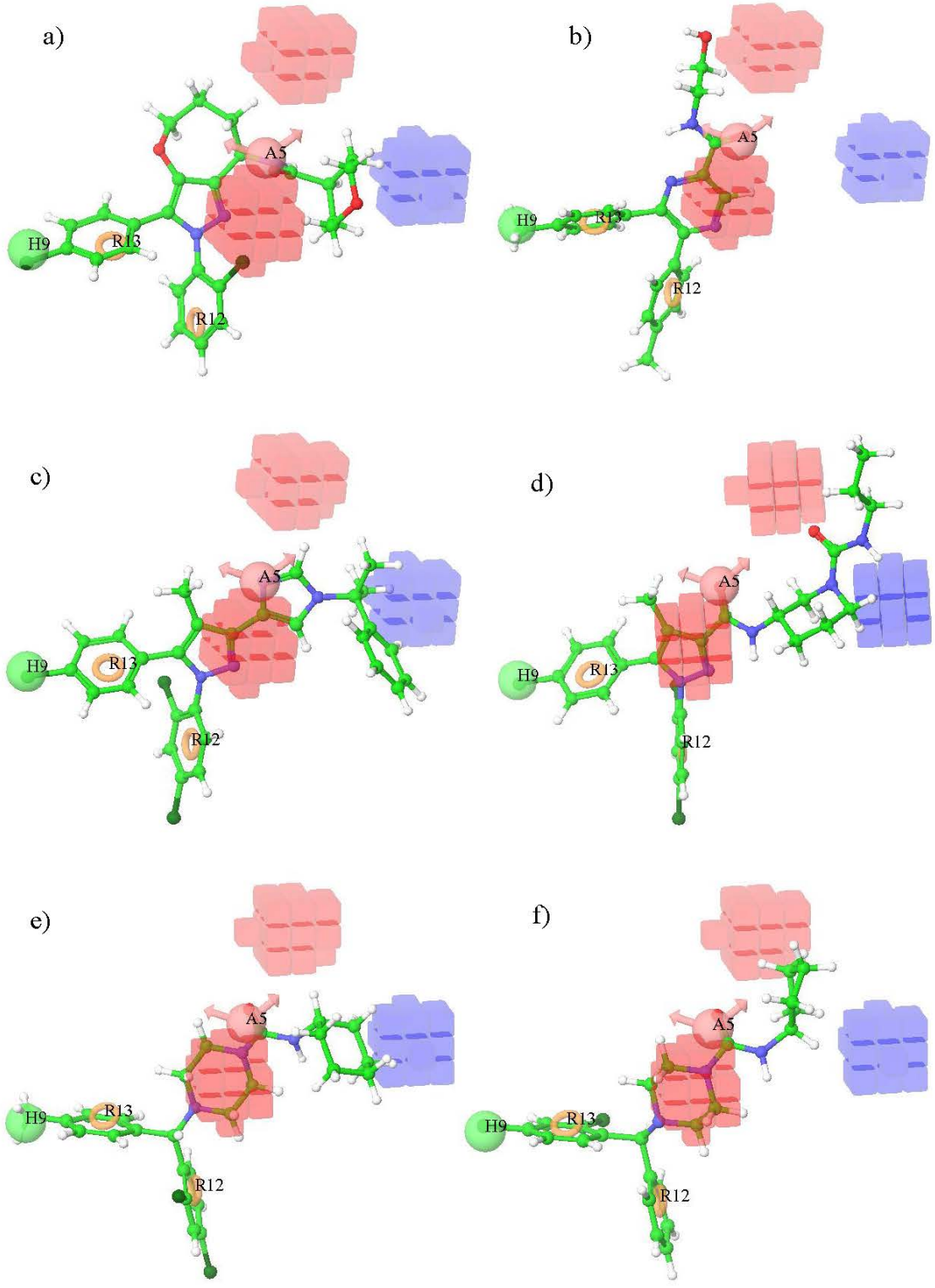

Fig. 4.2.6 Effects of bulky substituents on a) active compound (**1**), b) inactive compound (**7**), c) active compound (**9**), d) inactive compound (**21**), e) active compound (**15**) and f) inactive compound (**17**).

4.2.3.2.2 Effect of electron withdrawing groups

For understanding the effect of electron-withdrawing groups, a few examples of active and inactive compounds with substituents projecting into the cubes are depicted in Fig. 4.2.7. Electron-withdrawing effects are visualized at positive and negative regression coefficient thresholds of 0.01 and -0.01 respectively. Electron withdrawing groups such as oxygen atom of the carbonyl group and tetrahydropyran ring in compound (**1**) were present in the blue regions which are favourable for good activity (Fig. 4.2.7a) whereas oxygen of hydroxyl group of compound (**7**) is embedded in the red region thus offering poor activity (Fig. 4.2.7b). Oxygen atoms of the SO_2 group at 4^{th} position of the piperidine ring in compound (**24**) acting as electron withdrawing groups are embedded in the blue-coloured cubes (favourable region present towards the right hand side of the Fig. 4.2.7c) justifying the high activity of compound (**24**) whereas oxygen atom of the carbonyl group attached at 4^{th} position of the piperidine ring forming a side chain in compound (**23**) acts as electron-withdrawing group, and this carbonyl group embedded in the red-coloured cubes (unfavourable region present towards right hand side of the Fig. 4.2.7d) might be responsible for poor activity of compound (**23**). Electron-withdrawing group like cyano at 4^{th} position of pyrazole ring in compound (**13**) oriented towards blue coloured cubes (present at upper left hand side of the Fig. 4.2.7e) as well as nitrogen of the pyrrolidine ring attached to 3^{rd} position of the pyrazole ring side chain embedded in the blue coloured cubes (present at the centre of the Fig. 4.2.7e) could be responsible for high activity of compound (**13**). On the other hand, electron-withdrawing group like oxygen of carbonyl group attached to 3^{rd} position of the piperidine ring in compound (**21**) is embedded in the red coloured cubes (present towards left hand side of the Fig. 4.2.7f), which disfavoured the electron-withdrawing group in this area could be one of the reasons for compound (**21**) exhibiting poor activity.

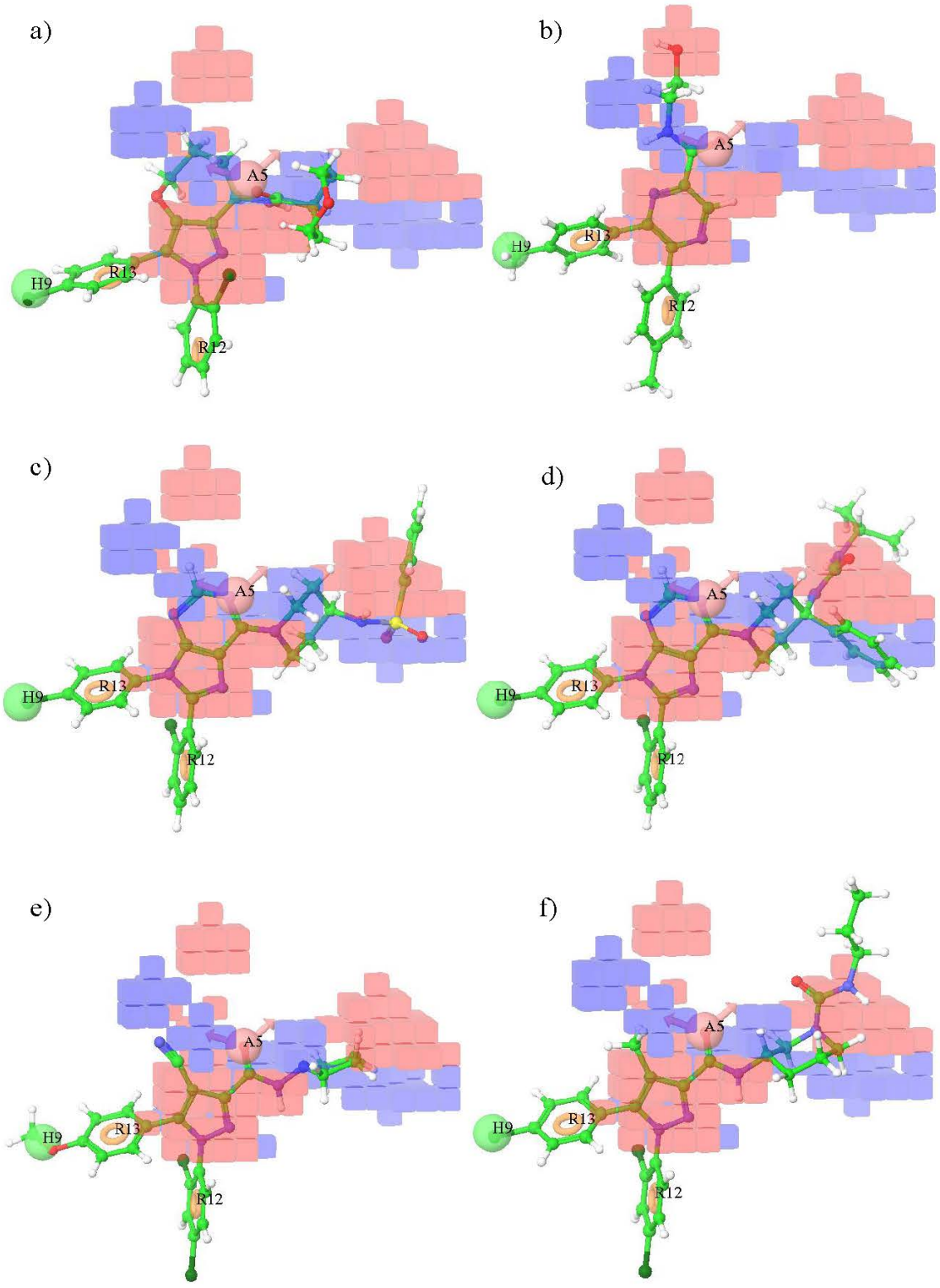

Fig. 4.2.7 Effect of electron withdrawing groups on a) active compound (**1**), b) inactive compound (**7**), c) active compound (**24**), d) inactive compound (**23**), e) active compound (**13**) and f) inactive compound (**21**).

4.2.3.2.3 Analysis of H-bond donor effects

For the convenience and clarify, the H-bond donor effects are visualized at a positive coefficient threshold of 0.01 and negative coefficient threshold of -0.01. The active and inactive compounds with their H-bond donor groups are considered to explain the background behind the differences in their activity on the basis of the generated contour maps. Blue coloured cubes indicate that H-bond donors are favoured in this region for high activity of a compound while red coloured cubes indicate unfavourable regions for the activity. Hydrogen bond donor group present in compound (**1**) like NH of amide in the side chain is oriented near the blue-coloured cubes (present in almost centre of the Fig. 4.2.8a, a favourable region for the activity) imparting high activity to compound (**1**) whereas NH group at 8 position of oxepine ring in compound (**2**) is partially embedded in the red-coloured cubes (present at the centre of the Fig. 4.2.8b), an unfavourable region for activity, thus compound (**2**) could be expected to exhibit poor activity. In compound (**6**), the hydroxyl group present in the side chain attached to the 3-position of pyrazine ring acting as hydrogen bond donor is embedded in the blue coloured cubes (present on the left side of the contour maps as shown in Fig. 4.2.8c) could be one of the reasons for high activity of compound (**6**). Whereas, the hydroxyl group present in the side chain attached to 3rd position of pyrazine ring in compound (**7**), embedded in the red coloured cubes (present at top of the Fig. 4.2.8d, an unfavourable region for H-bond donor), justifies the poor activity of compound (**7**). Likewise, the NH group attached to 4th position of piperidine ring in compound (**24**) acting as H-bond donor is covered in the blue coloured cubes (at right side of the Fig. 4.2.8e, a favourable region for the activity) and this could be responsible for its high activity. Whereas in compound (**25**), two hydrogen bond donor groups are present, in which first NH attached to the butyl side chain is embedded in the red-coloured cubes (present at right hand side of the Fig. 4.2.8f) and the second NH attached to 6-position of the purine ring is also embedded in the red-coloured cubes (present at almost centre of Fig. 4.2.8f), both unfavourable regions for the activity, hence compound (**25**) should have shown poor activity.

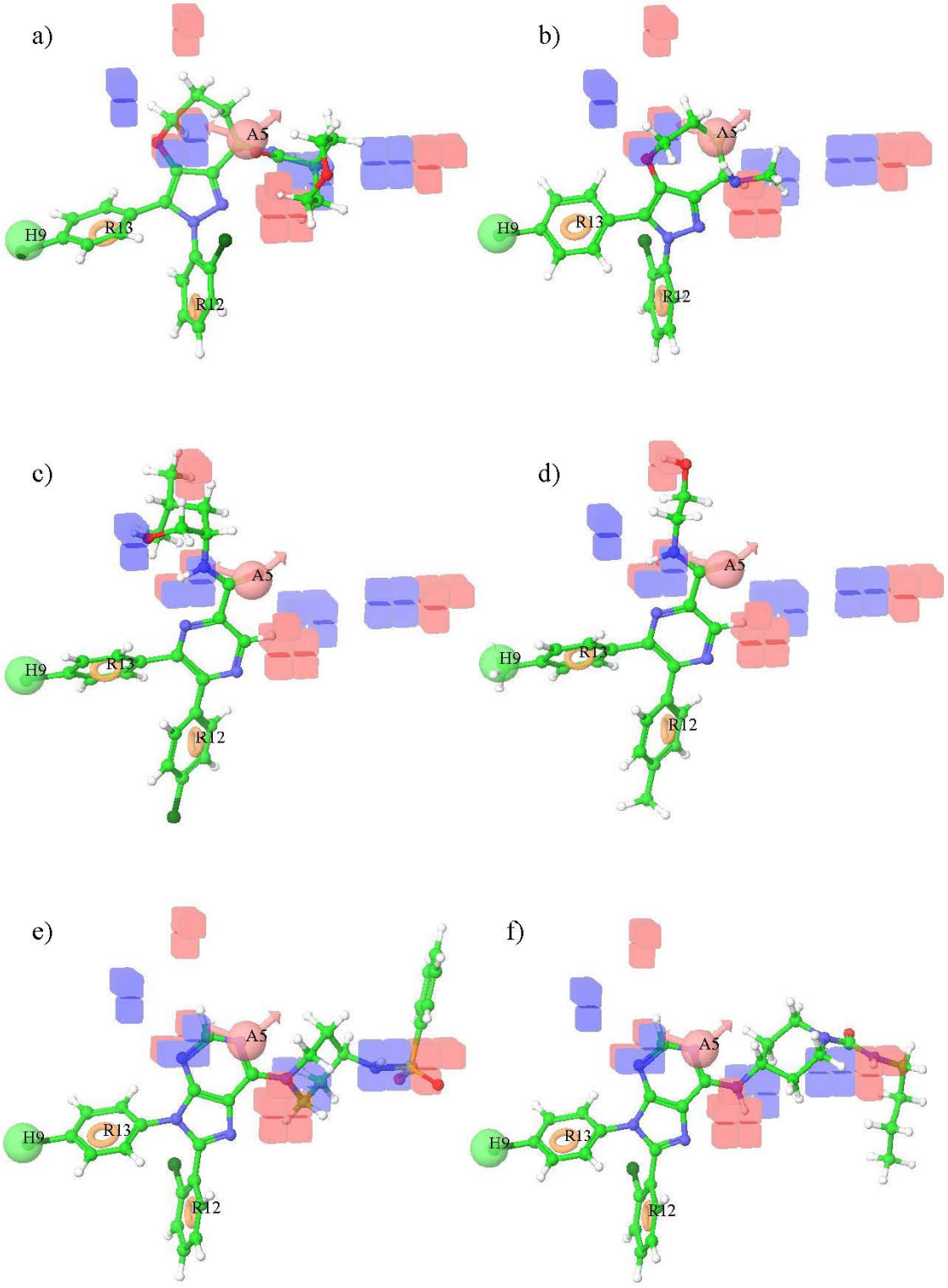

Fig. 4.2.8 Maps of H-bond donor effects on a) active compound (**1**), b) inactive compound (**2**), c) active compound (**6**), d) inactive compound (**7**), e) active compound (**24**) and f) inactive compound (**25**).

4.2.3.2.4 Effect of hydrophobic groups

Hydrophobic effects are visualized at a positive regression coefficient threshold of 0.015 and negative regression coefficient threshold of -0.015 for interpretation of the active and inactive compounds (Fig. 4.2.9). Phenyl ring attached to SO_2 group in compound (**24**) acting as a hydrophobic group is oriented towards blue-coloured cubes (present at the right side top corner of Fig. 4.2.9a) having positive coefficient for the activity and this could be the reason for good activity of compound (**24**) whereas in compound (**23**), the phenyl ring attached to 4^{th} position of the piperidine ring is oriented towards red-coloured cubes (present at the right hand side of Fig. 4.2.9b) leading to poor activity of the compound (**23**). Hydrophobic group like diethyl attached to SO_2 in compound (**3**) is embedded in the blue-coloured cubes (present at top of the Fig. 4.2.9c), a favourable region for the activity thus exhibiting good activity for compound (**3**), whereas the hydrophobic *n*-propyl group attached to the amide group in compound (**21**) is oriented towards red coloured cubes (present at right top of the Fig. 4.2.9d) indicating the negative coefficient and thus, compound (**21**) exhibited poor activity. Hydrophobic group like phenyl attached to 1^{st} position of imidazole ring in compound (**9**) embedded in the blue-coloured cubes (towards right hand side of the Fig. 4.2.9e) is a favourable region for the activity and this could be the reason for good activity of compound (**9**) whereas the butyl group attached to the amide in compound (**25**) is oriented towards red-coloured cubes (present towards right side corner of the Fig. 4.2.9f), an unfavourable region for the activity leading to poor activity of compound (**25**).

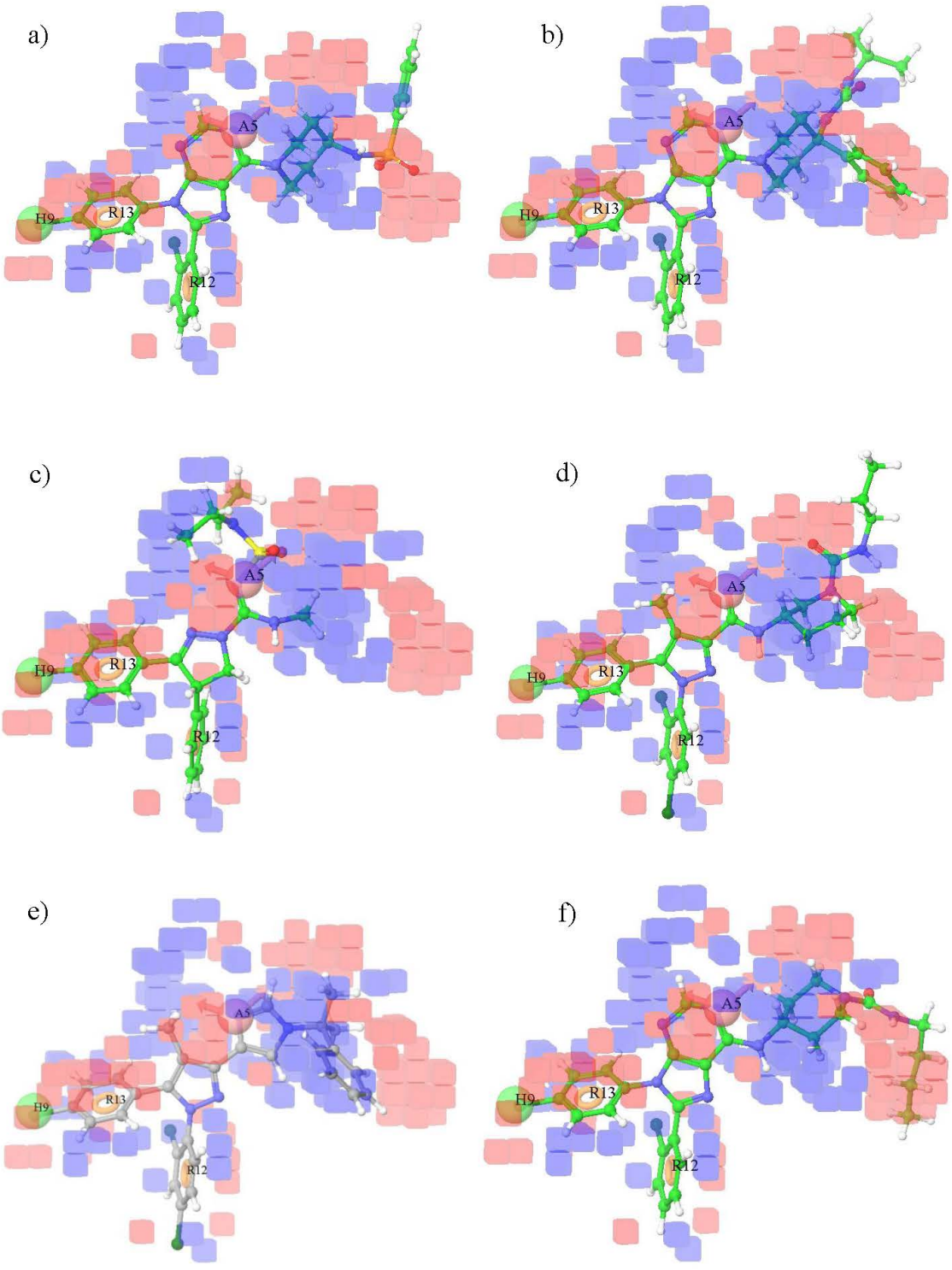

Fig. 4.2.9 Effect of hydrophobic groups on a) active compound (**24**), b) inactive compound (**23**), c) active compound (**3**), d) inactive compound (**21**), e) active compound (**9**) and f) inactive compound (**25**).

4.3 Performing virtual screening for the identification of novel scaffolds by using different filters like pharmacophore model, 3D-QSAR (atom-based), molecular docking, Lipinski's rule of five, CNS score and receptor-ligand interactions.

Virtual screening is a useful technique for the identification of hits using databases available in public/private domain. The main aim of the current study was to infuse and introduce newer chemical diversity to CB1 receptor antagonists in terms of entirely different scaffolds than the existing ones. The information derived from pharmacophore and 3D-QSAR modelling has been utilised for the identification of promising hits as peripherally acting CB1 receptor antagonists to broaden the chemical landscape of the currently existing narrow chemical spectrum of peripherally restricted CB1 receptor antagonists so that newer CB1 receptor antagonists could be discovered having lesser side effects and better therapeutic efficacy for the control of obesity. The present study is a step towards the designing of newer unknown chemical classes of peripherally acting CB1 receptor antagonists. Here, both the ligand and the structure based drug design approaches are combined together to mine more reliable information which could be successfully applied to develop novel peripherally acting CB1 receptor antagonists. Different filters were applied (Fig. 4.3.1) to get the initial hits as CB1 receptor antagonists to the Asinex database containing 435,214 compounds.

4.3.1 First Filter: Pharmacophore features

The best validated pharmacophore hypothesis AHRR.6 generated in this study was used as the first filter to search Asinex database. A condition that all the four features (2 aromatic rings, 1 hydrophobic group, 1 hydrogen bond acceptor) of the pharmacophore hypothesis must match to the compounds was applied. A total of 139,686 compounds matched the pharmacophore features present in AHRR.6. Fitness score (fixed at ≥ 1.5) is an important parameter which measures how well the ligand fits the pharmacophore. On the basis of fitness score, 49,780 compounds were obtained at this stage (Fig. 4.3.1).

4.3.2 Second Filter: Molecular docking

Molecular docking was applied as the second filter. As, the crystal structure of CB1 receptor remains elusive upto 2016, therefore a homology modeled structure[264] was used for the docking studies. Some reference compounds such as rimonabant,

AM6545 and TM38837 were also grafted in the dataset. In the docking studies, a high-throughput virtual screening (HTVS) method was used first to dock the compounds. The reference compound rimonabant showed a G-score (-7.605) which was fixed as the threshold value for the screening. A total of 3,155 compounds showed G-score greater than the threshold value (-7.605) and all these compounds were selected as hits. These 3,155 hits were docked again in the active site of CB1 receptor by standard precision (SP) method using the same reference compounds. At this stage, the reference compound AM6545 showed a G-score (-9.121). Out of the 3,155 compounds, 262 compounds showed higher G-scores than the scores of the reference compounds. These 262 compounds were further re-docked in the active site of CB1 receptor by extra-precision (XP) method. The reference compound AM6545 showed a G-score (-10.047) which was fixed as the new threshold value. Only 86 compounds showed higher G-score than the threshold value (-10.047) in this phase of filtering process.

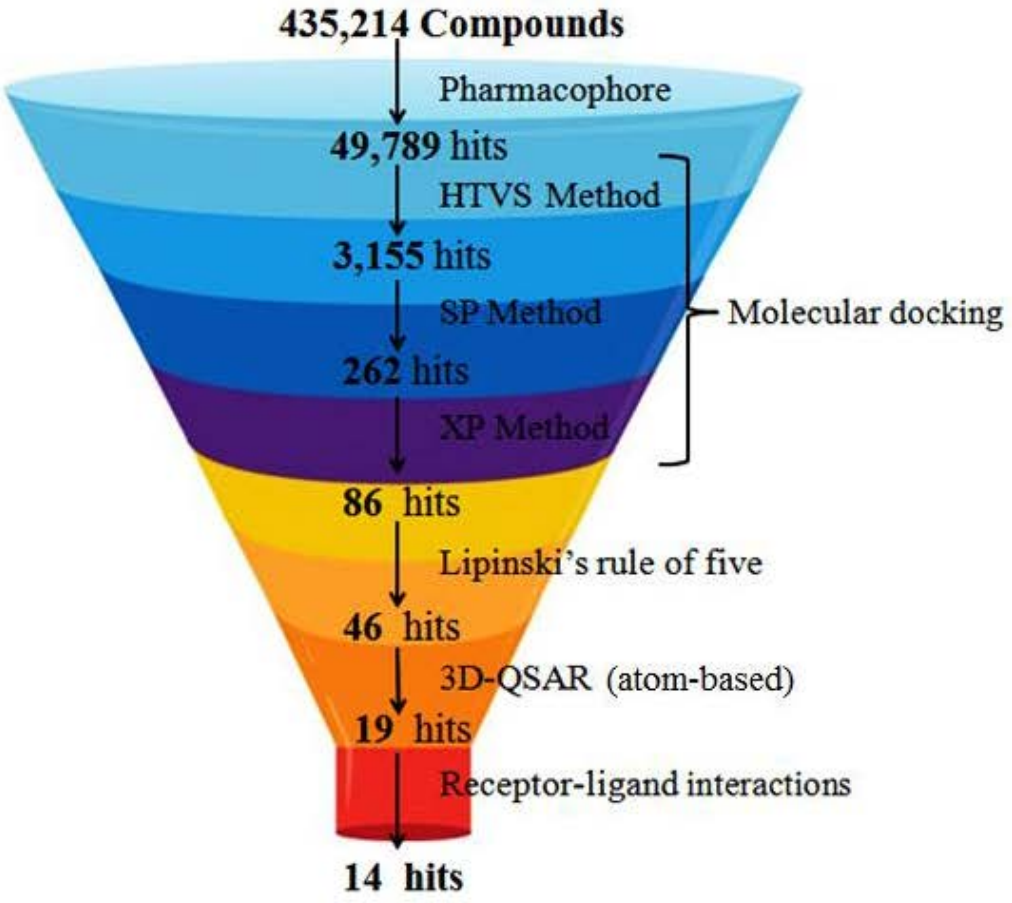

Fig. 4.3.1 Flow chart of virtual screening of compounds applied on Asinex database of 435,214 compounds.

4.3.3 Third Filter: Lipinski's rule of five

To evaluate the hits for drug like properties the third filter of 'Lipinski's rule of five' was applied. Only 46 compounds followed Lipinski's rule of five. The molecular weight of the selected leads ranged from 377.51 to 494.52, lipophilicity in between 1.87 to 4.99, H-bond donor groups ranged from 0 to 2 and H-bond acceptors were from 4 to 9 indicating that all the 46 selected compounds followed the rules of five.

4.3.4 Fourth filter: Application of 3D-QSAR (atom-based) model to predict the activity

CB1 receptor antagonistic activity of the 46 hits obtained from the previous stage was predicted by using the developed 3D-QSAR (atom-based) model. A predicted activity value of 7.5 was considered as the threshold value for the active compounds (similar to that maintained in the development of pharmacophore model). At this stage, a total of 19 hits having predicted activity higher than the threshold value (7.5) were obtained.

4.3.5 Fifth Filter: CNS score and receptor interactions

CNS score ranging from +2 to -2 indicates the probable presence or absence of a drug in the brain.[256] CNS score of +2 indicates strong presence of the drug in the brain whereas CNS score of -2 indicates its absence. This scoring was applied for the identification of peripherally active compounds as restricted entry into the CNS was an essential requirement for the designing of peripherally active CB1 receptor antagonists. CNS score was calculated for the 19 hits obtained from the previous stage of filtration. Only 14 compounds showed CNS score of -1 or -2. These 14 hits in which all the four pharmacophore features were present and the compounds also fulfilled other essential requirements to exhibit potent and selective peripherally acting CB1 receptor antagonist activity were selected finally. Chemical structures of the obtained 14 hits are shown in Fig. 4.3.2.

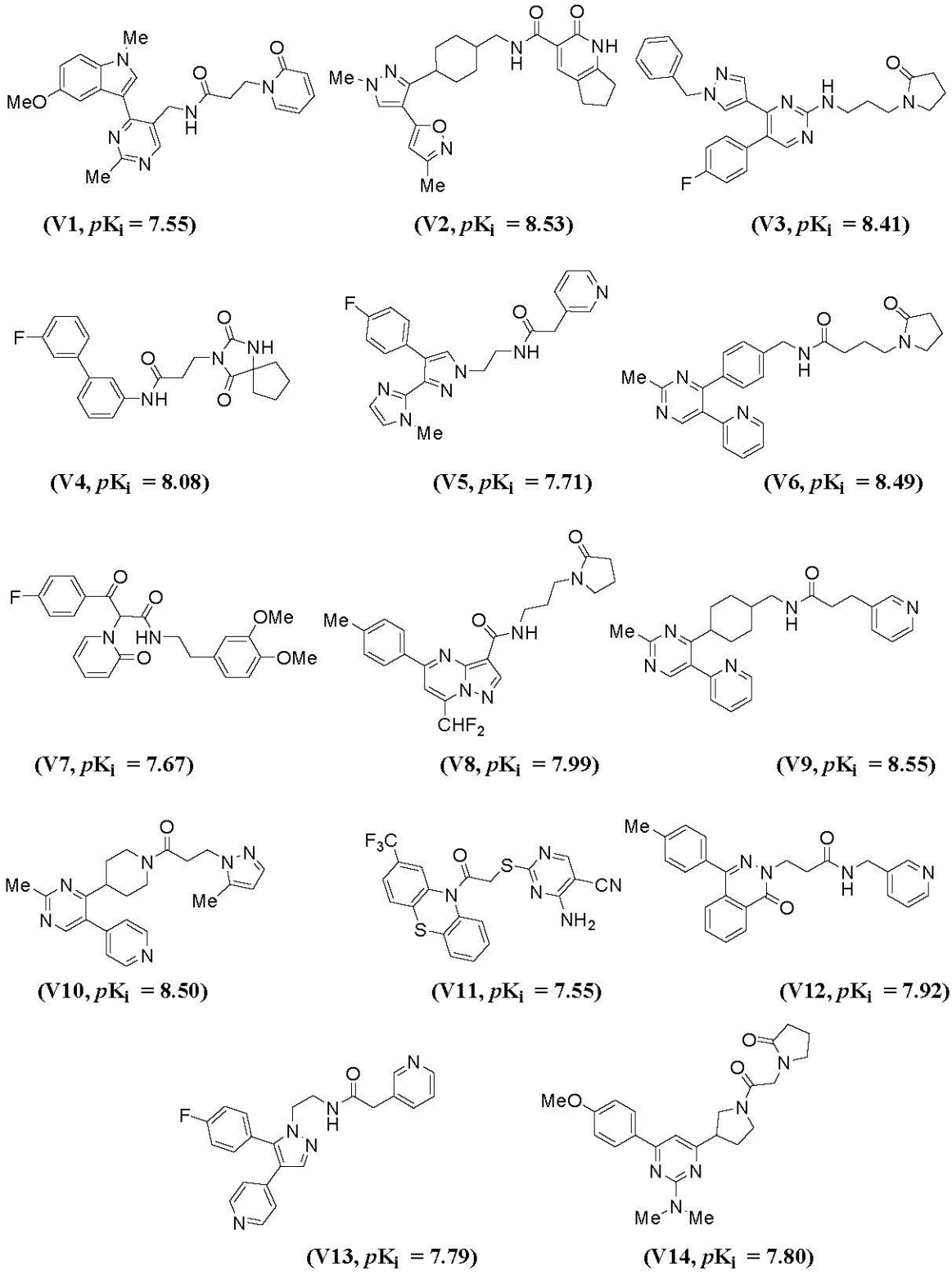

(V1, pK_i = 7.55) **(V2, pK_i = 8.53)** **(V3, pK_i = 8.41)**

(V4, pK_i = 8.08) **(V5, pK_i = 7.71)** **(V6, pK_i = 8.49)**

(V7, pK_i = 7.67) **(V8, pK_i = 7.99)** **(V9, pK_i = 8.55)**

(V10, pK_i = 8.50) **(V11, pK_i = 7.55)** **(V12, pK_i = 7.92)**

(V13, pK_i = 7.79) **(V14, pK_i = 7.80)**

Fig. 4.3.2 Chemical structures and predicted activities (calculated by using the developed 3D-QSAR model) of 14 hits obtained through virtual screening.

It was observed from the rimonabant-CB1 receptor interaction study that the carbonyl group of rimonabant formed H-bond with Lys192, 4-chlorophenyl ring was oriented towards Val196, Phe200, Trp356 and Leu360, 2,4-dichlorophenyl ring was oriented towards Trp279 and Met363, and piperidyl group interacted with Phe177, Phe189 and Trp255 residues. The identified 14 hits are having diverse scaffolds such as pyrazole, pyridine, pyrimidine, indole, phenothiazine, pyrazolo[1,5-*a*]pyrimidine etc. It was observed that all of the obtained hits showed good binding interactions in the active site of CB1 receptor. H-bonds were formed by these hits with Asp266, Ile267, Phen268, Ser383 and Lys192 as shown in Fig. 4.3.3. H-bond formation with Lys192 is essential for the CB1 receptor antagonistic activity as observed in rimonabant (Fig. 4.3.3a). Peripherally acting compound AM6545 also formed H-bond with Lys192 as shown in Fig. 4.3.3b. The pyrimidine ring of compound **V1** is oriented towards Val196, Phe200 and Trp356 residues, phenyl ring of the indole moiety is oriented towards Trp279 and Met363 whereas the pyridone ring is oriented towards Phe177, His178, Asp266, Ile267, Lys376 and Phe379 residues. In case of compound **V2**, the oxazole ring is oriented towards Trp356 and Phe200, pyrazole ring is oriented towards Phe278 and Trp279 residues whereas the pyridone ring showed interactions with Phe177, Asp266, Phe279, Ala380 and His178. Thus, it is revealed from this study that the obtained hits are suitably oriented in the active site of CB1 receptors. The orientations of compounds (**V1** and **V2**) are shown in Fig. 4.3.3 (c and d) respectively.

All the hits fulfilled the physicochemical requirements for a 'drug like compound' and were lying within the acceptable range of all the desirable parameters (Table 4.3.1). One important strategy for the designing of peripheral acting CB1 receptor antagonists is to increase the polar surface area and decrease the lipophilicity so that the designed compounds do not enter the CNS. Polar surface area of these hits was ranging from 76.71 to 111.71, which was much higher than rimonabant (PSA = 53.32). Lipophilicity (i.e. logP) of these hits was ranging from 2.24 to 4.62, much lower than that of rimonabant (logP = 6.11) indicating that the obtained hits were having favourable hydrophobicity for showing peripheral CB1 receptor antagonist activity.

Virtual screening offered highly diverse set of hit molecules. Some of these scaffolds (V1, V4, V7, V8, V11, V12 and V14) have never been reported to be present in CB1 receptor antagonists. This feature fulfilled one of the envisaged aim of performing virtual screening i.e. diversifying the existing chemical landscape of peripherally restricted CB1 receptor antagonists.

Table 4.3.1 Computed physicochemical properties of the obtained 14 hits.

Compd	Mol. Wt	No. of HBD	No. of HBA	logP	CNS score	PSA	No. of rotatable bonds	HB	% Absorption in human
V1	431.49	1	7	3.43	-2	101.35	6	4	94.03
V2	435.52	2	6	4.62	-2	111.71	3	4	100.00
V3	470.54	1	7	4.36	-2	80.93	9	2	100.00
V4	395.43	2	5	4.04	-2	103.60	5	3	100.00
V5	404.44	1	7	3.85	-1	76.92	5	3	100.00
V6	429.52	1	6	2.88	-2	97.01	9	4	87.69
V7	438.45	1	7	3.79	-1	93.68	9	2	100.00
V8	427.45	1	7	3.69	-1	96.06	6	3	94.58
V9	415.53	1	5	4.17	-1	76.71	6	4	100.00
V10	390.48	0	7	2.96	-1	80.09	4	3	92.12
V11	459.46	2	7	3.77	-2	100.37	5	1	89.93
V12	398.46	1	5	3.99	-1	82.83	6	1	100.00
V13	401.44	1	6	3.77	-1	77.83	5	3	96.34
V14	423.51	0	8	2.24	-1	83.83	5	2	90.66
Rimonabant	463.79	1	5	6.11	+2	53.32	2	1	100.00

HBD: Hydrogen bond donor, HBA: Hydrogen bond acceptor, HB: No. of Hydrogen bonds formed with the receptor

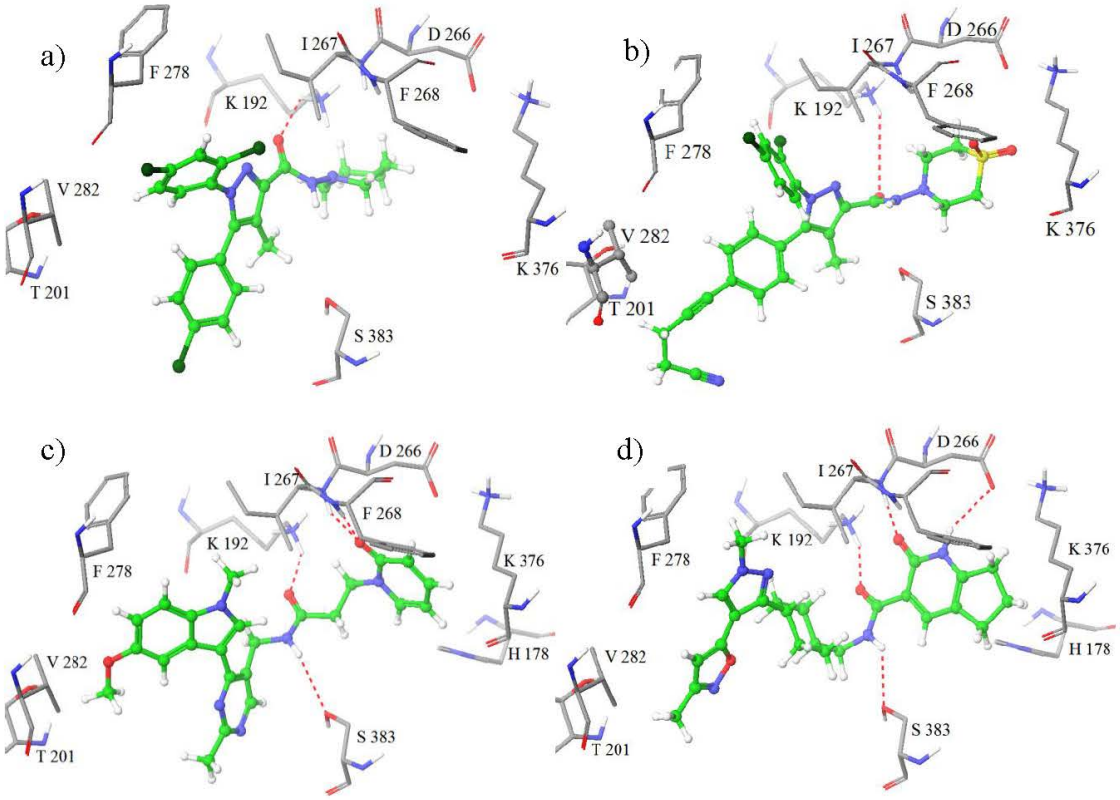

Fig. 4.3.3 Docking interactions of (a) Rimonabant (b) AM6545 (c) hit (**V1**) (d) hit (**V2**) with CB1 receptor.

4.4 Hit optimization through molecular modeling techniques and synthesis of the designed compounds

4.4.1 Identification of hit (V11) as anti-obesity agent

All the computational studies reported in the present work were carried out using Maestro (9.0 and 9.4) software of Schrödinger, USA.[260,265] The developed pharmacophore and 3D-QSAR (atom-based) models were used in this study for determining the fitting of the designed compounds into the pharmacophoric features, and prediction of the biological activity. For molecular modeling purposes, chemical structures of all the compounds were sketched, cleaned up and the structures were minimized by using OPLS 2005 force field in the standard tool 'Ligprep' of Maestro 9.0. Molecular docking studies for the designed compounds were performed by using standard tool 'Glide 5.5' in Maestro 9.0 software.[266] The co-crystallized structure for CB1 receptor (PDB code: 5TGZ) was downloaded from RCSB Protein Data Bank.[267] Protein preparation was done by addition of all the hydrogen atoms and deletion of water molecules. The hydrogen bond assignment was optimized by exhaustive sampling method and the obtained protein structure was energy minimized in presence of OPLS_2005 force field using Impref module in the standard option 'protein preparation wizard' of Maestro 9.0. The obtained protein structure was used for receptor grid generation.[268] The energy minimized structures were docked into the active site of CB1 receptor by using extra-precision (XP) mode. Docking protocol was validated by re-docking the co-crystallized ligand and by observing the interactions with the active site of the CB1 receptor. Physicochemical and pharmacokinetic parameters were calculated by using Qikprop module of Maestro 9.0[256] and pkCSM pharmacokinetic software.[269]

In the current era of drug discovery process, computational methods play a vital role in the identification of novel hits which could be further processed to convert them into clinically used therapeutic agents. In the search of newer scaffolds for CB1 receptor antagonists, we successfully found new hits with the application of virtual screening of Asinex database containing 4,35,214 compounds using different filters and tools such as pharmacophore mapping, 3D-QSAR model, Lipinski's rule of five, CNS scoring, molecular docking and receptor ligand interactions. Out of the 4,35,214 compounds, finally 14 compounds were obtained as novel hits. Out of these 14 hits, seven hits (V1, V4, V7, V8, V11, V12 and V14) were found having totally new

scaffolds which were never reported in CB1 receptor antagonists. Out of these 7 hits, all were found to be having quite similar diaryl containing scaffold except for hit V11, which contained a phenothiazine scaffold which was never reported in the literature to show CB1 receptor antagonist activity.

Pharmacophore modeling studies were performed on the hit (V11) using our own developed pharmacophore model (AHRR.6) for peripherally acting CB1R antagonists. In the four featured pharmacophore (AHRR.6) model, the two phenyl rings of phenothiazine scaffold of the hit (V11) occupied the aromatic ring (R12 and R13) features. Hydrophobic (H9) feature was occupied by the trifluoromethyl group attached to 2nd position of the phenothiazine ring. The feature of hydrogen bond acceptor (A5) was occupied by the nitrogen of the pyrimidine ring indicating that the hit (V11) fitted suitably into the pharmacophore as shown in Fig. 4.4.1b. The *in silico* activity of the obtained hit (V11) was predicted by using the best developed 3D-QSAR (atom-based) model and it was predicted a pK_i value of 7.55 where the threshold value of the active compounds was set to be $pK_i \geq 7.5$ indicating that the hit (V11) could be an active compound. Orientation of the hit (V11) in the active site of CB1 receptor was also studied and found to be quite similar to rimonabant (Fig. 4.4.1c). Trifluoromethyl group attached to the 2nd position of the phenothiazine ring of the hit (V11) was oriented towards Val196, Phe200, Trp356 and Leu360 residues similar to the 4-chlorophenyl group of rimonabant. Ring A of phenothiazine of hit (V11) was oriented towards Trp279 and Met363 residues similar to 2,4-dichlorophenyl ring of rimonabant (Fig. 4.4.1a). Pyrimidine ring of hit (V11) was oriented towards Phe177, Phe189 and Trp255 residues similar to piperidyl group of rimonabant. The hit (V11) showed one hydrogen bond between the nitrogen of pyrimidine ring and Lys192, which was essential for the CB1 receptor antagonistic activity. Thus, the docking studies indicated that the hit (V11) was bound in the active site of CB1 receptor similar to rimonabant as shown in Fig. 4.4.1c. The results of the pharmacophore mapping, 3D-QSAR and docking studies clearly indicated that hit (V11) was a suitable case for further optimization. Biological evaluation of the hit (V11) (compound **1**, Fig. 4.5.1) as orally active anti-obesity agent supported the theoretical studies. So, it was planned to synthesize and optimize the novel phenothiazine series as peripherally acting CB1 receptor antagonist for the treatment of obesity.

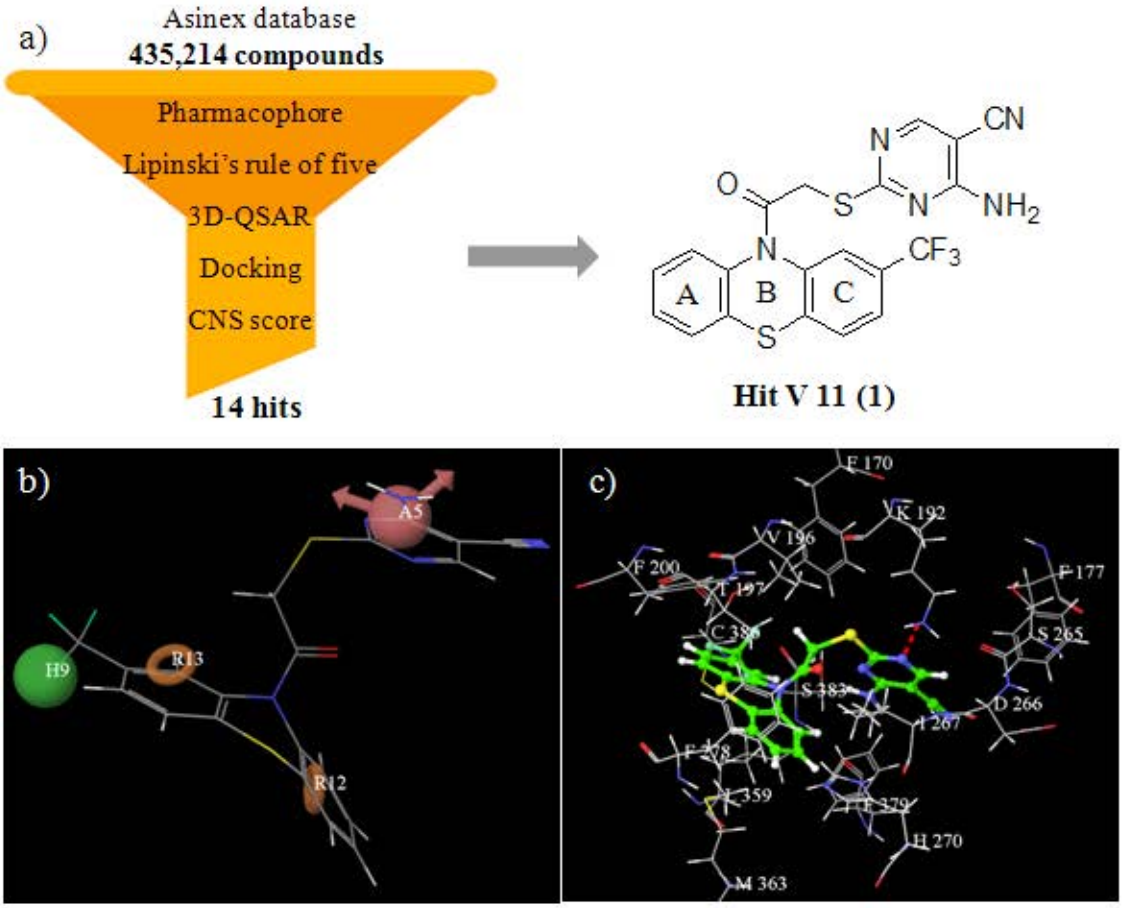

Fig. 4.4.1 a) Flowchart of virtual screening and chemical structure of hit V11 (**1**), b) fitting of hit V11 (**1**) in the pharmacophore model, c) orientation of hit V11 (**1**) in the active site of CB1 receptor.

4.4.2 Optimization of the hit V11 (1)

Further, with the aim to enhance potency, modifications were carried out in the structure of the hit (V11) and the resulting compounds were assessed through molecular modeling techniques. As per the pharmacophore (AHRR) model, two phenyl rings of the phenothiazine scaffold were perfectly aligned on the pharmacophoric ring features (R12 and R13) hence the rings were not modified and the phenothiazine scaffold was maintained as such in the designed molecules. Modifications were carried out on two places i.e. on the sites having hydrophobic group and hydrogen bond acceptor group. The hydrophobic (H) feature of the developed pharmacophore was occupied by the trifluoromethyl group of hit (V11). So, different hydrophobic groups were planned to be incorporated, such as trifluoromethyl, chloro and methoxy at this position which could favour high potency, and the activity of the resulting compounds was predicted. Keeping hydrogen at this position decreased the activity as is the case with compound (**20**) because it has only three pharmacophoric features (ARR). With the objective to

establish the structure activity relationship, it was planned to synthesize these compounds. In the region of hydrogen bond acceptor (A) pharmacophore feature, it was decided to put some polar functional groups so that this group could occupy hydrogen bond acceptor feature and would show mandatory interactions with Lys192 residue, a key amino acid residue for CB1 activity. Thus, considering the synthetic feasibility, efforts were made to attach different polar functional groups such as 4,5-dihydrothiazole, 1-phenyl-1*H*-tetrazole, 1,3,4-thiadiazol-2-amine, 4-(1,3,4-oxadiazol-2-yl)pyridine, 4-amino-5-(4-pyridyl)-4*H*-1,2,4-triazole and ethyl 4-aminopyrimidine-5-carboxylate. The 4,5-dihydrothiazole substituted compound showed low PSA and G-score values of 33.15 $Å^2$ and -8.58 respectively. In 1-phenyl-1*H*-tetrazole substituted compound, the PSA increased to 69.66 $Å^2$ but the G-score got reduced (-7.44). The 1,3,4-thiadiazol-2-amino substituted compound showed comparatively better PSA and G-score values i.e. 74.10 $Å^2$ and -8.85 respectively. 4-(1,3,4-Oxadiazol-2-yl)pyridine substituted compounds showed still improved PSA value of 76.81 $Å^2$ and G-score of -10.79. Substitution with 4-amino-5-(4-pyridyl)-4*H*-1,2,4-triazole group further increased the PSA value to 96.27 $Å^2$ and G-score to -11.74. Ethyl 4-aminopyrimidine-5-carboxylate substituted compound showed the highest PSA value of 106.26 $Å^2$ with a good G-score of -10.37. Higher values of PSA and G-score suggested that the substituted pyrimidine, oxadiazole and triazole groups could be favourable for peripheral CB1R antagonist activity. Furthermore, good fitness scores and improved predictive activities prompted us to take up these compounds for synthesis.

Further, efforts were also made to vary the carbon chain spacer between 2-chloro substituted phenothiazine scaffold and 4-amino-2-mercaptopyrimidine-5-carbonitrile group. The 2 carbon chain bearing compounds showed poor results (fitness score = 1.09, *p*Ki = 6.90, G score = -9.17) as compared to the compounds with 3 carbon spacer (fitness score = 1.15, *p*Ki = 8.20, G score = -10.17). So, it was decided to synthesize some compounds with spacer having 3 carbon chain. The fitness score, predicted activity (pK_i) and G-score of the designed compounds are shown in Table 4.4.1. Synthesis of the designed phenothiazine compounds were carried out as per the scheme 1 and 2.

Table 4.4.1 Fitness score, predicted activity and G-score of the synthesized compounds

Comp	Fitness Score (Pharmacophore)	Predicted Activity (pK_i) (3D-QSAR model)	G-score (Docking)
1	1.55	7.55	-10.58
18	1.48	7.59	-10.05
19	1.63	7.66	-10.04
20	1.76	7.04	-10.21
21	1.53	7.99	-10.37
22	1.77	7.52	-9.46
23	1.60	8.00	-10.33
24	1.72	6.99	-10.35
25	1.67	7.16	-10.79
26	1.69	7.31	-9.48
27	1.67	7.47	-9.10
28	1.14	7.51	-9.99
29	1.45	7.60	-11.74
30	1.46	7.75	-9.80
31	1.44	7.17	-10.70
32	0.95	7.10	-9.49
38	1.64	7.55	-12.59
39	1.15	8.20	-10.17
40	1.76	8.15	-10.34
41	1.64	7.12	-10.24
42	1.63	8.15	-11.20
43	1.55	7.79	-8.70
44	1.42	7.11	-9.22
45	1.63	7.29	-9.57
Rimonabant	2.53	7.90	-9.01

Thus, the selected hit (V11) was modified using different hydrophobic and polar functional groups. The compounds planned for the synthesis contained groups such as trifluoromethyl, chloro, methoxy and hydrogen, at 2nd position of the phenothiazine ring and certain polar functional groups such as substituted pyrimidine, oxadiazole and triazole attached to the amide chain. Some compounds having three carbon chain in between phenothiazine and pyrimidine ring were also planned to be synthesized. All the designed compounds were evaluated by the pharmacophore model, 3D-QSAR model and docking studies prior to synthesis as shown in Table 4.4.1.

The physicochemical and pharmacokinetic parameters of the designed compounds were also computed. The physicochemical properties such as molecular weight (391.46 - 506.56), number of hydrogen bond donors (0 - 2), number of hydrogen bond acceptors (6 - 9), hydrophobicity (2.77 - 6.31), polar surface area (75.22 - 114.55) and number of rotatable bonds (3 - 9) were in the acceptable range. All the

designed compounds were predicted to show good human absorption (71.62 - 100 %). BBB (im)permeability, an important parameter for the designing of peripherally acting CB1 antagonists, was computed for the designed compounds. The threshold value for the compounds that indicated readily crossing of the BBB was logBB > 0.3 whereas logBB < -1 indicated poor penetration into the brain.[270,271] The values of BBB permeability of the designed compounds were in the range -0.52 to -1.72, whereas rimonabant showed BBB permeability value of 0.23. This data clearly indicated that the designed compounds would not cross the BBB. It was also predicted that all the compounds would be metabolised by CYP3A4 enzyme system. The total clearance of the synthesized compounds ranged from 0.009–0.351 ml/min/kg indicating good physicochemical and pharmacokinetic properties (Table 4.4.2) suggesting their 'drug like' behaviour.

Table 4.4.2 Computed physicochemical and pharmacokinetic properties of the synthesized compounds.

Comp	Mol. Wt	No. of HBD	No. of HBA	log P	PSA	No. of rotatable bonds	% Absorption (human)	BBB permeability (logBB)	Metabolism by	Total clearance log(ml/min/kg)
1	459.46	2	7	3.77	100.37	5	89.93	-1.30	CYP3A4	0.158
18	425.91	2	7	3.59	99.42	5	88.59	-1.02	CYP3A4	0.079
19	421.49	2	8	3.20	107.71	6	86.29	-0.97	CYP3A4	0.313
20	391.46	2	7	2.95	97.59	5	86.93	-0.84	CYP3A4	0.138
21	506.51	2	8	5.33	106.26	6	78.15	-1.54	CYP3A4	0.195
22	472.96	2	8	4.83	106.27	6	100.00	-1.26	CYP3A4	0.117
23	468.54	2	8	4.42	114.55	7	100.00	-1.31	CYP3A4	0.351
24	438.51	2	8	4.42	104.43	6	100.00	-1.08	CYP3A4	0.176
25	486.48	0	7	4.68	76.81	3	100.00	-1.57	CYP3A4	0.150
26	452.93	0	8	4.17	76.82	3	100.00	-0.89	CYP3A4	0.067
27	448.51	0	8	3.72	85.10	4	100.00	-1.32	CYP3A4	0.302
28	418.48	0	7	3.66	76.83	3	100.00	-1.10	CYP3A4	0.133
29	500.51	2	8	3.73	96.27	4	71.62	-1.72	CYP3A4	0.032
30	466.96	2	8	3.25	96.28	4	81.62	-1.44	CYP3A4	0.046
31	462.54	2	9	2.85	104.57	5	79.30	-1.09	CYP3A4	0.174
32	432.51	2	8	2.77	96.29	4	78.80	-0.87	CYP3A4	0.009
38	459.50	2	6	5.04	75.23	7	91.35	-0.95	CYP3A4	0.151
39	425.93	2	6	4.33	75.33	7	100.00	-0.68	CYP3A4	0.094
40	421.53	2	7	4.17	81.92	8	100.00	-0.74	CYP3A4	0.319
41	391.50	2	6	4.07	75.22	7	100.00	-0.52	CYP3A4	0.153
42	506.56	2	7	6.31	81.73	8	89.36	-1.25	CYP3A4	0.160
43	473.00	2	7	5.82	81.73	8	100.00	-0.98	CYP3A4	0.103
44	468.58	2	8	5.47	87.55	9	100.00	-1.04	CYP3A4	0.328
45	438.56	2	7	5.34	80.52	8	95.59	-0.81	CYP3A4	0.162
Rimonabant	463.79	1	5	6.11	53.32	2	100.00	0.23	CYP3A4	0.156

4.4.3 Chemistry

The designed compounds were synthesized as per the synthetic scheme shown in Fig. 4.4.2 and 4.4.3. In the synthetic scheme (Fig. 4.4.2), ethoxymethylenemalononitrile and ethyl 2-cyano-3-ethoxyacrylate (**2** and **3**) were treated with thiourea (**4**) in the presence of sodium ethoxide as base at room temperature to obtain 5-substituted 4-amino-2-mercaptopyrimidine derivatives (**5** and **6**) respectively. Further, 2-substituted phenothiazine derivatives (**7-10**) were treated with chloroacetyl chloride (**11**) using triethylamine to yield the 2-substituted 2-chloro-1-(10*H*-phenothiazin-10-yl)ethanone derivatives (**12-15**) which were further treated with the thiol derivatives (**5**, **6**, **16**, **17**) using potassium carbonate and dimethylformamide (DMF) to obtain the final compounds (**1**, **18-32**).

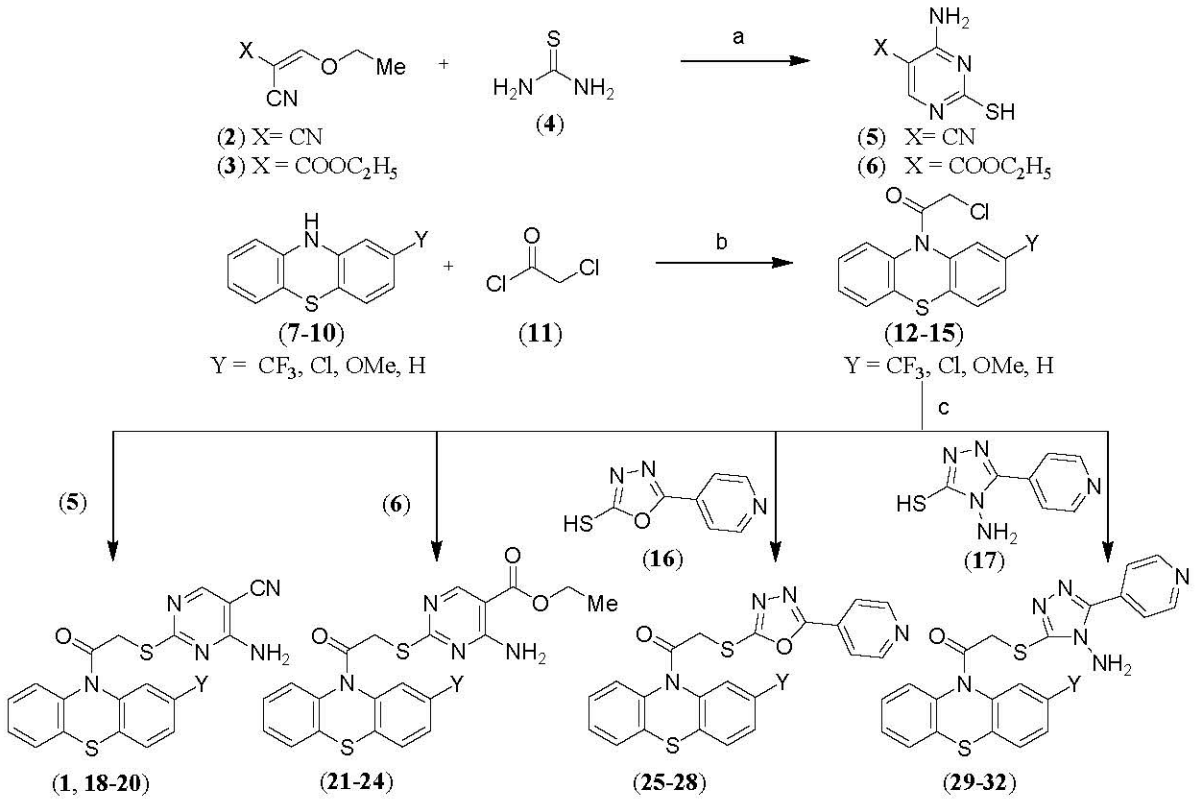

Comp	Y
7, 12, 1, 21, 25, 29	CF_3
8, 13, 18, 22, 26, 30	Cl
9, 14, 19, 23, 27, 31	OMe
10, 15, 20, 24, 28, 32	H

Fig. 4.4.2 Reagents and conditions: a) $NaOC_2H_5$, EtOH, rt; b) triethylamine, DCM, reflux; c) K_2CO_3, DMF, rt.

In the synthetic scheme (Fig. 4.4.3), 2-substituted phenothiazine derivatives (**7-10**) were treated with 1-bromo-3-chloropropane (**33**) using sodium hydride with DMSO and THF to form 2-substituted 10-(3-chloropropyl)-10*H*-phenothiazine derivatives (**34-37**), which were further reacted with the thiol derivatives (**5**, **6**) to form the desired compounds (**38-45**).

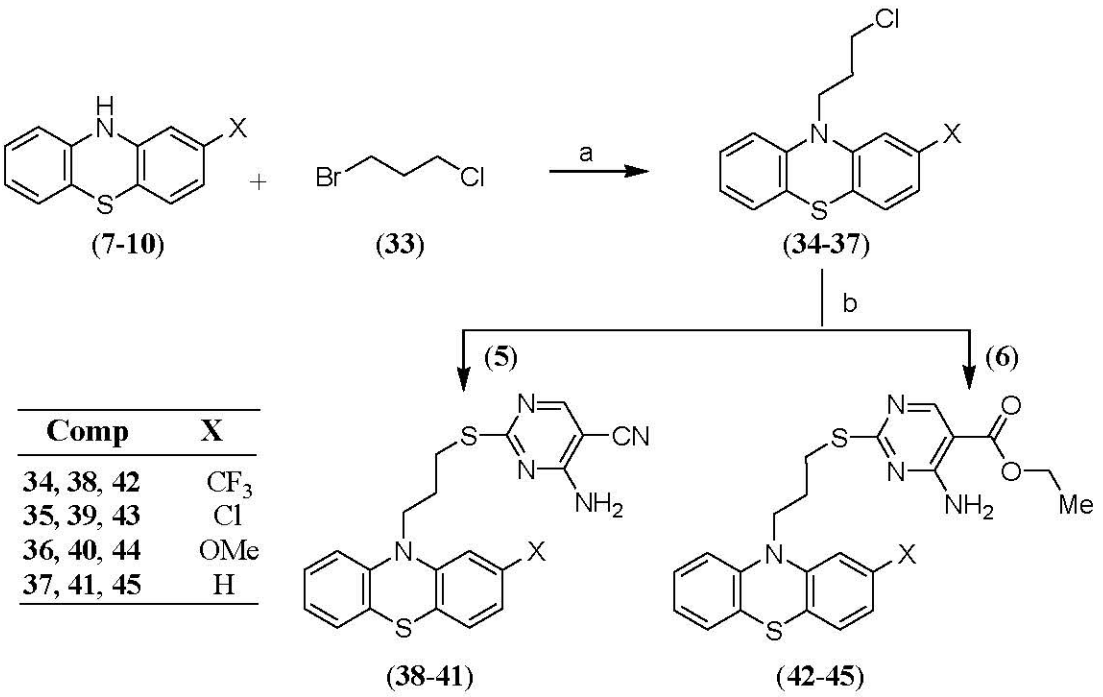

Comp	X
34, 38, 42	CF_3
35, 39, 43	Cl
36, 40, 44	OMe
37, 41, 45	H

Fig. 4.4.3 Reagents and conditions: a) NaH, DMSO, THF, 0 ^{0}C; b) K_2CO_3, DMF, rt.

In order to execute schemes 1 and 2, commercially available ethoxymethylenemalononitrile (**2**), ethyl 2-cyano-3-ethoxyacrylate (**3**), 2-substituted phenothiazine derivatives (**7-10**), chloroacetyl chloride (**11**), 1-bromo-3-chloropropane (**33**) were used as such. The work related to the synthesis of intermediates and the designed targeted compounds has been described under the following major heads:

4.4.3.1 Synthesis of 5-substituted 4-amino-2-mercaptopyrimidine derivatives (**5** and **6**)

4.4.3.2 Synthesis of 2-substituted 2-chloro-1-(10*H*-phenothiazin-10-yl)ethanone derivatives (**12-15**)

4.4.3.3 Synthesis of 1-(2-substituted-10*H*-phenothiazin-10-yl)-2-substituted-2-ylthio)ethanones (**1**, **18-32**)

4.4.3.4 Synthesis of 10-(3-chloropropyl)-10*H*-phenothiazine derivatives (**34-37**)

4.4.3.5 Synthesis of 5-substituted 2-(3-(2-substituted-10*H*-phenothiazin-10-yl)propylthio)-4-aminopyrimidine compounds (**38-45**)

4.4.3.1 Synthesis of 5-substituted 4-amino-2-mercaptopyrimidine derivatives (5 and 6)

In Scheme 1, ethoxymethylenemalononitrile (**2**) or ethyl 2-cyano-3-ethoxyacrylate (**3**) were reacted with thiourea (**4**) to obtain 4-amino-2-mercaptopyrimidine-5-carbonitrile (**5**) and ethyl 4-amino-2-mercaptopyrimidine-5-carboxylate (**6**) respectively in the presence of sodium ethoxide as a base at room temperature. IR spectrum of compound (**5**) showed N-H stretching vibrations as two strong peaks at 3443 and 3370 cm^{-1} and C≡N stretching of cyano group was seen at 2223 cm^{-1}. Mass spectrum of compound (**5**) showed a peak at 153.1 $(M+1)^+$. IR spectrum of compound (**6**) showed N-H stretching vibrations as two strong peaks at 3551 and 3387 cm^{-1} and C=O stretching of ester group was seen at 1705 cm^{-1}. Mass spectrum of compound (**6**) showed a peak at 199.7 $(M+1)^+$.

4.4.3.2 Synthesis of 2-substituted 2-chloro-1-(10*H*-phenothiazin-10-yl)ethanone derivatives (12-15)

2-Substituted phenothiazines (**7-10**) were reacted with chloroacetyl chloride using triethylamine as base to obtain 2-substituted 2-chloro-1-(10*H*-phenothiazin-10-yl)ethanone derivatives (**12-15**). IR spectra of compounds (**12-15**) showed C=O stretching of the amide group at 1690, 1682, 1689 and 1693 cm^{-1} respectively.

(**12**) X = CF_3; (**13**) X = Cl
(**14**) X = OMe; (**15**) X = H

4.4.3.3 Synthesis of 1-(2-substituted-10*H*-phenothiazin-10-yl)-2-substituted-2-ylthio)ethanones (1, 18-32)

Substituted 2-chloro-1-(10*H*-phenothiazin-10-yl)ethanones (**12-15**) were reacted with thiol containing compounds (**5**, **6**, **16** and **17**) using anhydrous potassium carbonate as base at room temperature to obtain 1-(2-substituted-10*H*-phenothiazin-10-yl)-2-substituted-2-ylthio)ethanones (**1**, **18-32**).

IR spectrum of compound (**1**) showed N-H stretching vibrations as two strong peaks at 3402 and 3321 cm^{-1}, C≡N stretching of cyano group was seen at 2216 cm^{-1} and C=O stretching of amide group was seen at 1684 cm^{-1}. The PMR spectrum of compound (**1**) showed singlet at δ 8.25 ($1H_i$), singlet at δ 7.64 ($1H_a$), doublet at δ 7.54-7.52 ($1H_b$, J = 7.8), doublet at δ 7.50-7.48 ($1H_c$, J = 7.8), multiplet at δ 7.40-7.36 ($2H_{g,f}$), multiplet at δ 7.32-7.28 ($1H_e$) and doublet at δ 7.26-7.23 ($1H_d$) for aromatic protons. A broad singlet was observed at δ 5.70 ($2H_j$) due to the protons of amine. The aliphatic protons showed a singlet at δ 4.03 ($2H_h$). Its ^{13}C-NMR spectrum showed peak at δ 172.88 due to C=O carbon of the amide. Aromatic carbons appeared at 166.55, 161.22, 159.46, 138.12, 137.13, 131.35, 128.0, 127.79, 127.42, 127.19, 126.85, 124.67, 123.96, 123.0, 121.97 and 114.91 whereas the aliphatic carbon appeared at δ 85.94 and 34.02. Its mass spectrum showed molecular ion peak at 460.2 $(M+1)^+$.

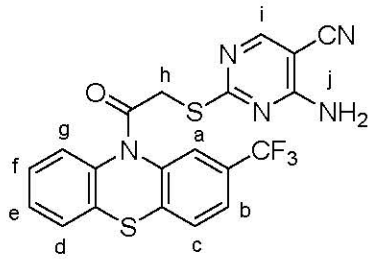

(**1**)

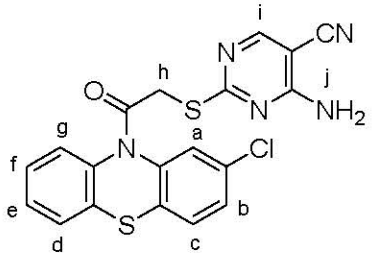

(**18**)

IR spectrum of compound (**18**) showed N-H stretching vibrations as two strong peaks at 3460 and 3332 cm^{-1}, C≡N stretching of cyano group was seen at 2224 cm^{-1} and C=O stretching of amide group was seen at 1645 cm^{-1}. The PMR spectrum of compound (**18**) showed signals at δ 8.24 (s, 1H, Ar-H_i), 7.91 (s, 1H, Ar-H_a), 7.58-7.54 (m, 2H, Ar-$H_{b,c}$), 7.51-7.49 (d, 2H, Ar-$H_{g,d}$), 7.43-7.39 (m, 1H, Ar-H_f), 7.35-7.31 (m, 1H, Ar-H_e), 5.74 (bs, 2H, NH_{2j}) and 4.05 (dd, 2H, CH_{2h}) for two protons. Its mass spectrum showed molecular ion peak at 426 $(M+1)^+$ and 428 $(M+3)^+$.

IR spectrum of compound (**19**) showed N-H stretching vibrations as two strong peaks at 3337 and 3179 cm^{-1}, C≡N stretching of cyano group was seen at 2219 cm^{-1} and C=O stretching of amide group was seen at 1664 cm^{-1}. The PMR spectrum of the compound (**19**) showed singlet at δ 8.26 ($1H_i$), broad singlet at δ 7.70 ($2H_j$), doublet at δ 7.65-7.63 ($1H_b$, J = 7.76), doublet at δ 7.51-7.49 ($1H_c$, J = 7.76), doublet at δ 7.40-7.38 ($1H_g$), doublet at δ 7.36-7.34 ($1H_d$), singlet at δ 7.30 ($1H_a$), multiplet at δ 7.28-7.26 ($1H_f$) and double doublet at δ 6.90-6.87 ($1H_e$, J = 8.7, 2.6 Hz). The aliphatic protons

offered signals at δ 4.18 (s, $2H_h$) and 3.80 (s, $3H_k$). Its ^{13}C-NMR spectrum showed a peak at δ 173.02 due to C=O carbon of the amide. Aromatic carbons appeared at δ 166.35, 161.23, 160.07, 159.99, 158.73, 139.25, 138.03, 128.23, 127.64, 127.25, 126.80, 115.18, 113.27 and 113.02 whereas the aliphatic carbons appeared at δ 85.83, 55.46 and 34.25. Its mass spectrum gave molecular ion peak at 421.12 $(M)^+$.

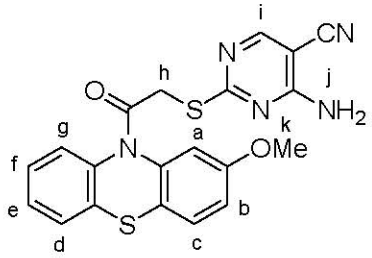

(19)

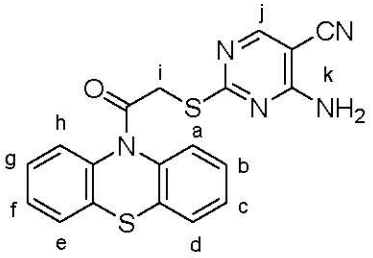

(20)

IR spectrum of compound (**20**) showed N-H stretching vibrations as two strong peaks at 3361 and 3145 cm^{-1}, C≡N stretching of cyano group was seen at 2228 cm^{-1} and C=O stretching of amide group was seen at 1663 cm^{-1}. Its PMR spectrum gave signals at δ 8.21 (s, 1H, Ar-H_j), 7.66-7.64 (d, 2H, J = 7.8 Hz, Ar-$H_{a,d}$), 7.51-7.49 (d, 2H, J = 7.8 Hz, Ar-$H_{h,e}$), 7.48 (bs, 2H, NH_k), 7.40-7.36 (m, 2H, Ar-$H_{b,c}$), 7.31-7.27 (m, 2H, Ar-$H_{g,f}$) and 4.12 (s, 2H, CH_{2i}). Its mass spectrum showed molecular ion peak at 414.4 $(M+Na)^+$.

IR spectrum of compound (**21**) showed N-H stretching vibrations as two strong peaks at 3422 and 3282 cm^{-1}, C=O stretching of ester group and amide group got merged at 1694 cm^{-1}. The PMR spectrum of compound (**21**) showed singlet at δ 8.62 ($1H_i$), singlet at δ 7.93 ($1H_a$), broad singlet at δ 7.80 ($2H_j$), multiplet at δ 7.59-7.55 ($2H_{b,c}$), multiplet at δ 7.51-7.47 ($2H_{g,d}$), multiplet at δ 7.42-7.38 ($1H_f$) and multiplet at δ 7.33-7.29 ($1H_e$). The aliphatic protons showed quartet at δ 4.35-4.29 ($2H_k$), singlet at δ 4.08 ($2H_h$) and triplet at δ 1.38-1.34 ($3H_l$). Its mass spectrum showed molecular ion peak at 506.2 $(M)^+$.

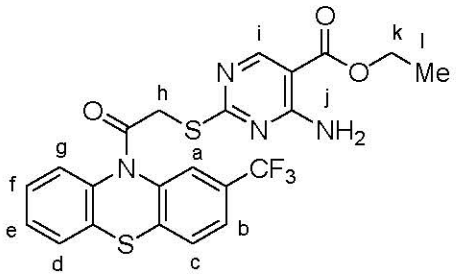

(21)

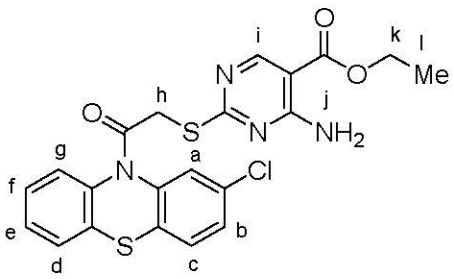

(22)

IR spectrum of compound (**22**) showed N-H stretching vibrations as two strong peaks at 3471 and 3358 cm^{-1}, C=O stretching of ester group and amide group were merged at 1676 cm^{-1}. The PMR spectrum of compound (**22**) offered signals at δ 8.62 (s, 1H, Ar-H_i), 7.79 (bs, 1H, NH_j), 7.67-7.66 (d, 1H, Ar-H_g), 7.57-7.55 (dd, 1H, J = 7.8, 0.8 Hz, Ar-H_b), 7.48-7.46 (dd, 1H, J = 7.8, 1.36 Hz, Ar-H_c), 7.39-7.36 (m, 1H, Ar-H_f), 7.35 (s, 1H, Ar-H_a), 7.30-7.26 (m, 1H, Ar-H_e), 7.24-7.21 (d, 1H, J = 8.4 Hz, Ar-H_d), 5.78 (bs, 1H, NH_j), 4.34-4.29 (q, 2H, CH_{2k}), 4.07 (s, 2H, CH_{2h}) and 1.38 (t, 3H, CH_{3l}). Its ^{13}C-NMR spectrum showed peak at δ 172.97 due to C=O carbon of the amide. Aromatic carbons appeared at δ 166.63, 165.33, 161.15, 158.36, 158.31, 139.22, 137.61, 131.88, 131.56, 131.23, 129.07, 128.10, 127.64, 127.45, 127.24, 127.07 and 100.89 whereas the aliphatic carbon appeared at δ 60.63, 34.04 and 14.04. Its mass spectrum showed molecular ion peak at 494.1 $(M+Na)^+$ and 495.8 $(M+2+Na)^+$.

IR spectrum of compound (**23**) showed N-H stretching vibrations as two strong peaks at 3442 and 3333 cm^{-1}, C=O stretching of ester group and amide group were seen at 1692 cm^{-1}. The PMR spectrum of compound (**23**) showed singlet at δ 8.60 (1H_i), broad singlet at δ 7.77 (1H_j), doublet at δ 7.58-7.56 (1H_g), doublet at δ 7.47-7.45 (1H_b, J = 7.6 Hz), singlet at δ 7.35 (1H_a), multiplet at δ 7.33-7.32 (1H_f), doublet at δ 7.26-7.24 (1H_c, J = 7.6 Hz), multiplet at δ 7.24-7.21 (1H_e), doublet at δ 6.84-6.81 (1H_d) and broad singlet at δ 5.93 (1H_j). The aliphatic protons showed quartet at δ 4.34-4.28 (2H_k), double doublet at δ 4.06 (2H_h), singlet at δ 3.81 (3H_m) and triplet at δ 1.37-1.33 (3H_l). Its ^{13}C-NMR spectrum showed peak at δ 173.97 and 166.87 due to C=O carbon of the ester and amide respectively. Aromatic carbons appeared at δ 166.22, 161.92, 159.30, 159.04, 139.75, 138.49, 128.51, 128.16, 127.18, 127.10, 113.59, 113.07 and 101.34 whereas aliphatic carbon appeared at δ 60.96, 55.73, 35.50 and 14.25. Its mass spectrum showed molecular ion peak at 468.2 (M^+).

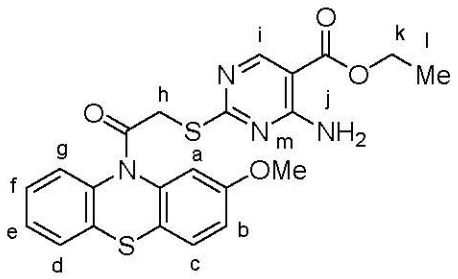

(**23**)

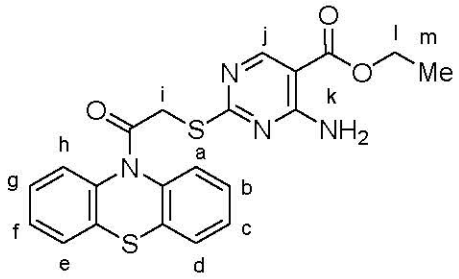

(**24**)

IR spectrum of compound (**24**) showed N-H stretching vibrations as two strong peaks at 3399 and 3278 cm^{-1}, C=O stretching of ester group was seen at 1704 cm^{-1} and

C=O stretching of amide group was seen at 1669 cm^{-1}. Its PMR spectrum yielded signals at δ 8.51 (s, 1H, Ar-H_j), 7.69-7.67 (d, 2H, J = 7.7 Hz, Ar-$H_{a,d}$), 7.55 (bs, 2H, NH_{2k}), 7.53-7.51 (d, 2H, J = 7.7 Hz, Ar-$H_{h,e}$), 7.41-7.37 (m, 2H, Ar-$H_{b,c}$), 7.32-7.28 (m, 2H, Ar-$H_{g,f}$), 4.32-4.28 (q, 2H, CH_{2l}), 4.17 (s, 2H, CH_{2i}) and 1.36-1.32 (t, 3H, CH_{3m}). Its mass spectrum showed molecular ion peak at 438.4 (M^+).

IR spectrum of compound (**25**) showed C=O stretching of amide group at 1680 cm^{-1}. The PMR spectrum of compound (**25**) showed doublet at δ 8.80-8.79 ($2H_{j,l}$, J = 6.1 Hz), singlet at δ 7.93 ($1H_a$), doublet at δ 7.83-7.82 ($2H_{i,k}$, J = 6.1 Hz), doublet at δ 7.65-7.63 ($1H_b$), doublet at δ 7.59-7.57 ($1H_c$), doublet at δ 7.52-7.49 ($2H_{g,d}$), multiplet at δ 7.46-7.41 ($1H_f$) and multiplet at δ 7.37-7.33 (m, $1H_e$). The aliphatic protons showed broad singlet at δ 4.60 ($1H_h$) and 4.25-4.22 ($1H_h$). Its ^{13}C-NMR spectrum showed peak at δ 165.40 due to C=O carbon of the amide. Aromatic carbons appeared at δ 164.92, 164.20, 150.90, 138.09, 137.08, 130.47, 129.84, 129.51, 128.63, 128.35, 128.20, 126.67, 124.92, 124.38, 124.1, 122.21 and 120.0 whereas the aliphatic carbon appeared at δ 36.96. Its mass spectrum exhibited molecular ion peak at 486.6 $(M)^+$.

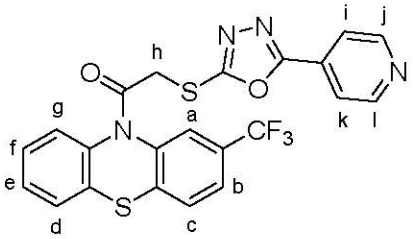

(**25**)

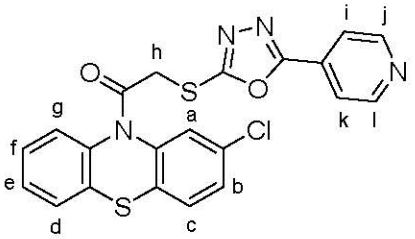

(**26**)

IR spectrum of compound (**26**) showed C=O stretching of amide group at 1679 cm^{-1}. Its PMR spectrum offered signals at δ 8.80-8.78 (d, 2H, J = 6.1 Hz, Ar-$H_{j,l}$), 7.83-7.82 (d, 2H, J = 6.1 Hz, Ar-$H_{i,k}$), 7.67 (s, 1H, Ar-H_a), 7.62-7.60 (d, 1H, Ar-H_b), 7.50-7.48 (d, 1H, Ar-H_c), 7.42-7.40 (m, 1H, Ar-H_f), 7.39-7.37 (d, 1H, Ar-H_g), 7.33-7.29 (m, 1H, Ar-H_e), 7.27-7.24 (m, 1H, Ar-H_d) for aromatic protons. The aliphatic protons showed broad singlet at δ 4.53 ($1H_h$) and 4.30 ($1H_h$). Its mass spectrum showed molecular ion peak at 452.2 $(M)^+$ and 454.2 $(M+2)^+$.

IR spectrum of compound (**27**) showed C=O stretching of amide group at 1671 cm^{-1}. The PMR spectrum of compound (**27**) showed doublet at δ 8.80-8.78 ($2H_{j,l}$, J = 6.0 Hz), doublet at δ 7.83-7.82 ($2H_{i,k}$, J = 6.0 Hz), doublet at δ 7.62-7.60 ($1H_b$, J = 7.8 Hz), doublet at δ 7.48-7.46 ($1H_c$, J = 7.8 Hz), multiplet at δ 7.38-7.34 ($2H_{f,a}$), multiplet at δ 7.29-7.27 ($1H_e$), doublet at δ 7.25-7.23 ($1H_g$), doublet at δ 6.86-6.84 ($1H_d$), broad

singlet at δ 4.45 ($2H_h$) and a singlet at δ 3.83 ($3H_m$). Its mass spectrum yielded molecular ion peak at 448.6 (M^+).

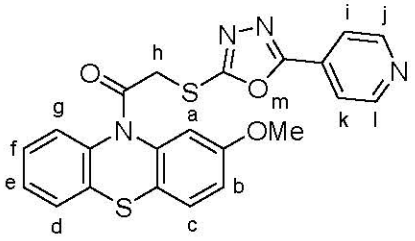

(27)

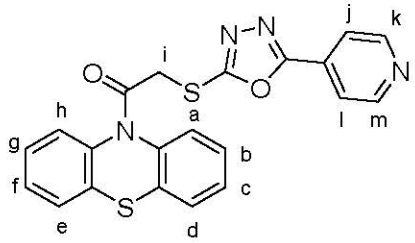

(28)

In IR spectrum of compound (**28**) C=O stretching of the amide group was seen at 1667 cm^{-1}. The PMR spectrum of compound (**28**) showed signals at δ 8.79-8.77 (d, 2H, J = 6.0 Hz, Ar-$H_{k,m}$), 7.82-7.81 (d, 2H, J = 6.0 Hz, Ar-$H_{j,l}$), 7.63-7.61 (d, 2H, Ar-$H_{a,d}$), 7.49-7.47 (d, 2H, Ar-$H_{h,e}$), 7.39-7.35 (m, 2H, Ar-$H_{b,c}$), 7.30-7.26 (m, 2H, Ar-$H_{g,f}$), and 4.44 (bs, 2H, CH_{2i}). Its mass spectrum offered molecular ion peak at 418.6 (M^+).

IR spectrum of compound (**29**) showed N-H stretching vibrations as two strong peaks at 3321 and 3111 cm^{-1} and C=O stretching of amide group was seen at 1670 cm^{-1}. The PMR spectrum of compound (**29**) showed doublet at δ 8.70-8.68 ($2H_{j,l}$, J = 5.6 Hz), doublet at δ 8.03-8.01 ($2H_{i,k}$, J = 5.6 Hz), singlet at δ 8.01 ($1H_a$), doublet at δ 7.82-7.80 ($1H_g$), doublet at δ 7.75-7.73 ($1H_b$, J = 8.3 Hz), doublet at δ 7.62-7.60 ($1H_c$, J = 8.3 Hz), doublet at δ 7.58-7.56 ($1H_d$), multiplet at δ 7.47-7.44 ($1H_f$) and multiplet at δ 7.39-7.35 ($1H_e$). The aliphatic protons gave a singlet at δ 6.22 ($2H_h$). Broad singlets were observed at δ 4.54 (bs, $1H_m$) and 4.28 (bs, $1H_m$) due to the protons of amine. Its mass spectrum showed molecular ion peak at 500.89 (M^+).

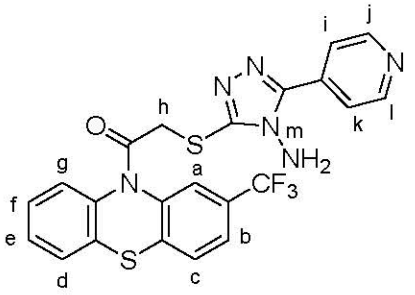

(29)

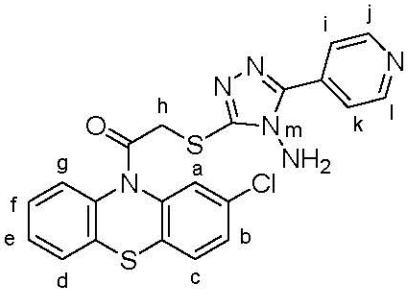

(30)

IR spectrum of compound (**30**) showed N-H stretching vibrations as two strong peaks at 3320 and 3106 cm^{-1} and C=O stretching of amide group was seen at 1666 cm^{-1}. Its PMR spectrum offered signals at δ 8.69-8.68 (d, 2H, J = 4.8 Hz, Ar-$H_{j,l}$), 8.07-

8.06 (d, 2H, J = 4.8, Ar-$H_{i,k}$), 7.71 (s, 1H, Ar-H_a), 7.71-7.69 (d, 1H, Ar-H_b), 7.52-7.50 (d, 1H, Ar-H_c), 7.47-7.45 (d, 1H, Ar-H_g), 7.42-7.38 (m, 1H, Ar-H_f), 7.34-7.32 (m, 1H, Ar-H_e), 7.30-7.28 (d, 1H, Ar-H_d), 6.12 (s, $2H_h$), 4.45 (bs, $1H_m$) and 4.24 (bs, $1H_m$). Its mass spectrum showed molecular ion peak at 465.9 $(M)^+$ and 467.6 $(M+2)^+$.

IR spectrum of compound (**31**) showed N-H stretching vibrations as two strong peaks at 3318 and 3207 cm^{-1} and C=O stretching of amide group was seen at 1654 cm^{-1}. Compound (**31**) showed doublet at δ 8.70-8.68 ($2H_{j,l}$, J = 6.1 Hz), doublet at δ 8.03-8.01 ($2H_{i,k}$, J = 6.1 Hz), doublet at δ 7.68-7.65 ($1H_g$), doublet at δ 7.52-7.50 ($1H_d$), multiplet at 7.42-7.36 ($3H_{b,a,f}$), multiplet at δ 7.31-7.30 (m, $1H_e$), doublet at δ 6.93-6.90 ($1H_c$), singlet at δ 6.22 ($2H_h$), broad singlet 4.40 ($2H_m$) and singlet at δ 3.81 ($3H_n$) in its PMR spectrum. Its mass spectrum offered molecular ion peak at 462.1 (M^+).

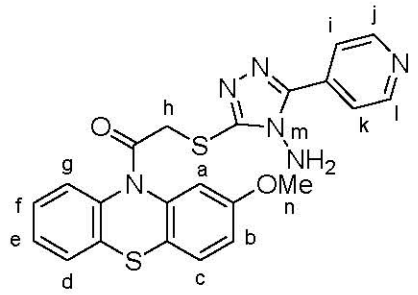

(**31**)

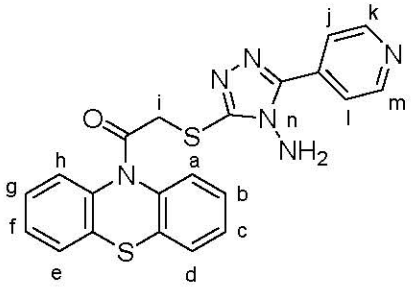

(**32**)

Compound (**32**) showed N-H stretching vibrations as two strong peaks at 3308 and 3202 cm^{-1} and C=O stretching of amide group at 1652 cm^{-1} in its IR spectrum. Its PMR spectrum exhibited signals at δ 8.69-8.68 (d, 2H, J = 6.1 Hz, Ar-$H_{k,m}$), 8.03-8.02 (d, 2H, J = 6.1 Hz, Ar-$H_{j,l}$), 7.73-7.71 (d, 2H, Ar-$H_{a,d}$), 7.54-7.52 (d, 2H, Ar-$H_{h,e}$), 7.42-7.38 (m, 2H, Ar-$H_{b,c}$), 7.33-7.29 (m, 2H, Ar-$H_{g,f}$), 6.20 (s, 2H, CH_{2i}) and 4.37 (bs, 2H, NH_{2n}). Molecular ion peak was obtained at 432.8 (M^+) in its mass spectrum.

4.4.3.4 Synthesis of 10-(3-chloropropyl)-10*H*-phenothiazine derivatives (34-37)

2-Substituted phenothiazines (**7-10**) were reacted with 1-bromo-3-chloropropane (**33**) in the presence of NaH to obtain 10-(3-chloropropyl)-10*H*-phenothiazine derivatives (**34-37**). Compound (**34**) showed molecular ion peak at 342.9 $(M+1)^+$ in its mass spectrum. In mass spectrum compound (**35**) showed molecular ion peak at 301 $(M+1)^+$ and 303 $(M+3)^+$. Compound (**36** and **37**) showed molecular ion peaks at 305.1 $(M+1)^+$ and 275.2 $(M+1)^+$ respectively in their mass spectra.

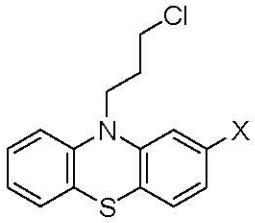

(**34**) X = CF_3; (**35**) X = Cl
(**36**) X = OMe; (**37**) X = H

4.4.3.5 Synthesis of 5-substituted 2-(3-(2-substituted-10*H*-phenothiazin-10-yl)-propylthio)-4-aminopyrimidine derivatives (38-45)

IR spectrum of compound (**38**) showed N-H stretching vibrations as two strong peaks at 3475 and 3306 cm^{-1} and C≡N stretching of cyano group was seen at 2220 cm^{-1}. It offered signals at δ 8.23 (s, 1H, Ar-H_k), 7.72 (bs, 2H, NH_{2l}), 7.31-7.29 (d, 1H, Ar-H_b), 7.21-7.19 (m, 2H, Ar-$H_{f,e}$), 7.16-7.13 (m, 2H, Ar-$H_{c,a}$), 7.06-7.04 (d, 1H, J = 7.92, Ar-H_g), 7.00-6.98 (m, 1H, Ar-H_d), 4.09-4.05 (t, 2H, CH_{2h}), 3.18-3.14 (t, 2H, CH_{2j}) and 2.14-2.10 (m, 2H, CH_{2i}) in its PMR spectrum. Its mass spectrum showed molecular ion peak at 459.3 (M^+).

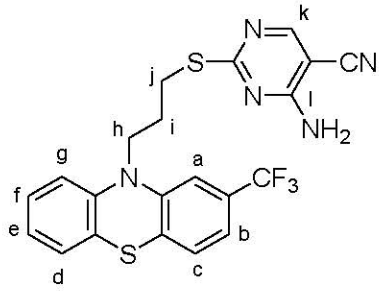

(**38**)

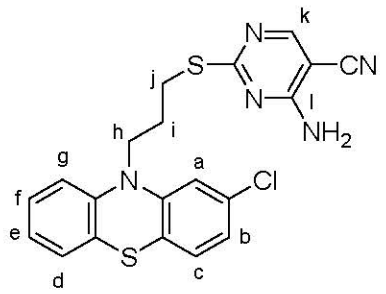

(**39**)

IR spectrum of compound (**39**) showed N-H stretching vibrations as two strong peaks at 3444 and 3343 cm^{-1} and the C≡N stretching of cyano group was seen at 2218 cm^{-1}. In the PMR spectrum of the compound (**39**), protons appeared as singlet at δ 8.23 ($1H_k$), broad singlet at δ 7.70 ($2H_l$), multiplet at δ 7.18-7.16 ($1H_f$), doublet at δ 7.13-7.11 ($1H_g$), doublet at δ 7.09-7.07 ($1H_b$, J = 8.1 Hz), doublet at δ 7.02-7.00 ($1H_d$), singlet at δ 6.97 ($1H_a$), multiplet at δ 6.97-6.95 ($1H_e$) and doublet at δ 6.94-6.91 ($1H_c$, J = 8.1 Hz). Peaks were observed at δ 4.02-3.98 (t, 2H, CH_{2h}), 3.16-3.13 (t, 2H, CH_{2j}) and 2.14-2.11 (m, 2H, CH_{2i}) for aliphatic protons. Its mass spectrum showed molecular ion peak at 446.5 ($M+Na^+$) and 448.5 $(M+2+Na)^+$.

IR spectrum of compound (**40**) showed N-H stretching vibrations as two strong peaks at 3414 and 3340 cm^{-1} and C≡N stretching of cyano group at 2217 cm^{-1}. PMR spectrum of compound (**40**) gave peaks at δ 8.12 (s, 1H, Ar-H_k), 7.09-7.04 (m, 2H, Ar-$H_{f,e}$), 6.98-6.96 (d, 1H, J = 8.0 Hz, Ar-H_b), 6.87-6.82 (m, 1H, Ar-H_g), 6.81-6.79 (d, 1H, J = 8.0 Hz, Ar-H_c), 6.44-6.41 (d, 1H, Ar-H_d), 6.41 (s, 1H, Ar-H_a), 5.44 (bs, 2H, NH_{2l}), 3.92-3.89 (t, 2H, CH_{2h}), 3.70 (s, 3H, CH_{3m}), 3.12-3.09 (t, 2H, CH_{2j}) and 2.17-2.12 (m, 2H, CH_{2i}). In its ^{13}C-NMR spectrum, aromatic carbons appeared at δ 174.06, 161.30, 159.49, 159.22, 145.84, 144.24, 127.05, 126.79, 126.70, 124.76, 122.07, 115.33, 115.16, 114.94, 106.64 and 102.86 whereas the aliphatic carbons appeared at δ 85.41, 54.91, 45.12, 27.29 and 25.91. Its mass spectrum offered molecular ion peak at 420.7 (M^+).

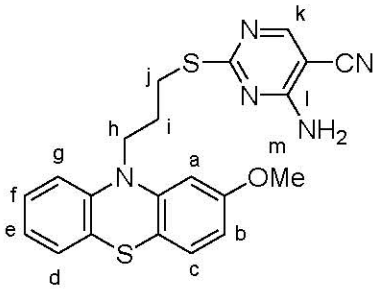

(**40**)

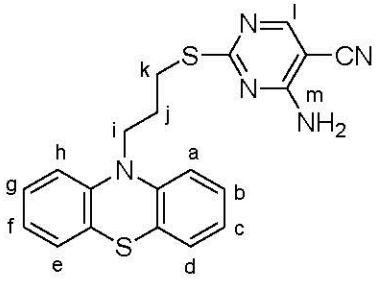

(**41**)

IR spectrum of compound (**41**) showed N-H stretching vibrations as two strong peaks at 3353 and 3160 cm^{-1} and C≡N stretching of cyano group at 2224 cm^{-1}. Its PMR spectrum offered signals at δ 8.19 (s, 1H, Ar-H_l), 7.18-7.13 (m, 4H, Ar-H_{a-d}), 6.96-6.92 (m, 2H, Ar-$H_{g,f}$), 6.90-6.88 (d, 2H, Ar-$H_{h,e}$), 5.33 (bs, 2H, NH_{2m}), 4.05-4.02 (t, 2H, CH_{2i}), 3.22-3.18 (t, 2H, CH_{2k}) and 2.25-2.18 (m, 2H, CH_{2j}). In its ^{13}C-NMR spectrum, aromatic carbons appeared at δ 175.88, 161.46, 159.49, 145.28, 127.64, 127.33, 125.61, 122.69, 115.70 and 115.06 whereas the aliphatic carbon appeared at δ 86.13, 45.63, 28.42 and 26.56. Its mass spectrum showed molecular ion peak at 391.5 $(M)^+$.

Compound (**42**) showed N-H stretching vibrations as two strong peaks at 3422 and 3282 cm^{-1} and C=O stretching of ester group at 1697 cm^{-1} in its IR spectrum. The PMR spectrum of compound (**42**) yielded a singlet at δ 8.60 ($1H_k$), broad singlet at δ 7.76 ($1H_l$), doublet at δ 7.23-7.21 ($1H_b$, J = 8.0 Hz), multiplet at δ 7.17-7.13 ($3H_{f,g,d}$), singlet at δ 7.04 ($1H_a$), multiplet at δ 6.98-6.94 ($1H_e$) and a doublet at δ 6.92-6.90 ($1H_c$, J = 8.0 Hz). A broad singlet was observed at δ 5.40 ($1H_l$) for protons of the amine. The aliphatic protons showed a quartet at δ 4.36-4.30 ($2H_m$), triplet at δ 4.06-4.03 ($2H_h$),

triplet at δ 3.23-3.20 ($2H_j$), multiplet at δ 2.27-2.20 (m, $2H_i$) and a triplet at δ 1.39-1.36 (t, $3H_n$). Molecular ion peak was obtained at 506.68 (M^+) in its mass spectrum.

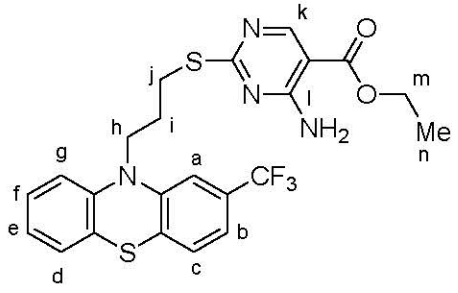

(**42**)

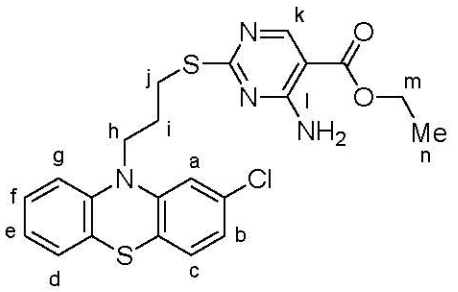

(**43**)

IR spectrum of compound (**43**) showed N-H stretching vibrations as two strong peaks at 3412 and 3268 cm^{-1} and a C=O stretching of ester group was seen at 1695 cm^{-1}. The PMR spectrum of compound (**43**) exhibited signals at δ 8.40 (s, 1H, Ar-H_k), 7.54 (bs, 1H, NH_l), 6.96-6.91 (m, 2H, Ar-$H_{b,a}$), 6.83-6.81 (d, 1H, Ar-H_c), 6.74-6.70 (m, 1H, Ar-H_f), 6.68-6.63 (m, 3H, Ar-$H_{e,g,d}$), 5.25 (bs, 1H, NH_l), 4.14-4.09 (q, 2H, CH_{2m}), 3.79-3.75 (t, 2H, CH_{2h}), 3.00-2.95 (t, 2H, CH_{2j}), 2.05-1.98 (m, 2H, CH_{2i}) and 1.18-1.14 (t, 3H, CH_{3n}). Its mass spectrum showed molecular ion peaks at 472.5 $(M)^+$ and 474.5 $(M+2)^+$.

IR spectrum of compound (**44**) showed N-H stretching vibrations as two strong peaks at 3410 and 3268 cm^{-1} and C=O stretching of ester group at 1691 cm^{-1}. The PMR spectrum of compound (**44**) showed signals at δ 8.61 (s, 1H, Ar-H_k), 7.74 (bs, 1H, NH_l), 7.15-7.11 (m, 2H, Ar-$H_{f,g}$), 7.04-7.02 (d, 1H, J = 8.1 Hz, Ar-H_b), 6.92-6.90 (m, 1H, Ar-H_e), 6.89-6.87 (d, 1H, J = 8.1 Hz, Ar-H_c), 6.49 (s, 1H, Ar-H_a), 6.49-6.47 (d, 1H, Ar-H_d), 5.45 (bs, 1H, NH_l), 4.35-4.30 (q, 2H, CH_{2n}), 4.00-3.96 (t, 2H, CH_{2h}), 3.76 (s, 3H, CH_{3m}), 3.21-3.17 (t, 2H, CH_{2j}), 2.28-2.22 (m, 2H, CH_{2i}) and 1.38-1.35 (t, 3H, CH_{3o}). Its ^{13}C-NMR spectrum exhibited peak at δ 175.34 due to C=O carbon of ester. Aromatic carbons appeared at δ 166.35, 161.80, 159.72, 158.97, 146.55, 144.97, 127.69, 127.46, 127.15, 125.70, 122.56, 116.20, 115.57, 106.77, 103.49 and 101.15 whereas the aliphatic carbon appeared at δ 60.95, 55.50, 46.02, 28.25, 26.75 and 14.29. Its mass spectrum yielded molecular ion peak at 468.5 $(M)^+$.

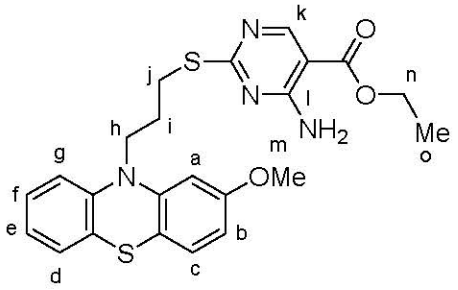

(44)

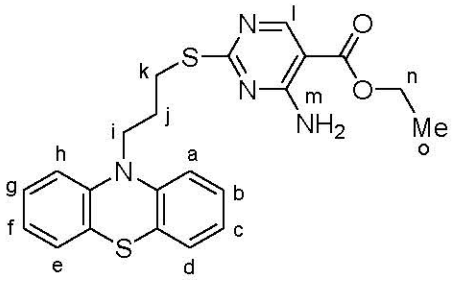

(45)

IR spectrum of compound (**45**) showed N-H stretching vibrations as two strong peaks at 3416 and 3270 cm^{-1} and C=O stretching of ester group at 1698 cm^{-1}. The PMR spectrum of compound (**45**) yielded signals at δ 8.60 (s, 1H, Ar-H_l), 7.72 (bs, 1H, NH_m), 7.16-7.12 (m, 4H, Ar-$H_{a,b,c,d}$), 6.93-6.88 (m, 4H, Ar-$H_{h,g,f,e}$), 5.36 (bs, 1H, NH_m), 4.35-4.29 (q, 2H, CH_{2n}), 4.04-4.00 (t, 2H, CH_{2i}), 3.22-3.19 (t, 2H, CH_{2k}), 2.26-2.20 (m, 2H, CH_{2j}) and 1.38-1.35 (t, 3H, CH_{3o}). Its mass spectrum showed molecular ion peak at 438.7 (M^+).

4.5 Pharmacological evaluation/screening of the synthesized compounds as peripherally acting CB1 receptor antagonists for the treatment of obesity

4.5.1 *In vitro* permeability assay of the test compounds

As discussed above, the brain permeation of the available CB1 receptor antagonists limits their therapeutic usage. Therefore, a successful CB1 receptor antagonist to be used as anti-obesity agent must be devoid of BBB permeability. Compounds which showed predicted activity of $pK_i \geq 7.5$ were selected for evaluation for BBB penetration study. In this study, the ability of the test compounds to cross the BBB was determined by the *in vitro* model PAMPA-BBB assay. This simple and rapid model has the advantage to predict passive BBB permeation with high accuracy.[272,273] The *in vitro* permeability (P_e) of the test compounds through the lipid extract of porcine brain was determined in PBS/ethanol (70:30). For validation of the assay, reported permeability values of nine quality standards[272] were compared with their experimental permeability values (see supplementary information, Table S2) which gave a linear relationship, P_e(exp.)= 1.171P_e(bibl.) + 1.489 (R^2 = 0.983). From this equation and considering the limit established by Di. et al[272], the range of permeability (P_e) (see supplementary information, Table S3) was determined. All the test compounds showed

permeability (P_e) values less than 3.8×10^{-6} cm s^{-1}, suggesting[306] that they would not cross the BBB by passive diffusion (Table 4.5.1).

Table 4.5.1 Permeability (P_e) results from the PAMPA-BBB assay with their predicted penetration in CNS. (Data expressed as mean±SEM of three independent experiments. 'CNS'- indicates low passive CNS permeation)

Compound	P_e (10^{-6} cm s^{-1})	Prediction
1	2.78±0.14	CNS-
18	2.28±0.11	CNS-
19	3.08±0.16	CNS-
21	2.72±0.19	CNS-
22	3.66±0.67	CNS-
23	2.80±0.58	CNS-
28	3.22±0.63	CNS-
29	1.05±0.22	CNS-
30	2.09±0.82	CNS-
38	2.60±0.18	CNS-
39	3.47±0.66	CNS-
40	3.58±0.73	CNS-
42	2.84±0.28	CNS-
43	3.28±0.38	CNS-

4.5.2 Acute hypophagic effect of the test compounds

As a preliminary screening, the synthesized compounds were evaluated for acute hypophagia in rats and the results are summarized in Fig. 4.5.1. Twenty four hr food deprived Wistar rats were given weighed amounts of food pellets after administration of the test compounds. Control was considered as 100 %. Out of the 14 compounds, three compounds (**28**, **29** and **38**) were not found effective to decrease the food intake (80-99 %) and seven test compounds (**1, 18, 22, 39**, **40**, **42** and **43**) were found weakly acting (62-74 %) food inhibitors after 2 hr of treatment, showing non-significant effects. However, four compounds (**19**, **21**, **23** and **30**) showed significant hypophagic activity (19-43 %) compared to the control animals ($p < 0.01$).

In another set of experiments, the selected test compounds (**19**, **21**, **23** and **30**) were further evaluated in presence of WIN-55212-2, a potent cannabinoid receptor agonist to assess their *in vivo* CB1 receptor antagonistic activity. Control group was considered as 100 %, and 54 % increase in the food intake was observed when the animals were treated with WIN-55212-2. Ability of the test compounds to attenuate the WIN-55212-2 mediated hyperphagic response indicated their CB1 receptor antagonistic

potential. WIN-55212-2 significantly (54 %) increased the amount of food intake in fasted animals as compared to the control group ($p < 0.05$). However, the effect of WIN-55212-2 was significantly attenuated by the test compounds (**19**, **21**, **23** and **30**) ($p < 0.001$). These compounds (**19**, **21**, **23** and **30**) showed significant decrease (36 %, 36 %, 26 % and 28 %) respectively in food intake as compared to the control. The results suggested CB1 receptor antagonistic potential of the test compounds (**19**, **21**, **23** and **30**).

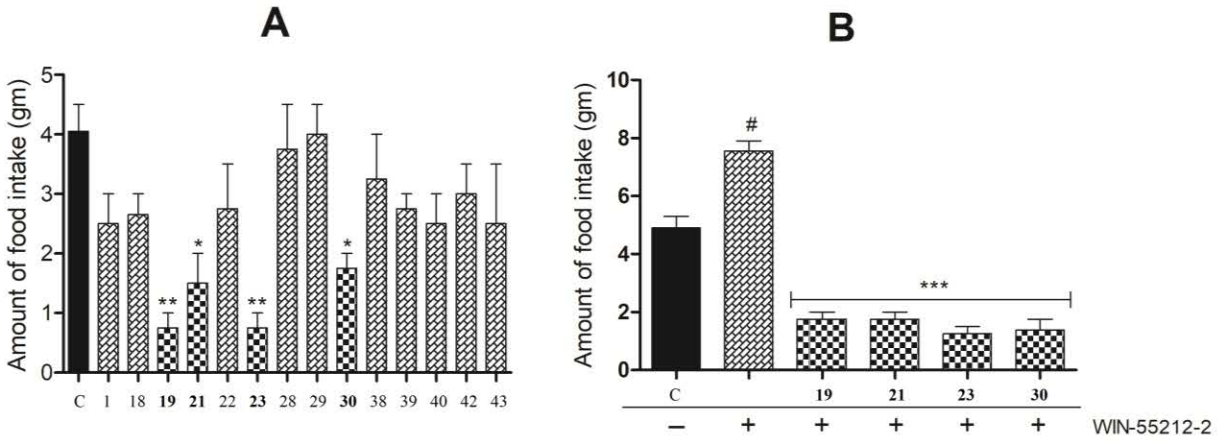

Fig. 4.5.1 Hypophagic response of the test compounds alone (A) and in presence of WIN-55212-2 (B). Data expressed as mean ± SEM (n=6). ** $p < 0.01$, * $p < 0.05$ *vs.* vehicle-treated control group (A). $^{\#}p < 0.01$ *vs.* vehicle-treated control group. ***$p < 0.001$ *vs.* WIN-55212-2-treated group (B).

4.6 Molecular modeling and SAR of the synthesized compounds

4.6.1 Pharmacophore mapping

Modeling studies were performed to evaluate the fitting of the synthesized compounds into the previously developed pharmacophore model (AHRR.6). The highest fitness score was observed (1.77) for compound (**22**) in pharmacophore mapping. Compound (**22**) occupied all four pharmacophoric features as shown in Fig. 4.6.1a in which two aromatic rings of the phenothiazine ring occupied two aromatic ring features, Cl group at 2nd position of phenothiazine ring occupied one hydrophobic feature and oxygen of ester group acts as the hydrogen bond acceptor feature. The most active compounds (**19**, **21**, **23** and **30**) showed good fitness scores (1.63, 1.53, 1.60 and 1.46 respectively) and all the structures fitted well into all the four pharmacophoric features which could be the reason for their good biological activity. The lowest fitness

score of 0.95 was shown by compound (**32**) as it did not contain a hydrophobic feature at 2nd position of phenothiazine ring when mapped in the pharmacophore model. Absence of the hydrophobic feature, flipped the molecule in such a way that one aromatic feature was occupied by phenyl ring of the phenothiazine scaffold and another by the triazole ring. Hydrogen bond acceptor feature was oriented near the nitrogen of the pyridine ring as shown in Fig. 4.6.1b. So, the orientation of compound (**32**) got poor fitness score in pharmacophore mapping. It was clear from this study that it is necessary to match all the pharmacophoric features for good biological activity.

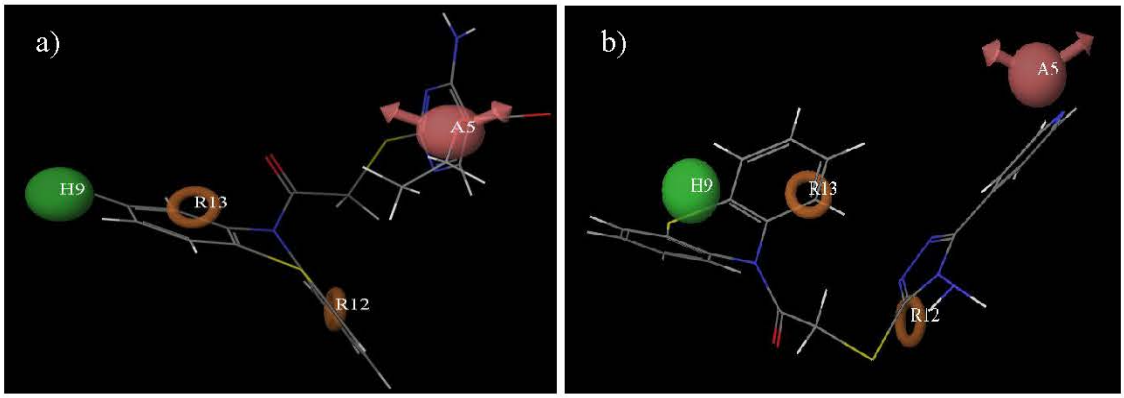

Fig. 4.6.1 Pharmacophore mapping of a) the highest fitness score compound (**22**) and b) the lowest fitness score compound (**32**).

4.6.2 Docking studies

In docking studies, it was observed that formation of a hydrogen bond with Lys192 residue was a characteristic feature for the CB1 receptor antagonistic activity. The virtual screening hit V11 (**1**) molecule having a G-score of -10.58 was observed to have binding in the active site of CB1 receptor forming hydrogen bond with Lys192 residue. Compounds (**21** and **23**) showed G-scores of -10.37 and -10.33 respectively, formed two hydrogen bonds, one between the nitrogen of pyrimidine ring with Lys192 residue and another between the hydrogen of amine attached to pyrimidine ring with Ser265 residue, which could be responsible for their good biological activity. The orientation of compound (**21**) in the active site of CB1 receptor is shown in Fig. 4.6.2a. Similarly, compounds (**19** and **30**) also showed good G-scores (-10.04 and -9.80 respectively) and were well oriented in the active site of CB1 receptor which supported their good biological activity. The lowest G-score (-8.70) was observed for compound (**43**). Although it formed one hydrogen bond with Lys192 residue as shown in Fig. 4.6.2b but still showed comparatively lower G-score as compared to other compounds.

This might be due to the introduction of 3 carbon chain spacer which increased the distance between phenothiazine ring (containing 2 aromatic rings and 1 hydrophobic features) and the substituted pyrimidine ring (containing one hydrogen bond acceptor feature).

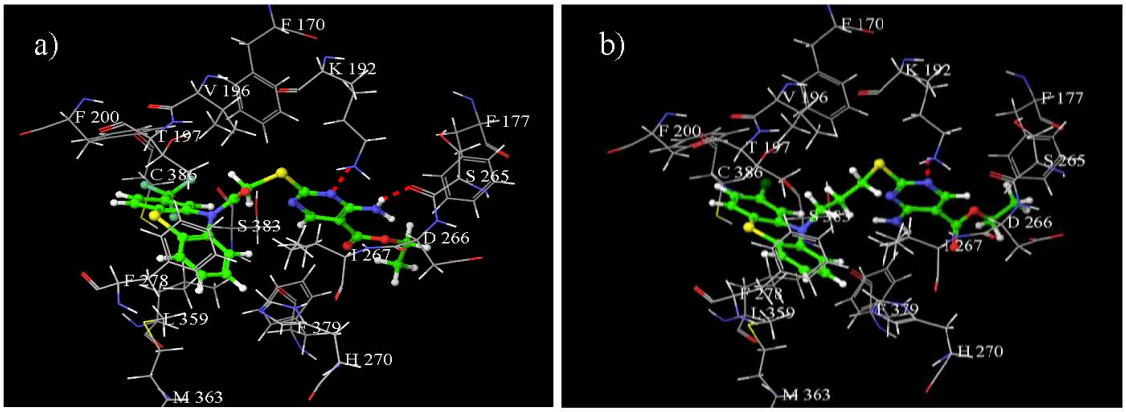

Fig. 4.6.2 Orientation of a) active compound (**21**), and b) less active compound (**43**).

4.6.3 Structure Activity Relationship (SAR)

Different phenothiazine derivatives were synthesized so that a structure activity relationship could be developed. In the hypophagic study, the food intake by the control group was considered as 100 %. The food intake got decreased (62 %) when treated with compound (**1**), the virtual screening hit V11 molecule acting as an antagonist. Replacement of trifluoromethyl group of compound (**1**) with methoxy group yielded compound (**19**) which caused significant decrease in the food intake (19 %). Replacement of 4-amino-2-mercaptopyrimidine-5-carbonitrile group of compound (**1**) by 4-aminopyrimidine-5-carboxylate resulted in compound (**21**) having decreased activity (food intake 37 %). Further, the trifluoromethyl group of compound (**21**) when replaced by methoxy group in compound (**23**) caused decreased food intake (19 %). The trifluoromethyl and 4-amino-2-mercaptopyrimidine-5-carbonitrile groups of compound (**1**) when replaced by chloro and 4-amino-5-(4-pyridyl)-4*H*-1,2,4-triazole groups resulted in compound (**30**) having lower activity (decreasing the food intake to 43 %). Whereas replacement of chloro group of **30** by trifluoromethyl group in compound (**29**) did not show any effect on food intake. Similarly, presence of hydrogen and 4-(1,3,4-oxadiazol-2-yl)pyridine group in compound (**28**) also showed no effect on food intake. Removal of amide linkage of compound (**1**) by three carbon chain resulted in compound (**38**) having no effect on food intake. In another experiment carried out

with WIN-55212-2, compound (**19**, **21**, **23** and **30**) showed significant decrease in food intake (36 %, 36 %, 26 % and 28 % respectively) which indicated their potential antagonistic property.

In nutshell, the SAR revealed that hydrophobic substituents such as trifluoromethyl, chloro and methoxy at 2nd position of phenothiazine ring were beneficial for the activity specially the methoxy group in compounds (**19** and **23**). Whereas, absence of hydrophobic feature at the 2nd position of phenothiazine ring resulted in poor activity as observed in compound (**28**) underlining the importance of a hydrophobic feature at this position. Amide linkage was observed to be favourable for the activity. Replacement of the amide linkage by a 3-spacer carbon chain in compounds (**38**, **39**, **40**, **42** and **43**) were found comparatively less active than the compounds (**19**, **21**, **23** and **30**) having an amide linkage. Different polar groups such as 4-amino-2-mercaptopyrimidine-5-carbonitrile in compound (**19**), 4-aminopyrimidine-5-carboxylate in compounds (**21** and **23**) and 4-amino-5-(4-pyridyl)-4*H*-1,2,4-triazole group in compound (**30**) were found useful to increase the PSA of the compounds and acted as hydrogen bond acceptor features which formed hydrogen bond with Lys192 residue and were found favourable for CB1R antagonistic activity.